



Skolkovo Institute of Science and Technology

REVEALING ELECTROCHEMICAL DEGRADATION PATHWAYS IN COMPLEX
LEAD HALIDES AND DESIGN OF STABLE PEROVSKITE SOLAR CELLS

Doctoral Thesis

by

OLGA R. YAMILOVA

DOCTORAL PROGRAM IN MATERIALS SCIENCE AND ENGINEERING

Supervisor
Professor Keith J. Stevenson

Moscow - 2023

© Olga R. Yamilova 2023

I hereby declare that the work presented in this thesis was carried out by myself at Skolkovo Institute of Science and Technology, Moscow, except where due acknowledgement is made, and has not been submitted for any other degree.

Candidate (Olga R. Yamilova)

Supervisor (Prof. Keith J. Stevenson)

Abstract

Recently lead halide perovskite solar cells demonstrated impressive power conversion efficiencies going beyond 25%. However, poor operational stability of these devices hampers their practical application. Among other factors, an active layer of the operating solar cells must sustain the electric field induced by the built-in and light-induced potentials. Unfortunately, electrochemical stability of complex lead halides remains poorly elucidated.

This Thesis is dedicated to the investigation of the field-induced degradation pathways of complex organo-inorganic lead halides with a perovskite structure and solar cells based on these materials. On the first stage, a model perovskite material methylammonium lead iodide was investigated to understand the general degradation pathway in the bulk material. On the second stage, a set of perovskite materials was compared and the influence of chemical composition on electrochemical stability was defined. On the last stage, application of an external bias to the complete solar cells allowed better clarity of the factors influencing the stability of the operating device.

It was revealed that the biasing leads to the classical reduction-oxidation process where the organic component of the perovskite material undergoes reduction with the following material destruction observed by PL mapping and AFM and thus becoming responsible for the irreversibility of the process. It was also demonstrated that replacement of a highly volatile methylammonium cation in the perovskite structure with a less volatile formamidinium cation or inorganic Cs^+ and Rb^+ improves the stability of the material significantly. A general pathway for electrochemical degradation of solar

cells was proposed, where small biasing voltage/duration leads to the electrochemical doping and efficiency increasing due to the charge-carriers accumulation, further biasing induces interlayer ion migration. And if an aggressive factor like oxygen or water is present in the adjacent charge-transport layer, it initiates a redox process in the perovskite layer. Thus, it was proved that the nature of the adjacent-to-the-perovskite-layer material in the solar cell structure is the most important for the device stability since some materials appear to be chemically aggressive to the perovskite components while the others play the role of protection and encapsulation layers. The choosing of the metal for the top electrode is also appeared significant since the majority of the metals are highly reactive towards iodide anions present in the perovskite structure.

Thus, this work has paved the way towards a direct design of photoactive and charge transport materials for electrochemically stable perovskite solar cells.

Publications

Articles in peer-reviewed journals:

1. Elnaggar, M.; Boldyreva, A. G.; Elshobaki, M.; Tsarev, S. A.; Fedotov, Yu. S.; Yamilova, O. R.; Bredikhin, S. I.; Stevenson, K. J.; Aldoshin, S. M.; Troshin, P. A., Decoupling contributions of charge-transport interlayers to light-induced degradation of p-i-n perovskite solar cells. *RRL Solar* **2020**, *4* (9), 2000191. DOI: 10.1002/solr.202000191
2. Tepliakova, M. M.; Mikheeva, A. N.; Frolova, L. A.; Boldyreva, A. G.; Elakshar, A.; Novikov, A. V.; Tsarev, S. A.; Ustinova, M. I.; Yamilova, O. R.; Nasibulin, A. G.; Aldoshin, S. M.; Stevenson, K. J.; Troshin, P. A., Incorporation of vanadium (V) oxide in hybrid hole transport layer enables long-term operational stability of perovskite solar cells. *J. Phys. Chem. Lett.* **2020**, *11* (14) 5563-5568. DOI: 10.1021/acs.jpcclett.0c01600
3. Yamilova, O. R.; Danilov, A. V.; Mangrulkar, M.; Fedotov, Yu. S.; Luchkin, S. Yu.; Babenko, S. D.; Bredikhin, S. I.; Aldoshin, S. M.; Stevenson, K. J.; Troshin, P. A., Reduction of methylammonium cations as a major electrochemical degradation pathway in MAPbI₃ perovskite solar cells. *J. Phys. Chem. Lett.* **2020**, *11* (1), 221-228. DOI: 10.1021/acs.jpcclett.9b03161

Submitted manuscripts:

Yamilova, O. R.; Fedotov, Yu. S.; Bredikhin, S. I.; Stevenson, K. J., How the Nature and Processing of Hole-Transport Material Can Affect the Field-Induced Degradation of p-i-n Perovskite Solar Cells, *Solar Energy Materials and Solar Cells* 2022, submitted.

Conferences:

1. Yamilova, O. R.; Fedotov, Yu. S.; Danilov, A. V.; Bredikhin, S. I.; Frolova, L. A.; Aldoshin, S. M.; Stevenson, K. J.; Troshin, P. A., Influence of charge transport layers on the electrochemical stability of perovskite solar cells, The International On-Line Conference Stab-Pero 2020, 2-3 June **2020** (e-Poster)
2. Yamilova, O. R.; Fedotov, Yu. S.; Danilov, A. V.; Bredikhin, S. I.; Frolova, L. A.; Stevenson, K. J.; Troshin, P. A., Impact of charge transport interlayers on the electrochemical stability of perovskite solar cells, The International Conference on Advanced Electromaterials (ICAE) 2019, Jeju, Korea, 5-8 November **2019** (poster presentation) - Best Poster Prize
3. Yamilova, O. R.; Fedotov, Yu. S.; Danilov, A. V.; Bredikhin, S. I.; Frolova, L. A.; Stevenson, K. J.; Troshin, P. A., Influence of hole transport materials on the electrochemical stability of perovskite solar cells, The International school on Hybrid, Organic and Perovskite Photovoltaics (HOPE-PV) 2019, Moscow, Russia, 21-23 October **2019** (oral talk) - Best Oral Presentation Prize
4. Yamilova, O. R.; Fedotov, Yu. S.; Danilov, A. V.; Bredikhin, S. I.; Frolova, L. A.; Stevenson, K. J.; Troshin, P. A., Influence of hole transport interlayer on the electrochemical stability of perovskite solar cells, The European Materials Research Society (E-MRS) 2019 Fall Meeting, Warsaw, Poland, 16-19 September **2019** (oral talk)
5. Yamilova, O. R.; Luchkin, S. Yu.; Mangrulkar, M.; Fedotov, Yu. S.; Bredikhin, S. I.; Troshin, P. A., Electrochemical degradation pathways of lead halide based perovskites in thin films and solar cells, The European Materials Research Society (E-MRS) 2018 Fall

Meeting, Warsaw, Poland, 17-20 September **2018** (poster presentation) - Best Poster Prize

6. Yamilova, O. R.; Inasaridze, L. N.; Luchkin, S. Yu.; Dremova, N. N.; Stevenson, K. J.; Troshin, P. A., Towards understanding the electrochemical degradation pathways of perovskite materials thin films, The European Materials Research Society (E-MRS) 2017 Fall Meeting, Warsaw, Poland, 18-21 September **2017** (poster presentation)

Acknowledgements

This work could be accomplished only with the support and contributions from my colleagues from the research group of the Center for Energy Science and Technology in Skoltech, Institute of Solid State Physics of the Russian Academy of Sciences (ISSP RAS). I would like to acknowledge my scientific advisor Prof. Keith Stevenson, as well as my individual committee members professors Albert Nasibulin and Alexei Buchachenko for their help and advice.

I would like to thank my colleagues for their help and useful advice: Dr. Aleksandra Boldyreva, Artyom Novikov, Igor Gorokh, Marina Teplyakova, Dr. Sergey Tsarev and Artem Zaikin.

I want to acknowledge my colleagues who carried out some of the experiments featured in this Thesis. AFM was measured by Dr. Sergey Luchkin (SkolTech). ToF-SIMS measurements were performed by Dr. Yuri Fedotov (ISSP RAS) and Andrei Danilov (SkolTech).

I am grateful to my friends and family for their kind support.

Table of Contents

Abstract.....	3
Publications.....	5
Acknowledgements.....	8
Table of Contents.....	9
List of Symbols, Abbreviations	12
List of Figures.....	14
List of Tables	18
Chapter 1. Introduction	19
Chapter 2. Review of the Literature	21
2.1 PEROVSKITE PHOTOVOLTAICS – KEY ASPECTS	21
2.1.1 IMPORTANT DEFINITIONS	21
2.1.2 KEY CHARACTERISTICS.....	25
2.1.3 REQUIREMENTS AND PROBLEMS.....	27
2.2 ELECTROCHEMICAL DEGRADATION OF PEROVSKITE PHOTOVOLTAICS	28
2.2.1 ELECTROCHEMICAL DEGRADATION OF BULK PEROVSKITE MATERIALS.....	29
2.2.2 ELECTROCHEMICAL DEGRADATION OF PSCS	32
Chapter 3. Research objectives	35
Chapter 4. Experimental section	36
4.1 LATERAL DEVICE PREPARATION AND CHARACTERIZATION	36

4.1.1 PEROVSKITE MATERIALS PREPARATION.....	36
4.1.2 LATERAL TWO-TERMINAL DEVICE FABRICATION.....	37
4.1.3 CHRONOAMPEROMETRY MEASUREMENTS	38
4.1.4 AFM MEASUREMENTS	38
4.1.5 PL MAPPING	38
4.1.6 TOF-SIMS ANALYSIS OF LATERAL DEVICES	39
4.2 SOLAR CELLS FABRICATION, CHARACTERIZATION AND INVESTIGATION.....	40
4.2.1 HTL MATERIALS DEPOSITION METHODS.....	40
4.2.2 PEROVSKITE MATERIALS FILMS PREPARATION METHODS.....	41
4.2.3 ETL MATERIALS DEPOSITION METHODS	41
4.2.4 TOP ELECTRODES DEPOSITION METHODS.....	42
4.2.5 FABRICATION OF SOLAR CELLS	42
4.2.6 BIASING AND CHARACTERIZATION OF SOLAR CELLS.....	42
4.2.7 TOF-SIMS ANALYSIS OF SOLAR CELLS	43
Chapter 5. Results and discussion	44
5.1 DEFINING THE ELECTROCHEMICAL DEGRADATION MECHANISM USING MODEL PEROVSKITE MATERIAL CH ₃ NH ₃ PBI ₃	44
5.1.1 BULK MATERIAL BIASING AND ANALYSIS	44
5.1.2 SOLAR CELL BIASING AND TOF-SIMS ANALYSIS.....	48
5.1.3 MECHANISM DETERMINATION	56
5.1.4 CONCLUSION FOR THE FIRST STAGE	57

5.2 DEFINING THE MOST ELECTROCHEMICALLY STABLE PEROVSKITE MATERIAL DEPENDING ON CHEMICAL STRUCTURE.....	59
5.2.1 BULK MATERIAL BIASING AND COMPARISON.....	59
5.2.2 SOLAR CELLS TESTING	68
5.2.3 CONCLUSION FOR THE SECOND STAGE	70
5.3 DEVICE CONFIGURATION INFLUENCE ON ELECTROCHEMICAL STABILITY OF THE PSCS.....	70
5.3.1 INFLUENCE OF HOLE-TRANSPORT LAYERS ON ELECTROCHEMICAL STABILITY OF THE DEVICE	70
5.3.2 INFLUENCE OF ELECTRON-TRANSPORT LAYERS AND TOP ELECTRODES	83
5.3.3 CONCLUSION FOR THE THIRD STAGE.....	87
Chapter 6. Conclusions.....	89
Bibliography	91
Appendix A. Supplementary materials.....	111

List of Symbols, Abbreviations

Symbols:

FF – fill factor

J – current density (mA/cm²)

J_{SC} – short cut current density

PCE – power conversion efficiency

V – voltage (V)

V_{OC} – open current voltage

V_{MPP} – maximum power point voltage

Abbreviations:

AFM – atomic force microscopy

CTL – charge transport layer

DMF – dimethylformamide

DMSO – dimethylsulfoxide

ETL – electron transport layer

ETM – electron-transport material

EQE – external quantum efficiency

FA^+ – formamidinium cation $HC(NH_2)_2^+$

HTL – hole transport layer

HTM – hole-transport material

ITO – transparent electrode indium-tin oxide

MA^+ – methylammonium cation ($CH_3NH_3^+$)

MPP – maximum power point

PCBA – phenyl-C₆₁-butyric acid

PCBM – phenyl-C₆₁-butyric acid methyl ester

PEDOT:PSS – poly(ethylene-3,4-dioxythiophene): polystyrene sulfonate

PL – photoluminescence

PSC – perovskite solar cell

PTAA – polytriarylamine

PV – photovoltaic

ToF-SIMS – Time-of-flight secondary ion mass-spectrometry

List of Figures

Figure 1. A typical crystal structure of a perovskite. Reproduced with permission from ref. ²⁵ Copyright 2018, Springer Nature.	22
Figure 2. Mesoporous (a) and planar (b, c) perovskite solar cell configuration, including conventional n-i-p (b) and inverted p-i-n (c)	23
Figure 3. Typical <i>J-V</i> curve for perovskite solar cell with hysteresis effect between forward and reverse scan	24
Figure 4. Example of <i>J-V</i> curve with measured solar cell characteristics.....	25
Figure 5. Typical EQE curve	27
Figure 6. PCE drop depending on the external electric field demonstrated by S. Bae et al. Reproduced with permission from ref. ⁴⁹ Copyright 2016, ACS Publications.....	30
Figure 7. IR-microscopy for CH ₃ ⁺ migration monitoring under applied electric field in the publication of Y. Yuan et al. Reproduced with permission from ref. ⁵⁵ Copyright 2015, John Wiley & Sons	32
Figure 8. General layout of the lateral two-electrode device (a). Evolution of the current flowing through the channel of the lateral two-terminal device under potentiostatic polarization with 1 V/μm applied bias (b).	44
Figure 9. Optical microphotograph of the device channel before (left) and after (right) applying 1 V/μm bias for 340 h (a). PL mapping of the channel before (left) and after (right) applying 1 V/μm bias for 24h. (b) AFM for anode (c) and cathode (d) areas before (left) and after (right) applying 1 V/μm bias for 100 h.....	45

Figure 10. ToF-SIMS profiles of lateral two-terminal devices across the channel formed by MAPbI₃ semiconductor film before (reference) and after (biased) exposure to electric bias of 1 V/μm for 340 h. A ratio of ion yields is given to account for possible geometry effects: ²⁰⁴Pb⁺ normalized to I⁺ (a) and NH₃⁺ normalized to I⁺ (b)..... 47

Figure 11. Schematic layout of the p-i-n perovskite solar cell architecture (a). The evolution of the device performance under different external biases applied in forward direction (b) and the comparison of the device degradation kinetics under forward and reverse bias of 1.5 V (c)..... 49

Figure 12. Evolution of forward (solid lines) and reverse (dot lines) *J*-*V* curves at scan rates of 10 mV/s (a) and 100 mV/s (b) for device biased at the applied potential of 1.5 V in forward direction..... 51

Figure 13. ToF-SIMS chemical maps showing the distribution of the characteristic marker ions Pb⁺, I₂⁻ and CH₃NH₃⁺ in the reference cells and devices exposed to 2 V under forward bias for 160 h..... 53

Figure 14. Cyclic voltammograms for 0.1 M solution of NaClO₄ in DMF as illustration of the DMF electrochemical stability window (from -1200 mV to 1100 mV) and 0.01 M solution of MAPbI₃ in DMF measured with various cathodic potential cutoffs 55

Figure 15. Schematic representation of the revealed mechanism of the field-induced electrochemical decomposition of MAPbI₃ 56

Figure 16. Evolution of the current flowing through the channel of the lateral two-terminal device under potentiostatic polarization with 1 V/μm applied bias for various perovskite materials. 60

Figure 17. Evolution of PL signal in the channel of lateral two-electrode device during the electric bias exposure for various perovskite materials. Optical photos of corresponding channels for every material after the 120 h biasing are presented on the left. Channels on all figures oriented horizontally, with cathode on top position and anode in bottom position. 62

Figure 18-1. ToF-SIMS profiles of lateral two-terminal devices for across the channel formed by corresponding (noted on the left) perovskite semiconductor film MAPbI_3 (a) $\text{MA}_{0.15}\text{Cs}_{0.1}\text{FA}_{0.75}\text{PbI}_3$ (b) $\text{Cs}_{0.15}\text{FA}_{0.85}\text{PbI}_3$ (c) before (reference) and after (biased) exposure to electric bias of $1 \text{ V}/\mu\text{m}$ for 300 h. A ratio of ion yields is given to account for possible geometry effects. 64

Figure 18-2. ToF-SIMS profiles of lateral two-terminal devices for across the channel formed by corresponding (noted on the left) perovskite semiconductor film $\text{Cs}_{0.125}\text{FA}_{0.875}\text{PbBr}_{0.375}\text{I}_{2.625}$ (a) CsPbI_2Br (b) before (reference) and after (biased) exposure to electric bias of $1 \text{ V}/\mu\text{m}$ for 300 h. A ratio of ion yields is given to account for possible geometry effects. 65

Figure 19. AFM data for corresponding (marked on the left) perovskite materials before and after biasing for 80 hours near both electrodes. 67

Figure 20. N-i-p solar cells device configuration (a). Normalized average PCE evolution for the batches of solar cells with different perovskite photoactive layers..... 69

Figure 21. Schematic structure of solar cells used in experiments (a). Chemical structures of organic HTMs (b) 71

Figure 22. Evolution of normalized PCE during the “stepwise” biasing of solar cells with various HTLs (a). Evolution of the efficiency of PSCs with PTAA as HTL under applied electric bias ($V_{MPP} = 0.7$ V, $V_{OC} = 1$ V, $I_{MPP} = 18.3$ mA/cm ² , $E_g/q = 1.55$ V) (b).....	73
Figure 23. Evolution of normalized average efficiency for solar cells with various HTLs under constant 1V electric bias. HTLs are ranged from the best (top) to worst (bottom)....	76
Figure 24. ToF-SIMS ions profiles for fresh and biased (2000 h) samples of solar cells with NiO _x and NiO _x PTAA as HTLs	81
Figure 25. Optical photos of the solar cell backsides after 2000 h under constant biasing..	82
Figure 26. Optical microscope images of the top silver electrode edges before and after biasing for 2000 h	83
Figure 27. Schematic structure of solar cells used in the experiment of ETL variation (a). Evolution of normalized average PCE of solar cells with various ETLs (b).....	85
Figure 28. Schematic structure of solar cells used in the experiment of top electrode variation (a). Evolution of normalized average PCE of solar cells with various electrode materials (b).	86

List of Tables

Table 1. Perovskite solutions preparation.....	36
Table 2. Perovskite films deposition.....	37
Table 3. Stability rating of all used HTLs depending on their ability to boost the device stability and their characteristics.....	80
Table 4. Average initial PCEs for investigated systems with various top electrodes.....	86

Chapter 1. Introduction

Climate change and ecological problems spread all over the world hand in hand with the urgency of sustainable development and renewable energy sources implementation. The adoption of photovoltaics is one of the emerging players staying at the forefront of energy transformation and decarbonization.

Among three generations of photovoltaic (PV) devices the last one based on hybrid emerging technologies appears to be the most promising in terms of production, prime cost, functionality and recycling. But problems regarding efficiency and stability slow down the extending of the new technology on the market.

The so-called perovskite photovoltaics appeared in 2009 year with the pioneering work of Prof. Miyasaka et al.¹ This third-generation technology implies photoactive materials based on complex organo-inorganic lead halides with the perovskite structure. Just in thirteen years perovskite solar cells (PSCs) power conversion efficiency (PCE) skyrocketed from 3.8%¹ up to recent record 25.7% efficiency,² which allows this technology to be considered as a strong competitor to traditional silicon and thin film chalcogenide solar cells.^{3,4} Besides, the photoactive layer in perovskite solar cells is applicable for low-cost solution-based printing fabrication and further development of large-scale roll-to-roll manufacturing.^{5,6} Other advantages to be mentioned are possibility for implication in flexible electronic devices,⁷ high power-per-weight values, appropriateness for wearable electronics and space,^{8,9} tunability of optical properties for implementation in tandem solar cells and indoor photovoltaics.¹⁰⁻¹³ But one of the most

important remaining obstacles is a short lifetime of the devices under realistic operating conditions.

To reach the commercially viable stability benchmarks, the absorber material and other device components should sustain several internal and external stressing factors. Extrinsic degradation causes include moisture¹⁴⁻¹⁷ and oxygen.^{18,19} These aspects are widely discussed in the literature, but due to the development of encapsulation techniques extrinsic causes become less and less important.²⁰ On the contrary, intrinsic degradation pathways caused by the action of sunlight,²¹ elevated temperatures^{22,23} and electric field²⁴ induce the most considerable changes in PSC efficiency. Unfortunately, among all aforementioned factors the bias-induced degradation processes remain the least elucidated.

Thus, we decided to dedicate this Thesis to the investigation of the field-induced degradation pathways of complex organo-inorganic lead halides with a perovskite structure and solar cells based on these materials. Our goal is to reveal the general degradation pathway in perovskite thin films, understand the influence of chemical composition of perovskite on its electrochemical stability. And finally highlight main factors influencing the stability of the operating solar cell.

We hope this work will pave the way towards the development of electrochemically stable perovskite solar cells.

Chapter 2. Literature review

2.1 Perovskite photovoltaics – key aspects

2.1.1 Important definitions

In the last decade, perovskite photovoltaics gained enormous attention of scientific community due to outstanding characteristics, unlabored fabrication process and remarkable efficiency development rate. This technology employs a type of solar cells where inorganic or hybrid organo-inorganic complex lead halides with a perovskite structure act as a photoactive layer.²⁵

In general, any material with crystal structure described by general chemical formula ABX_3 is commonly called perovskite. This name includes tremendous number of materials with various properties and applications. They can form crystals with a cubic, orthorhombic, tetragonal structure and others. The structure of most promising perovskite material for photovoltaic applications is demonstrated in Figure 1.^{25,26} The A here is an inorganic or organic cation, typically methylammonium (MA^+), formamidinium (FA^+) or Cs^+ , B is a divalent metal atom, mostly Pb^{2+} , X is a I^- , Br^- or rarely Cl^- halogen ion. A prototypical perovskite material used in photovoltaic devices is methylammonium lead iodide, $CH_3NH_3PbI_3$.

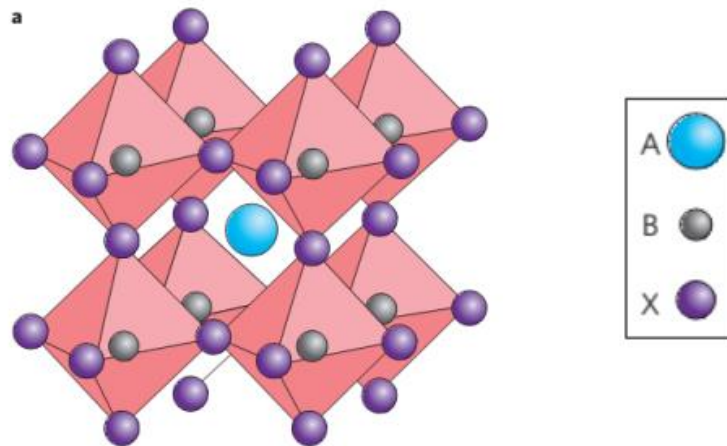


Figure 1. A typical crystal structure of a perovskite. Reproduced with permission from ref.²⁵ Copyright 2018, Springer Nature.

Organo-inorganic perovskite materials of a similar structure were first mentioned in 1884, however, only in 2009 professor T. Miyasaka et al. used perovskite materials $\text{CH}_3\text{NH}_3\text{PbI}_3$ and $\text{CH}_3\text{NH}_3\text{PbBr}_3$ as a new type of light absorbers,¹ paving the way for further research in this field.

Perovskite materials exhibit excellent electronic properties, for example, model material $\text{CH}_3\text{NH}_3\text{PbI}_3$ has exciton binding energy around 2 meV, charge carrier diffusion length 175 μm , charge carrier mobility $> 100 \text{ cm}^2/\text{V}\cdot\text{s}$.²⁷ It should be also mentioned that crystals with a perovskite structure have a very low density of traps, which is comparable to the properties of high-quality crystalline silicon.²¹ Due to these qualities, perovskites became promising materials for implementation in third generation solar cells.

First perovskite solar cells were based on a well-known technology of dye sensitized solar cells production with the mesoporous structure (Figure 2a).²⁸ In

mesoporous solar cells, the bottom layer is a conductive transparent electrode deposited on a glass substrate. An electron transport layer (ETL) applied over it is a nanoporous metal oxide (TiO_2 or Al_2O_3), forming a scaffold and then filled with a photoactive perovskite material. Then a hole transport layer (HTL) and metal electrodes (traditionally gold or silver) are sequentially fabricated. Mesoporous oxide layers improve the crystallization of the perovskite layer, resulting in enhanced efficiency of these solar cells up to 9.7% in 2012.²⁸

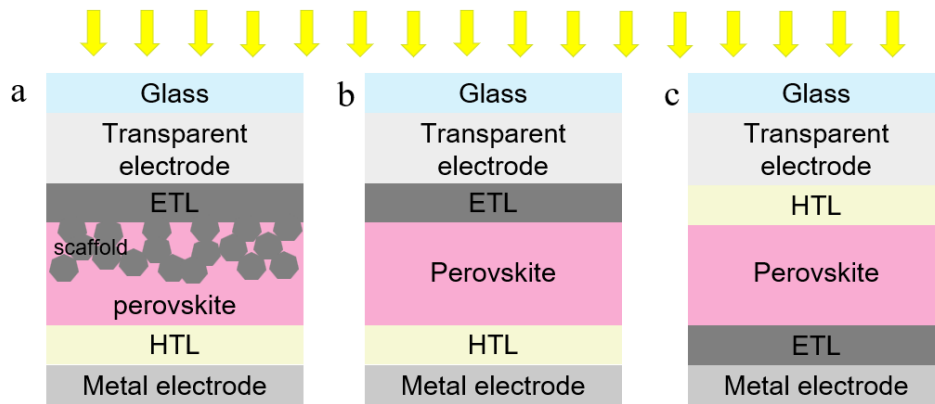


Figure 2. Mesoporous (a) and planar (b,c) perovskite solar cell configuration, including conventional n-i-p (b) and inverted p-i-n(c).

Further development of the PSCs fabrication process led to the emerging of solar cells with a planar structure (Figure 2b,c), where a thin film ETL was used instead of the nanoporous material.²⁹ The manufacturing process of planar structure perovskite solar cells is much simpler and cheaper compared to the mesoporous solar cells and thus it is more popular recently.³⁰ Besides, by selecting the optimal materials for each of the layers, scientists managed to increase the PCE of devices up to current record 25.7%.²

The shift from mesoporous to the planar structure instigated the evolution of conventional and inverted PSCs.³¹⁻³³ A conventional n-i-p structure implies a subsequence of transparent electron-collecting electrode – ETL – perovskite – HTL – top metal electrode. The main disadvantage for the n-i-p structure is a parasitic effect of hysteresis in the J - V curves (Figure 3),^{34,35} caused by ions and vacancies migration, charge traps and polarization effects.³⁶⁻³⁹ This effect can reduce the extracted power of the operating solar cell. Thus, the inverted p-i-n structure became one of the solutions to avoid undesirable hysteresis.⁴⁰ An inverted p-i-n structure has an opposite subsequence of transparent electrode – HTL – perovskite – ETL – top electron-collecting metal electrode. An inverted design also exploits low temperatures $< 150^{\circ}\text{C}$ and simple solution-based processing for all charge transport layers (CTLs).^{32,40,41}

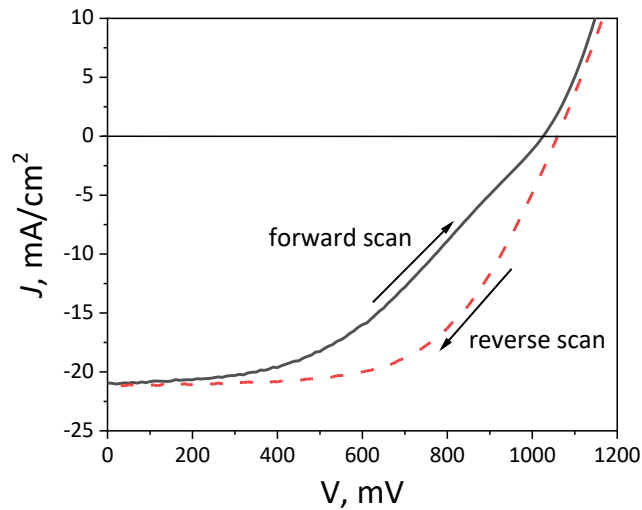


Figure 3. Typical J - V curve for perovskite solar cell with hysteresis effect between forward and reverse scan.

2.1.2 Key characteristics

The current-voltage (J - V) characteristic of solar cells like in Figure 3 is typically measured in laboratory conditions after fabrication. The standard test is carried out with solar radiation of 1000 W/m^2 at an ambient temperature of 25°C , as at a latitude of 45° .

The extreme points of the J - V curve, at which the power taken from the battery goes to zero, are demonstrated in Figure 4. Open circuit voltage - V_{OC} is the maximum available voltage at the output of the battery with an open load circuit. The current density at a short-circuited load circuit - J_{SC} - is, respectively, the current at zero output voltage.

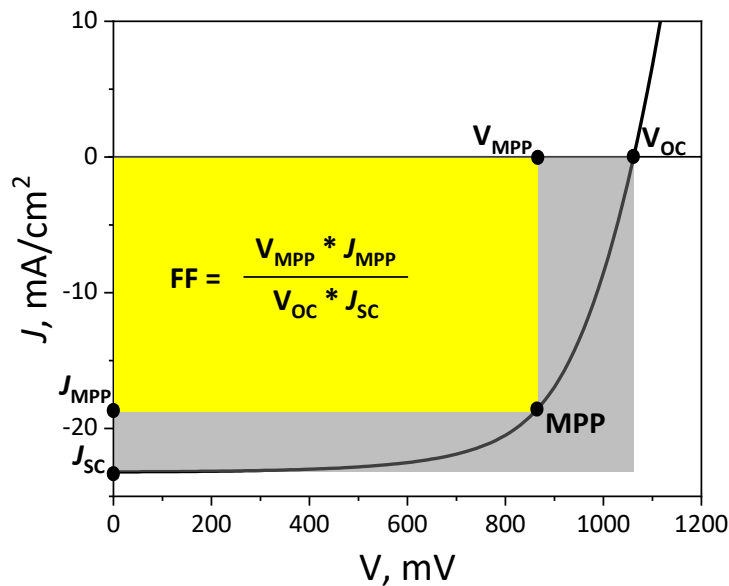


Figure 4. Example of J - V curve with measured solar cell characteristics.

In realistic solar cell operating conditions, the PV device always works in some mode between these two points. In the optimal situation, the MPP point corresponds to

the maximum load power. The rated voltage for the maximum power point is V_{MPP} and the rated current for that point is I_{MPP} . At this point, the efficiency of the solar cell should be determined according to the formula:

$$PCE = P_{\text{electrical}}/P_{\text{light}} = I_{MPP} \cdot V_{MPP}/P_{\text{light}} = I_{SC} \cdot V_{OC} \cdot FF/P_{\text{light}}$$

Here the FF is a fill factor of the solar cell, determined as the relation of the yellow and gray rectangle's areas:

$$FF = (J_{MPP} \cdot V_{MPP})/(J_{SC} \cdot V_{OC})$$

Single solar cell in the laboratory-driven model experiments operates at the maximum power point, which gives the best efficiency. However, in realistic conditions the solar cell in the assembled module can work at any point at the J - V curve. This point is not chosen by the module, but by the electrical characteristics of the circuit to which this module is connected.

Another important parameter of solar cell is an external quantum efficiency (EQE). This parameter defines the number of electrons extracted from the photoactive layer divided by the number of photons irradiating the device. Typical EQE is presented in Figure 5. In ideal situation the curve could be represented by flat line at 100% EQE, and this would correspond to the solar cell absorbing and converting into energy 100% of sunlight without any losses. But in real life the decrease in blue light area is usually caused by front surface recombination, while the decrease in the red light area by low diffusion length and reduced absorption of long-wavelength photons. And reflections cause reduction in the middle area.

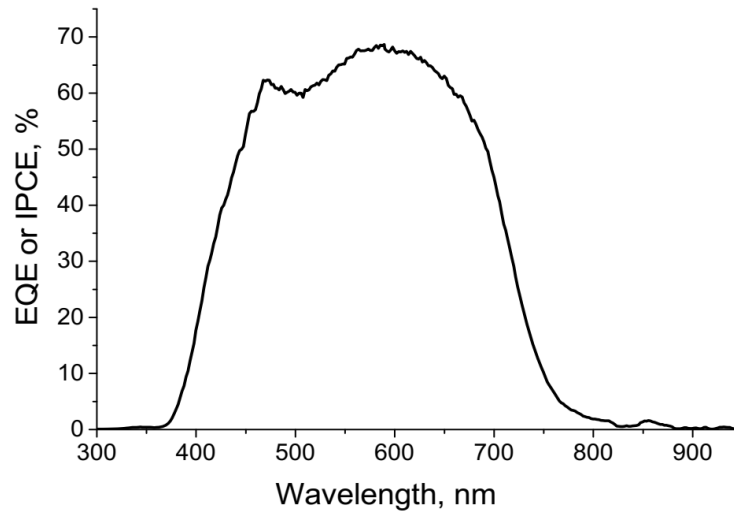


Figure 5. Typical EQE curve

2.1.3 Requirements and problems

For successful commercialization any photovoltaic technology should satisfy several criteria. High efficiency, low production cost, long lifetime of the device are necessary to reduce the obtained energy price per one kW·h. Functionality and recycling after usage are also considered as important factors since functionality involves possibility of implementation in various devices and recycling is dedicated to reducing of the total amount of human wastes.

First generation solar cells made of mono- and polycrystalline silicon demonstrated surpassing efficiency more than 20% for market samples and stability around 20 years but fell behind in all leftover parameters. Fabrication of monocrystalline silicon requires high temperatures exceeding 1500°C during the Chochralski method, resulting in high energy demands and fabrication costs. Besides, processing includes aggressive and toxic substances like HCl, H₂SO₄, HF, SiCl₄. The weight of the obtained

solar panels is very high, which puts restrictions on functionality. And the recycling of silicon for now is limited because of economical inexpediency.

Second generation thin-film technologies such as amorphous silicon, cadmium telluride and copper-indium-gallium-selenide are all displaying quite average level for all parameters. And the brightest representatives of third generation photovoltaics such as dye-sensitized, organic and quantum-dot solar cells have always been the outsiders in terms of efficiency and stability – the most important criteria. But they excel at functionality, recycling, production cost.⁴²

Progress in perovskite photovoltaics made it the best third-generation technology in terms of efficiency, on par with the best monocrystalline silicon. Thus, it has the potential to become the main rival for first generation photovoltaics, which now occupies more than 85% of the world market. But extremely low operational stability of perovskite solar cells due to degradation processes remains one of the most important problems hindering the further development and market implementation.

2.2 Electrochemical degradation of perovskite photovoltaics

Degradation of photoactive perovskite materials is a set of physicochemical processes occurring during their storage, processing, operation which leads to a change in the initial properties of the device. The main role in the process of photoactive materials degradation is played by such factors as: sunlight, temperature, electric field, mechanical impact, chemically aggressive substances. Depending on the prevailing factor photodegradation, thermodegradation, electrodegradation, mechanical and chemical

degradations are distinguished. Great damage is usually caused by the influence of such aggressive factors as oxygen and air moisture, leading to the chemical transformations of the material, reversible and irreversible changes in its physical properties. Among all mentioned factors the influence of electric field remains the least elucidated despite its significance due to the built-in and photo-induced potentials that are always present in the operating device.

Perovskite materials and solar cells degradation depends on a large number of external and internal factors. The latter are due to the properties of the material, its structure and the fabrication method. For research purposes and for accelerated and forced tests, the degradation of perovskite materials is studied under artificial conditions simulating operating one. This makes possible to obtain quantitative information about the individual stages of the process, to establish the reliability of ideas about its mechanism and about the change in time of practically important properties.

2.2.1 Electrochemical degradation of bulk perovskite materials

It was previously demonstrated that, due to the low activation energy in organic-inorganic complex lead halides, ion migration can easily proceed during the voltage application, which screens the external electric field.⁴³⁻⁴⁵ The accumulated mobile ions initiate chemical reactions, which can also be accelerated by heating and/or light irradiation.^{46,47}

In addition to the migration of vacancy ions, an external electric field in combination with exposure to light can also initiate an electrochemical reaction in a

perovskite material.⁴⁸ Previous studies have shown that the model perovskite material MAPbI₃ is an electrochemically active system with mobile methylammonium cations and iodide anions.

Also, by Soohyun Bae et al. the appearance of an external electric field during the operation of a perovskite solar battery was confirmed.⁴⁹ They demonstrated that an external electric field initiates the migration of ions in the perovskite layer, which ultimately leads to a rapid drop in the PCE of solar cells. Thus, the stability of perovskite solar cells is closely related to the current-voltage characteristics of the perovskite material and its electrochemical stability (Figure 6).

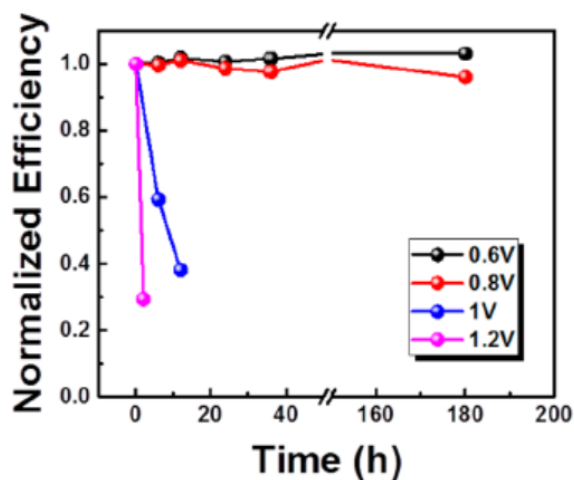


Figure 6. PCE drop depending on the external electric field demonstrated by S. Bae et al. Reproduced with permission from ref.⁴⁹ Copyright 2016, ACS Publications.

The electric field applied to perovskite films might lead to realization of diverse electrochemical degradation pathways, which are still poorly investigated.^{24,50-53} While a plenty of different bias-induced effects have been observed, no unambiguous conclusions on their mechanisms are usually provided. For example, applying electric bias to the lateral two-terminal devices with the MAPbI₃ semiconductor layer leads to visible changes in the film structure near the gold contacts appearing within the first minutes after applying bias,^{49,54} while no convincing mechanisms explaining this effect were reported. A deeper insight was achieved using photothermal infrared (PTIR) microscopy revealing the field-induced migration of MA⁺ to the cathode thus evidencing that not only halide anions but also organic cations can contribute to the ionic conductivity of lead halide perovskites (Figure 7).⁵⁵ Performing similar experiments at elevated temperatures led to the formation of the PbI₂ stripe near the anode, which was slowly moving toward the cathode thus evidencing methylammonium iodide exchange between the MAPbI₃ and PbI₂ due to the I⁻ migration in electric field.⁵⁶ Performing similar experiments in ambient air allowed identifying some irreversible degradation of MAPbI₃ with the formation of the PbI₂ phase starting from cathode.⁵⁴ While the aforementioned effects were observed under very different conditions, all observations suggest that the material degradation is associated with the ion migration leaving unclarified further mechanistic details.⁵⁷⁻⁵⁹ On the contrary, a pathway of the field-induced degradation of MAPbI₃ was hypothesized in the publication of L. Frolova et al.,⁴⁸ while no unambiguous evidence was provided thus leaving this aspect under discussion.

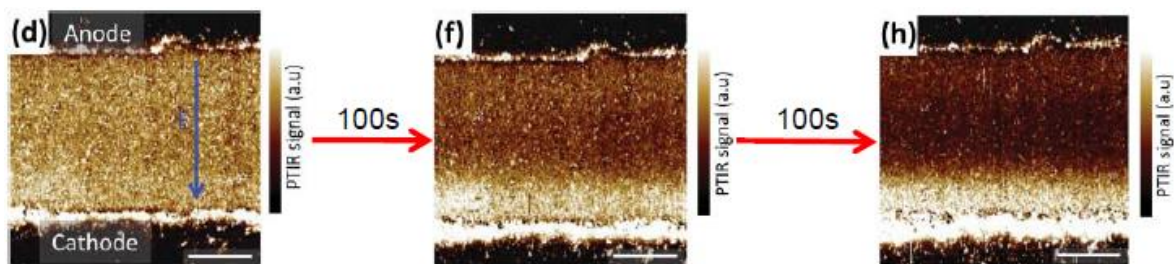


Figure 7. IR-microscopy for CH_3^+ migration monitoring under applied electric field in the publication of Y. Yuan et al. Reproduced with permission from ref.⁵⁵ Copyright 2015,

John Wiley & Sons.

The electrochemical stability of perovskite films can also be impacted by the presence of adjacent functional (e.g. charge transport) layers. In particular, probe microscopy measurements performed for MAPbI_3 films deposited on tin-doped indium oxide (ITO) substrates coupled with the subsequent ToF-SIMS chemical analysis revealed a field-induced interfacial degradation accompanied by the diffusion of the perovskite components into ITO and *vice versa*.⁶⁰ High-resolution electron microscopy and EDX analysis revealed field-induced oxygen migration from TiO_x electron-transport layer to the perovskite film, which can be reversed by applying a bias of opposite polarity.⁶¹

2.2.2 Electrochemical degradation of PSCs

Solar cell always operates under electric field, usually equal to the maximum power point (MPP) with some deviations in multi-cell devices and tandems.⁶² Electric field can exert the performance of the device in different manner: it can demonstrate zero

impact on solar cell characteristics^{63,64} or even improve the efficiency,⁶⁵⁻⁶⁷ but in majority of the cases it leads to the degradation of the device.⁶²⁻⁷⁴ This indicates the possibility of various degradation pathways manifestation depending on the environment and conditions. However, the impact of the bias on the perovskite solar cells obviously depends on the strength of the generated electric field and exposure time.

Empirical screening of different regimes revealed that 1 V represents a kind of threshold potential. Devices are mostly stable under bias below 1 V, although when it goes above 1 V a rapid and irreversible decay of the performance was observed.⁴⁹ While the mechanisms of the observed effects are still not understood, a plethora of possible mechanisms of PSCs bias-induced degradation under different conditions was proposed.

Those suggestions include ion migration leading to accumulation of ions at the interfaces with the charge transport interlayers,^{49,62,64,69,75} iodide penetration into the charge transport layer and PbI_2 formation in perovskite layer,⁶⁸ charge accumulation at the interface,^{66,71} phase segregation,⁷⁰ reversible migration of oxygen from the adjacent charge-transport layer into perovskite.⁷² Such a multitude of observations and conclusions is mostly caused by the variation of experimental conditions: different solar cell structures including both n-i-p and p-i-n with various charge transport materials; various perovskites $\text{MAPbI}_x\text{Cl}_{3-x}$,⁶⁵ MAPbI_3 ,^{63,64,66-69,71,72,74} mixed halide^{62,73} and even rubidium-containing perovskite;⁷⁰ discrepant environment – combination of factors like bias-temperature,⁶⁶ bias-light,^{69,70,73} bias-air,^{63,64} bias-moisture.⁶⁴ All of these makes it difficult to differentiate the clear bias-induced degradation mechanism. And majority of

publications provides only short time biasing experiments, excluding long-term effects of applied electric field.^{49,65,68,72,74}

Observing all the publications on the topic, we firmly believe that electrochemical stability of solar cell is not only related to the degradation of the active material itself but also strongly influenced by adjacent charge transport layers and even metal electrodes. Many publications demonstrate the possibility of chemical interaction between perovskite and neighboring layer, including ion accumulation and structural changes on the interface.^{60,66,68,69,72} For example, reversible field-induced oxygen migration from TiO_x was revealed by electron microscopy and EDX.⁶¹ Mutual diffusion of perovskite and ITO layers under applied electric field was observed with time-of-flight secondary ion mass spectrometry (ToF-SIMS).⁶⁰ Although until now there are no publications dedicated to systematic investigation of charge-transport materials and electrodes influence on electrochemical stability of PSCs, only trial was performed by Craig H. Swartz et al. to compare hole-transport materials (HTMs) poly[bis(4-phenyl)(2,4,6-trimethylphenyl)amine (PTAA) and CuI.⁶⁷

Chapter 3. Research objectives

The presented overview features that understanding the degradation mechanisms of perovskite materials and perovskite solar cells is a very important task from a scientific point of view, which requires a systematic study of a structurally different materials and device configurations, which will enable further directed design of materials for highly efficient and stable solar cells.

This Thesis is dedicated to the investigation of electrochemical degradation of complex lead halides and photovoltaic devices on their basis. Objectives of this work included:

- determination of the perovskite material electrochemical degradation pathway, on the example of the classical material $\text{CH}_3\text{NH}_3\text{PbI}_3$.
- according to the detected pathway, defining the chemical structure of the most electrochemically stable perovskite material.
- comparative analysis of different adjacent charge-transport materials and metal electrodes to understand the impact of their nature on electrochemical stability of the complete device.

Chapter 4. Experimental section

4.1 Lateral device preparation and characterization

4.1.1 Perovskite materials preparation

All perovskite solutions for further experiments were prepared according to the literature sources with minor optimizations. Masses of reagents (commercially available) and specific conditions are written in Table 1.

Table 1. Perovskite solutions preparation conditions

Ref.	Material	Reagents and masses, g	Solvents and volumes, ml	Additional conditions
[48]	MAPbI ₃	MAI – 0.4452 PbI ₂ – 1.2908	DMF – 1.7 NMP – 0.3	Ultrasonication for 5 minutes, no heating
[76]	MA _{0.15} Cs _{0.1} FA _{0.75} PbI ₃	MAI – 0.0668 CsI – 0.0728 FAI – 0.3612 PbI ₂ – 1.2908	DMF – 1.6 DMSO – 0.4	Ultrasonication for 5 minutes, no heating
[102]	Cs _{0.15} FA _{0.85} PbI ₃	CsI – 0.1092 FAI – 0.4094 PbI ₂ – 1.2908	DMF – 1.6 DMSO – 0.4	Ultrasonication for 5 minutes, no heating
[77]	Cs _{0.12} FA _{0.8} PbI _{2.92}	CsI – 0.099 FAI – 0.435 PbI ₂ – 1.474	DMF – 1.7 DMSO – 0.3	Ultrasonication for 5 minutes, no heating
[78]	Rb _{0.1} Cs _{0.15} FA _{0.75} PbI ₃	RbI – 0.0478 CsI – 0.1169 FAI – 0.6578 PbI ₂ – 2.0745	DMF – 2.4 DMSO – 0.6	Ultrasonication for 5 minutes, no heating
[79]	Cs _{0.125} FA _{0.875} PbBr _{0.375} I _{2.625}	CsBr – 0.052 FAI – 0.3 PbI ₂ – 0.8 PbBr ₂ – 0.092	DMF – 0.96 DMSO – 0.14	Ultrasonication for 5 minutes, no heating
[80]	CsPbI ₂ Br	CsBr – 0.0852 PbI ₂ – 0.1844	DMF – 1	Ultrasonication for 5 minutes, no heating
[81]	MAPbI _x Cl _{3-x}	MAI – 0.256 PbCl ₂ – 0.149	DMF – 1	Heating at 90°C and stirring overnight

All preparation methods mentioned above were previously reported in the literature and demonstrated affordable characteristics and comparatively high stability of obtained films under various degradation factors. Chemical formulas represent only ratio of initial reagents and may not correspond to the actual crystal structure of the material. Nevertheless, according to the XRD measurements of the films, they fully correspond to the required phases of the materials (Figure A1 in the Appendix A, Supplementary materials).

4.1.2 Lateral two-terminal device fabrication

Table 2. Perovskite films deposition conditions

Material	Rotation speed, rpm	Antisolvent	Annealing temperature and time
MAPbI ₃	4000	Toluene	80°C, 5 min
MA _{0.15} Cs _{0.1} FA _{0.75} PbI ₃	4000	Toluene	100°C, 5 min
Cs _{0.15} FA _{0.85} PbI ₃	4000	Toluene	100°C, 10 min
Cs _{0.12} FA _{0.8} PbI _{2.92}	4000	Toluene	100°C, 10 min
Rb _{0.1} Cs _{0.15} FA _{0.75} PbI ₃	3500	Toluene	95°C, 10 min
Cs _{0.125} FA _{0.875} PbBr _{0.375} I _{2.625}	4000	Toluene	140°C, 10 min
CsPbI ₂ Br	1200	No antisolvent	100°C, 2 min
MAPbI _x Cl _{3-x}	4000	No antisolvent	90°C, 1.5 h

Glass substrates 15 × 15 mm size were sequentially cleaned by sonication in deionized water, acetone and isopropanol for 10 min each and then cleaned for 5 min by oxygen plasma treatment. Perovskite films were spin-coated in a nitrogen-filled glovebox

from the solutions prepared earlier according to the conditions in Table 2 and filtered. Afterwards, the films were annealed at 100 °C for 1 min. Gold electrodes were evaporated on top via shadow mask (channel length and width are 200 μm and 2 mm, respectively).

4.1.3 Chronoamperometry measurements

Chronoamperometry measurements were carried out using a Keithley 236 and Keithley 2612A source meters for continuously recording the current flowing through the channel of the devices under constant applied voltage density ~ 1 V/μm.

4.1.4 AFM measurements

Measurements were performed using Cypher EX AFM (Asylum Research, CA, US) operating under inert Ar atmosphere in MBraun glovebox with O₂ < 0.1 ppm and H₂O < 1 ppm.

4.1.5 PL mapping

Photoluminescence (PL) mapping was carried out using Automatic Research GmbH LBIC+PL+EL microscopy setup with Horiba spectrometer. The measurements were performed under anoxic conditions for encapsulated devices at room temperature. The sample was mounted on an X-Y stage with a travel distance of 150 mm for both axes and irradiated with the 532 nm green laser with the beam diameter of ~ 0.01 mm on the sample surface and power of 229 μW. The emission spectrum was analyzed using

Sincerity iHR320 imaging monochromator (Focal length 320 mm, entrance aperture ratio f/4.1) with grating at 900 nm, slit entrance of 0.7 mm and exposure time of 0.3 seconds for each point with delay of 250 ms. Right after the measurement, the optical photographs of the degraded lateral device channel were made.

4.1.6 ToF-SIMS analysis of lateral devices

For depth profiling and chemical mapping we used a TOF.SIMS 5-100P instrument (ION-TOF GmbH, Germany, 2007). During depth profiling, the sputtering ion beam (O^{2+} at 2000 eV ion energy and 480 nA measured sample current) was raster scanned over an area of $600 \times 600 \mu m^2$. The analysis ion beam consisting of Bi^+ pulses (25 keV ion energy, 20 ns pulse duration, 3.5 pA measured sample current) was set in the spectroscopy (high-current bunched) mode and raster scanned over a $400 \times 400 \mu m^2$ area (256×256 pixels) centered within the O^{2+} sputtered area at the regressing surface. The depth profiles were acquired in noninterlaced mode, that is, sequential sputtering and analysis, at a base pressure of 3×10^{-8} mbar. All mass spectra were acquired in positive polarity while the mass resolution was > 7000 ($m/\delta m$) for all fragments of interest. After data collection, the total area images were individually reconstructed and analyzed. Binning was used to obtain 128×128 pixel images from raw 256×256 pixel data. The reconstructed ion profiles were normalized to each other to allow for a fair comparison of relative concentrations.

4.2 Solar cells fabrication, characterization and investigation

4.2.1 HTL materials deposition methods

- PEDOT:PSS water solution was spincoated in the air atmosphere at 3000 rpm and then annealed at 165°C for 20 min.
- NiO_x (20 mg/ml in H₂O) was sonicated for 4 h, filtered and spincoated in the air at 4000 rpm three times with 10 second interval, then annealed at 100°C for 5 min in the air with following annealing at 140°C for 10 min in the glovebox.
- CuSCN (10 mg/ml DPS) was spincoated at 4000 rpm in a glovebox, heated at 100°C for 10 min.
- CuI (10 mg/ml in acetonitrile) was spincoated at 4000 rpm in a glovebox, heated at 100°C for 10 min.
- CuO_x: CuI (10 mg/ml in acetonitrile) was spincoated in the air at 6000 rpm, then soaked in KOH 10 mg/ml water solution for 5 seconds, washed in distilled water, dried and annealed at 50°C for 5 min, then annealed in a glovebox at 100°C for 10 min.
- V₂O₅ was deposited via thermal evaporation, 20 nm thickness.
- PTAA (4 mg/ml in toluene) was spincoated in a glovebox at 4500 rpm and then annealed at 100°C for 5 min.

4.2.2 Perovskite materials films preparation methods

All perovskite solutions were prepared and films were deposited as described in 4.1.1 and 4.1.2

4.2.3 ETL materials deposition methods

- SnO₂ (10% solution in H₂O) was filtered and spincoated in the air at 5000 rpm two times with 20 second interval, then annealed at 175°C for 10 min in the air with following annealing at 150°C for 5 min in the glovebox.
- TiO₂: mixture of 210 µl TTIP and 21 µl HCl in 3 ml of isopropanol was sonicated for 3 minutes, filtered and spincoated in the air at 3000 rpm, then annealed at 200°C for 20 min on the hotplate in the air with following annealing at 450°C for 20 min in the muffle oven.
- In₂O₃: pure In was deposited via thermal evaporation in vacuum chamber. Thickness of the film was 20 nm. Then films were annealed in the muffle oven for 20 min at the temperature 400°C.
- ZnO: mixture of 100 mg zinc acetate, 1 ml of 2-metoxyethanol and 33 µl of monoethanolamide was sonicated for 3 minutes, filtered and spincoated in the air at 6000 rpm, then annealed at 100°C for 10 min on the hotplate in the air with following annealing at 200°C for 60 min.
- PCBM (30 mg/ml in chlorobenzene) hot 70°C solution was spincoated in a glovebox at 3000 rpm without following annealing.
- PCBA (0.2 mg/ml in chlorobenzene) was spincoated in a glovebox at 3500 rpm and then annealed at 100°C for 5 min.

4.2.4 Top electrodes deposition methods

All electrodes were deposited on top of the device via thermal evaporation of metal through shadow mask. Thicknesses were 200 nm for n-i-p device configuration (Al, Ag, Au, Bi, Mn, Co, Ni, Cr and Cu) and for p-i-n device configuration we used sequentially 20 nm of Mg and 180 nm of Ag electrodes.

4.2.5 Fabrication of solar cells

ITO substrates were sequentially cleaned by sonication in deionized water, acetone and isopropanol for 10 min each and then cleaned for 5 min by oxygen plasma treatment. Then required layers were deposited sequentially according to the device configuration. HTL-perovskite-ETL-top electrode for p-i-n devices and ETL-perovskite-HTL-top electrode for n-i-p devices.

4.2.6 Biasing and characterization of solar cells

All aging experiments were performed in a dedicated nitrogen glove box with O₂ and H₂O levels below 0.1 ppm. The biasing process for prepared devices was carried out using a Keithley 236 and Keithley 2612A source meters for constant applied voltage. The current-voltage characteristics of the devices were measured in inert nitrogen atmosphere inside the glove box under simulated AM1.5G illumination (100 mW/cm²) provided by a Verasol AAA class solar simulator (Newport) and using Advantest 6240A source measurement units.

4.2.7 ToF-SIMS analysis of solar cells

For depth profiling we used a TOF.SIMS 5-100P instrument (ION-TOF GmbH, Germany, 2007). During depth profiling, the sputtering ion beam (O^{2+} at 2000 eV ion energy and 420 nA measured sample current) was raster scanned over an area of $350 \times 350 \mu m^2$. The analysis ion beam consisting of Bi^+ pulses (25 keV ion energy, 20 ns pulse duration, 3.5 pA measured sample current) was set in the spectroscopy (high-current bunched) mode and raster scanned over a $200 \times 200 \mu m^2$ area (256×256 pixels) centered within the O^{2+} sputtered area at the regressing surface. The depth profiles were acquired in noninterlaced mode, that is, sequential sputtering (2 seconds), pause (0.3 seconds) and analysis (2 frames), at a base pressure of $3 \cdot 10^{-8}$ mbar. Electron 20 eV gun was used for charge compensation. All mass spectra were acquired in positive polarity while the mass resolution was > 7000 ($m/\delta m$) for all fragments of interest. After data collection, the total area images were individually reconstructed and analyzed.

Chapter 5. Results and discussion

5.1 Defining the electrochemical degradation mechanism using model perovskite material $\text{CH}_3\text{NH}_3\text{PbI}_3$

5.1.1 Bulk material biasing and analysis

In the first stage of the work, lateral two-electrode devices were fabricated using MAPbI_3 films deposited on chemically inert soda lime glass substrates and gold contacts were evaporated through a shadow mask defining the channel length of $\sim 200\ \mu\text{m}$ (Figure 8a). The electric field of $1\ \text{V}/\mu\text{m}$ in average was applied across the device channel and the current flowing through the perovskite film was monitored and plotted as a function of time. The obtained results show the initial rapid increase in the current mainly due to the electrochemical doping induced in the semiconductor film followed by a slow exponential decay due to the electrochemical degradation of the perovskite (Figure 8b).

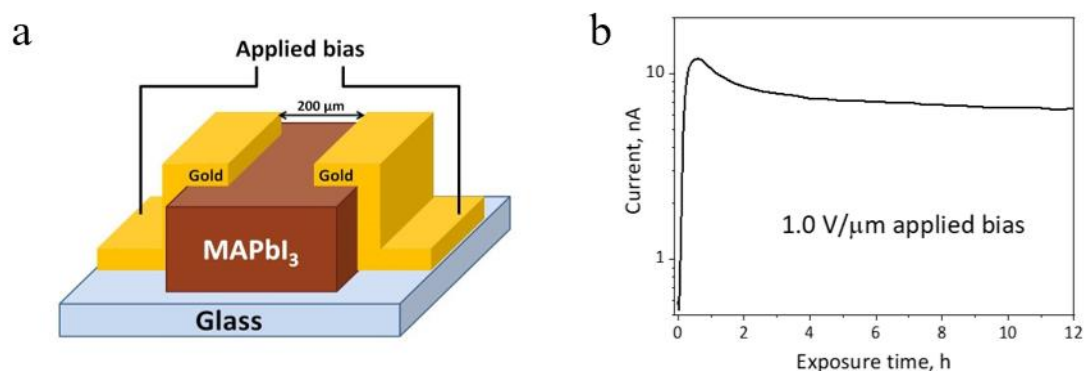


Figure 8. General layout of the lateral two-electrode device (a). Evolution of the current flowing through the channel of the lateral two-terminal device under potentiostatic polarization with $1\ \text{V}/\mu\text{m}$ applied bias (b).

A set of complementary analytical techniques was used to unravel the processes occurring in the material exposed to electric field. First, optical microscopy revealed severe changes in the film structure in a broad area ($\sim 50 \mu\text{m}$) adjacent to the cathode after a relatively long exposure to the electric bias for 340 h. On the contrary, the anode/perovskite interface was much more stable under the same conditions showing just a narrow ($2\text{-}5 \mu\text{m}$) stripe of degradation products (Figure 9a).

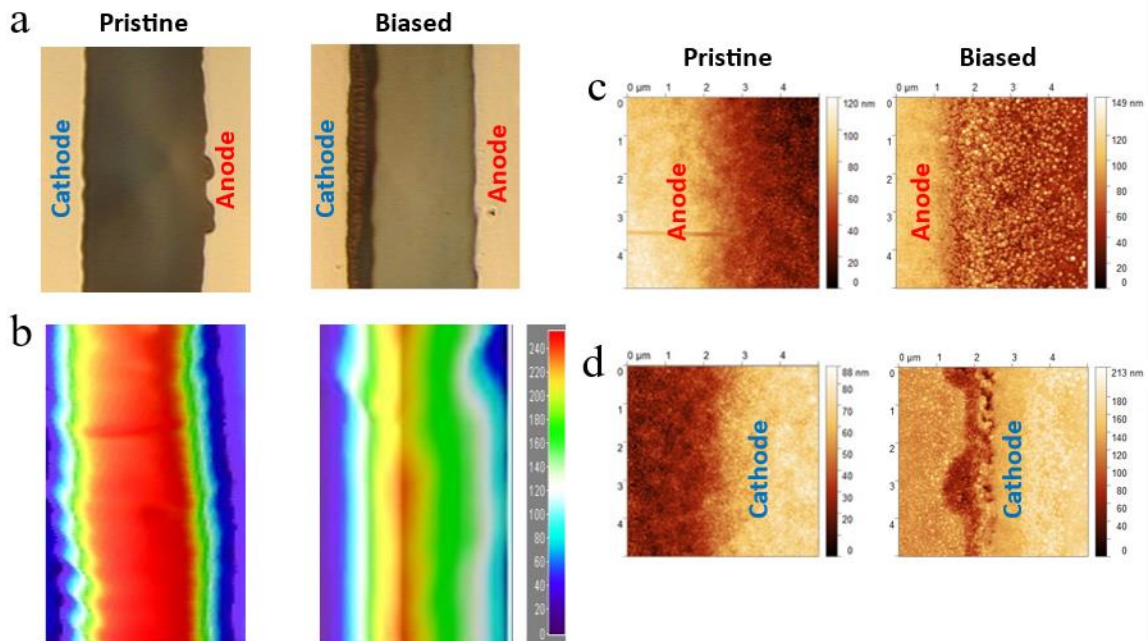


Figure 9. Optical microphotograph of the device channel before (left) and after (right) applying $1 \text{ V}/\mu\text{m}$ bias for 340 h (a). PL mapping of the channel before (left) and after (right) applying $1 \text{ V}/\mu\text{m}$ bias for 24 h (b). AFM for anode (c) and cathode (d) areas before (left) and after (right) applying $1 \text{ V}/\mu\text{m}$ bias for 100 h.

It is known that photoluminescence of the perovskite films is very sensitive to the appearance of defects.^{51,57-59,63,82} Therefore, we applied PL mapping to investigate the behavior of the material in the device channel after applying an electric field (Figure 9b). Indeed, biasing the device for 24 h leads to a significant quenching of the PL intensity at both electrodes with a stronger impact coming from the anode side. This observation is consistent with the results of a spectacular *in situ* PL imaging of ion motion in the perovskite films suggesting that I⁻ is rapidly moving toward anode in the applied electric field.^{51,58} The narrow stripe in the channel of the biased device showing the highest PL intensity in Figure 9b features the area where the perovskite undergoes a minimal degradation. On the contrary, quenching PL in the areas adjacent to both cathode and anode suggests a strong degradation with the formation of defects. At the anode side, I⁻ might undergo oxidation to molecular iodine (I₂) leading to the formation of iodide vacancies and, finally, PbI₂. At the cathode side, reduction of either Pb²⁺ or CH₃NH₃⁺ resulting in the corresponding vacancies can be suggested. Importantly, quenching of the PL from cathode and anode sides provides evidences that both anionic and cationic species are mobile in perovskite films, which is in agreement with previous theoretical and experimental studies.^{55,83} This conclusion is also supported by the fact that PL of the perovskite film becomes completely quenched in the channel after longer (> 50 h) exposure to electric bias.

Atomic force microscopy (AFM) data for devices exposed to external bias for 80 hours demonstrated the appearance of a new phase near the anode. The most striking morphological changes were induced by electric field at the cathode/perovskite interface,

where AFM revealed the formation of a deep (> 100 nm) canyon suggesting a severe degradation of the active material (Figure 9c,d). These results are consistent with the optical microscopy data also evidencing much stronger perovskite degradation at the cathode side rather than at the anode side.

To reveal the field-induced gradients in the chemical composition of the samples we used ToF-SIMS profiling. Figure 10a shows that applying electric bias for ~ 340 h does not change significantly the quantitative lead to iodine ratio across the channel of the device. This result is somewhat surprising since it is known that I⁻ anions are mobile and can undergo facile oxidation at the anode to form molecular iodine. However, it is known that I₂ readily reacts with virtually all iodides with the formation of polyiodides.^{84,85} For instance, I₂ can be trapped by MAI with the formation of MAI₃.

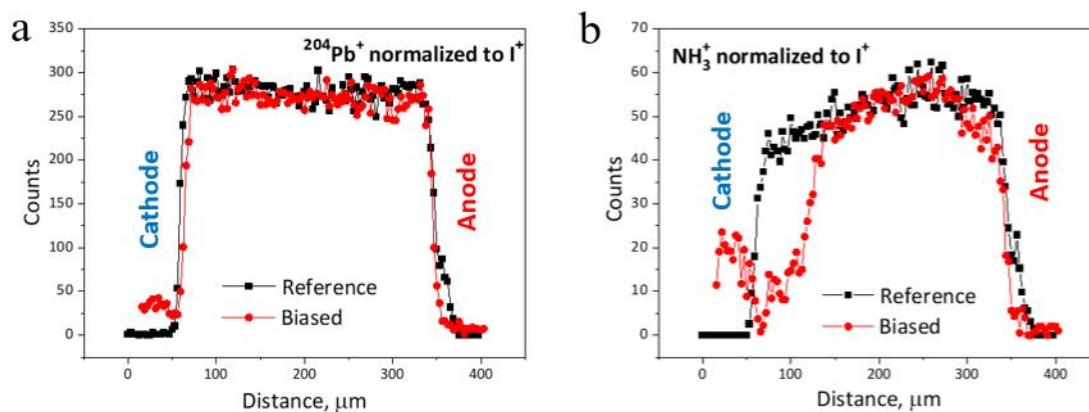


Figure 10. ToF-SIMS profiles of lateral two-terminal devices across the channel formed by MAPbI₃ semiconductor film before (reference) and after (biased) exposure to electric bias of 1 V/μm for 340 h. A ratio of ion yields is given to account for possible geometry effects: $^{204}\text{Pb}^+$ normalized to I^+ (a) and NH_3^+ normalized to I^+ (b).

This degradation pathway was also proposed in work of Frolova et al. and supported by the EDX data revealing iodine enrichment at the anode side of freshly biased two-terminal MAPbI₃ devices.⁴⁸ Therefore, it seems that though the oxidation of I⁻ occurs at the anode in the device under applied bias, it eventually does not change the elemental composition of the film due to trapping of I₂ in the form of polyiodides.^{86,87}

The most remarkable difference was observed in the yield of NH₃⁺ ion, which is a marker of methylammonium, normalized to the yield of I⁺ ion, which is the iodide marker. Figure 10b shows that applying electric bias (340 h) results in severe depletion of organic cations near the cathode thus implying that they undergo electrochemically induced degradation via reduction of CH₃NH₃⁺ to form methylamine CH₃NH₂ and molecular hydrogen H₂. Both products are volatile, so they can easily leave the film and make degradation process essentially irreversible. Obviously, massive elimination of organic cations changes the composition and structure of the perovskite film, which is consistent with the observations made using optical microscopy and AFM presented above.

5.1.2 Solar cell biasing and ToF-SIMS analysis

The experiments performed with the lateral two-terminal devices allowed us to reveal the important degradation pathway occurring in the perovskite films under applied electric bias, which includes reduction of organic cation and oxidation of iodine anion. However, it is not clear if this pathway is relevant to the real perovskite solar cell structures. Therefore, at the next stage of this work, we explored the bias-induced

degradation of perovskite solar cells assembled in a conventional p-i-n architecture shown in Figure 11a. Briefly, ITO was covered with poly(ethylene-3,4-dioxythiophene): polystyrene sulfonate (PEDOT:PSS) as a hole-selective layer, while phenyl-C₆₁-butyric acid methyl ester (PCBM) in combination with the Mg (20 nm)/Ag (180 nm) stack were used to provide electron-selective contact. A standard device fabrication procedure was reported previously.⁸⁸

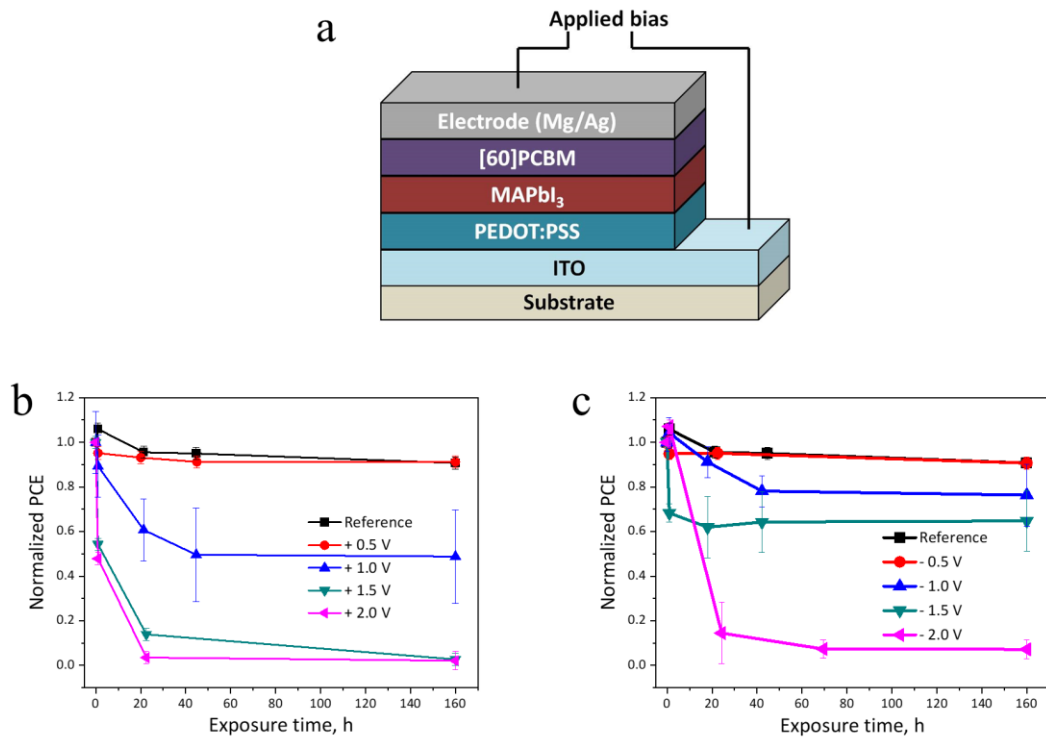


Figure 11. Schematic layout of the p-i-n perovskite solar cell architecture (a). The evolution of the device performance under different external biases applied in forward direction (b) and the comparison of the device degradation kinetics under forward and reverse bias of 1.5 V (c).

The selected batches of the fabricated devices were exposed to electric bias ranging from 0.1 V to 2.0 V applied either in the forward or reverse direction in the dark at room temperature inside the glove box under well-controlled anoxic conditions (O_2 , $H_2O < 0.1$ ppm). Biasing the devices at 0.1 to 0.5 V in both regimes did not induce any significant changes in the solar cells' performance. Some minor degradation was observed when the voltage was increased to 0.8 V, while the most severe effects appeared while bias approached 1 V, which is consistent with the previous observations of Bae et al. for n-i-p perovskite solar cells.⁴⁹

Figure 11b shows the evolution of the photovoltaic performance of the devices exposed to 0.5 V, 1.0 V, 1.5 V and 2.0 V in the forward bias, while a similar graph reflecting the device behavior under reverse bias is given in Figure 11c. Absolute values for devices' PCE, V_{OC} , J_{SC} and FF are demonstrated in Supplementary materials (Figures A2, A3 in Appendix A).

The decay of the device performance was found to be strongly bias-dependent. While the cells exposed to 1 V for 160 h can retain approximately one-half of the initial performance after 160 h, yet applying 2 V in forward bias significantly diminishes the device efficiency almost to zero within ~20 h. It should be noted that a decrease in the short circuit current density and fill factor makes the strongest contribution to the diminishment in performance; while the open circuit voltage is less affected (Figures A2, A3 in Appendix A, Supplementary materials). The observed bias dependent aging effects confirm that the device failure occurs due to some electrochemical (field-induced) processes in the device structure rather than because of some other suggested degradation

pathways like film defects, e.g. particles or pinholes leading to the development of shunts.

This conclusion is also supported by the evolution of the device J - V characteristics, which show an increase in the hysteresis for longer bias exposure times regardless the used voltage sweeping rate (10 mV/s or 100 mV/s, Figure 12). This result suggests that the hysteresis appearing in the current-voltage characteristics of perovskite solar cells might have an electrochemical origin and can be directly related to reversible redox transitions in the absorber layers adjacent to the electrodes.

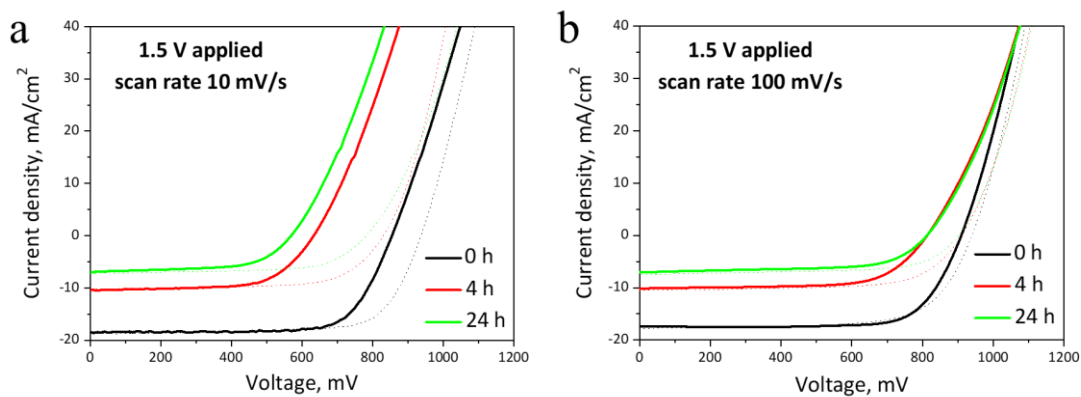


Figure 12. Evolution of forward (solid lines) and reverse (dot lines) J - V curves at scan rates of 10 mV/s (a) and 100 mV/s (b) for device biased at the applied potential of 1.5 V in forward direction.

It is also notable that applying a forward bias in all cases induces a stronger decay in the device performance compared to the reverse bias as shown in Figure 11c. This effect can be understood considering the fact that PEDOT:PSS is a hole-selective layer and it is blocking to some extent the injection of electrons into the perovskite active

layer from ITO under reverse bias. At the same time, PCBM is a typical n-type semiconductor essentially blocking injection of holes from the top electrode under reverse bias. Therefore, a careful selection of charge selective interlayers with the advanced blocking properties with respect to the opposite type of carriers might improve significantly the stability of the perovskite solar cells under reverse bias. This is practically very important aspect since some of the solar elements in a panel experience reverse bias effect in case of partial shadowing of the module.⁶²

Importantly, the performed experiments revealed a rather fast device degradation under forward bias of 1.0 V, which is below the typical open circuit voltage values of optimized perovskite solar cells (~1.1 V). Therefore, the impact of the electric field has to be considered while analyzing the intrinsic pathways responsible for the degradation of perovskite solar cells under realistic operation conditions. To gain a deeper understanding of the mechanistic aspects of the observed field-induced degradation of the perovskite solar cells, we performed ToF-SIMS analysis of non-biased reference cells and the devices exposed to 2 V for 160 h under forward bias. Figure 13 shows the chemical maps reflecting the distribution of the characteristic marker ions such as Pb^+ , I_2^- and CH_3NH_3^+ in the biased devices and the reference cells stored in the dark for the same time. Bias might be inducing some minor redistribution of lead as can be concluded from the appearance of trace amounts of Pb^+ inside PEDOT:PSS and PCBM charge transport layers, while this effect can still be considered as negligible.

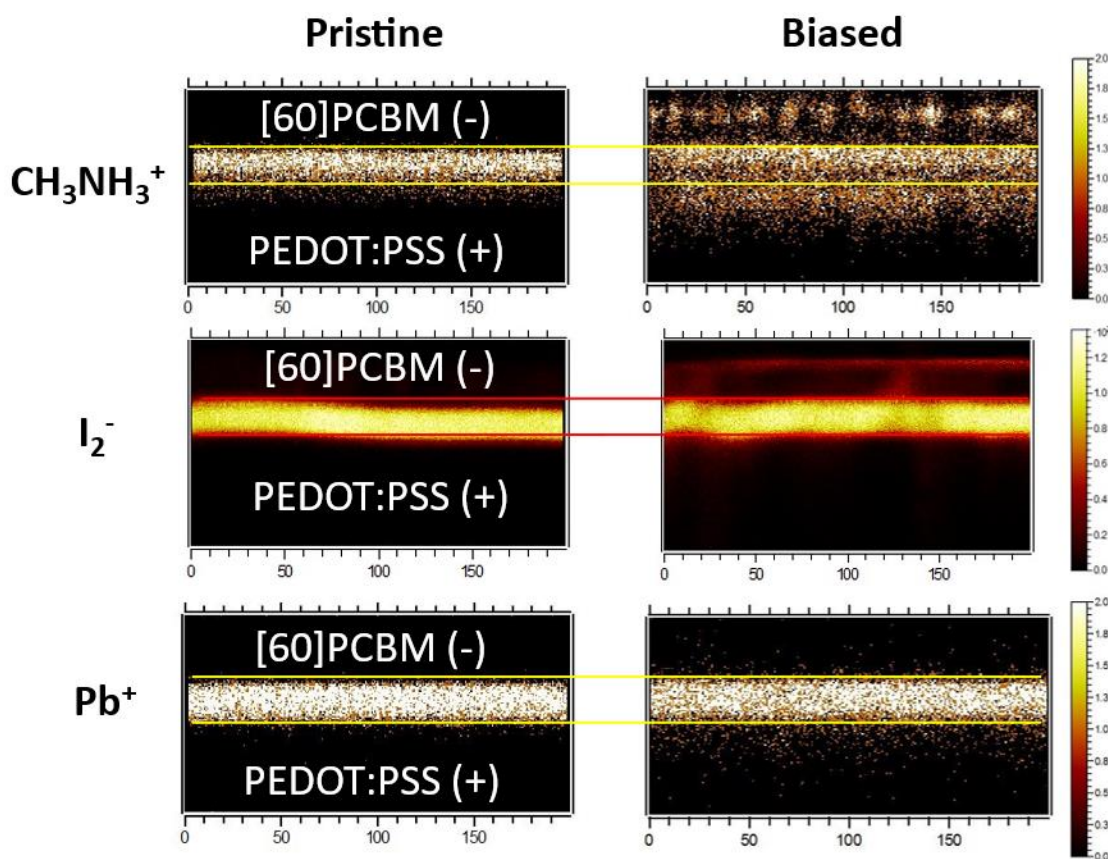


Figure 13. ToF-SIMS chemical maps showing the distribution of the characteristic marker ions Pb^+ , I_2^- and CH_3NH_3^+ in the reference cells and devices exposed to 2 V under forward bias for 160 h.

Field-induced redistribution of iodine was much stronger: even though its diffusion into PEDOT:PSS was limited, a considerable amount of iodine was observed in the PCBM electron transport layer and, particularly, at the top electrode/PCBM interface suggesting the formation of metal iodides. This result is not surprising since it is known that fullerene C_{60} aggressively absorbs iodine and forms a non-covalent inclusion complex $\text{C}_{60}\cdot 2\text{I}_2$.^{89,90} Moreover, the corrosion of the top electrode by iodine was observed

many times by other research groups previously.⁹¹⁻⁹⁵ To summarize, the presented maps showing iodide distribution before and after bias treatment of the device evidence anodic oxidation of I^- to I_2 , which was discussed above.

The most severe changes were revealed at the maps of $CH_3NH_3^+$ ions evidencing a massive degradation of the perovskite and accumulation of organic cations within both PCBM and PEDOT:PSS layers. Such result might be surprising since field-induced ion migration can explain only the appearance of $CH_3NH_3^+$ inside the fullerene-based electron transport layer. We showed previously that fullerene derivatives, in particularly PCBM, tend to accumulate methylammonium iodide released from the perovskite under illumination.⁹⁰

Therefore, a facile penetration of $CH_3NH_3^+$ into the PCBM layer and its transport all the way until it reaches the metal electrode is quite expectable. The reduction of $CH_3NH_3^+$ produces methylamine and molecular hydrogen as discussed above. In contrast to the lateral devices, methylamine cannot easily escape from the p-i-n solar cell structure e.g. due to the encapsulation effect of the top metal electrode. Therefore, it is continuously produced and accumulated in the device during exposure to the electric bias. The back migration of methylamine through the perovskite layer (e.g. at the grain boundaries) to the PEDOT:PSS hole selective layer leads to dedoping of PEDOT (since methylamine is much stronger base than polythiophene) and the formation of methylammonium salt of polystyrene sulfonic acid. Therefore, the well-known acidic nature of PEDOT:PSS is responsible for the aggressive absorption of methylamine and accumulation in the form of the corresponding PSS salt with the $CH_3NH_3^+$ cations.⁹⁵

Thus, the presented maps showing the CH_3NH_3^+ redistribution due to the action of the electric field evidence a strong impact of the reduction of organic cations and liberation of methylamine. These results are fully consistent with the data obtained for lateral two-terminal devices discussed above. Moreover, we performed cyclic voltammetry measurements for MAPbI_3 precursor solution in DMF and revealed both the oxidation and reduction processes set ~ 0.9 V apart from each other (Figure 14). Surprisingly, the solution electrochemistry “stability window” revealed for MAPbI_3 precursor also matches the behavior of perovskite solar cells, which start to degrade when applied bias approaches 1V.

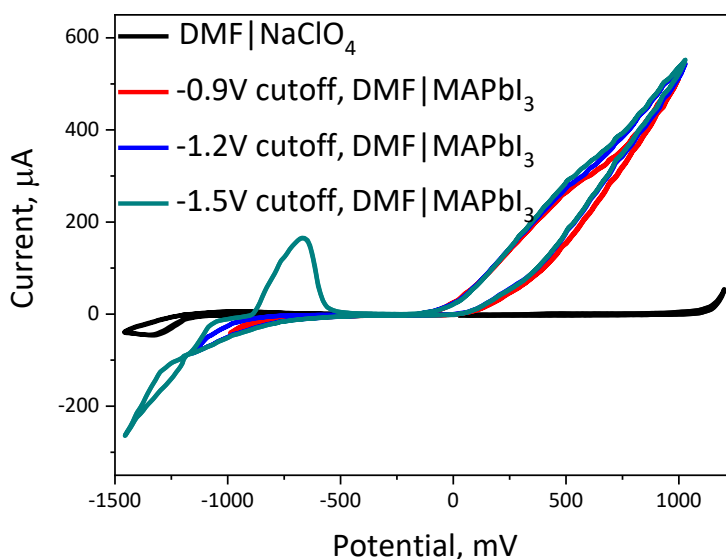


Figure 14. Cyclic voltammograms for 0.1 M solution of NaClO_4 in DMF as illustration of the DMF electrochemical stability window (from -1200 mV to 1100 mV) and 0.01 M solution of MAPbI_3 in DMF measured with various cathodic potential cutoffs.

5.1.3 Mechanism determination

The presented experimental results evidence unambiguously that MAPbI₃ films undergo facile field-induced electrochemical degradation following the mechanism presented in Figure 15. The oxidation of I⁻ with formation of I₂ seems to be potentially reversible due to trapping of iodine in the film in the form of polyiodides (AI_{n+2} on the scheme) incorporating univalent I₃⁻ anions. In contrast, reduction of CH₃NH₃⁺ to CH₃NH₂ and H₂ is essentially irreversible because both products are volatile and easily leave the device architecture (in particular, molecular hydrogen). It should be emphasized that similar electrochemical processes can occur in operating perovskite solar cells and even thin films exposed to light illumination. Indeed, the built-in and light induced potentials are more than sufficient to trigger the aforementioned redox processes, thus ruining the stability of the absorber material and devices. Most likely this is the main aspect why the all-inorganic perovskites such as CsPbX₃ (X = I, Br) incorporating cesium cations demonstrate outstanding stability in thin films and solar cells, as Cs⁺ can hardly be reduced under the specified conditions.⁹⁶⁻⁹⁸

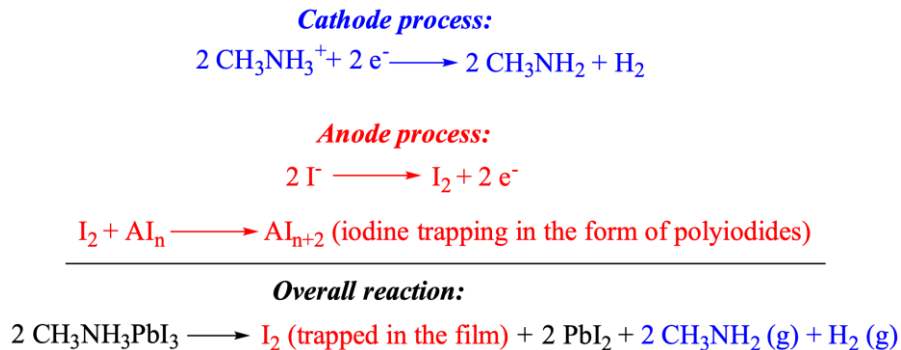


Figure 15. Schematic representation of the revealed mechanism of the field-induced electrochemical decomposition of MAPbI₃.

The confirmation that the electrochemical degradation of MAPbI_3 occurs under the bias even below the open circuit voltage of optimized perovskite solar cells is essentially important from a practical point of view. It is well known that perovskite solar cells are much less stable under the open circuit (OC) rather than at maximal power point (MPP) conditions.

Indeed, the results revealed here on the electrochemical degradation pathways imply they considerably contribute to the perovskite degradation at V_{OC} , while their impact at MPP is minimized since the MPP voltage is usually significantly below V_{OC} . Presumably, designing low band gap metal halide perovskites can partially solve the problem of the electrochemical degradation of the perovskite-type absorber materials.^{99,100} The open circuit voltage of such cells will be reduced giving a hope for better electrochemical stability, while the current density is expected to be increased following the band gap decrease thus providing a comparable or even higher power conversion efficiency.

5.1.4 Conclusion for the first stage

We performed a systematic study of the electric field-induced degradation of $\text{CH}_3\text{NH}_3\text{PbI}_3$ thin films in lateral two-terminal devices and p-i-n perovskite solar cell configurations. A set of complementary microscopy techniques revealed that perovskite undergoes electrochemical redox processes at both cathode and anode sides thus implying that both cations and anions migrate in the perovskite films. The oxidation of I⁻ to I₂ does not lead to severe compositional changes probably due to trapping of molecular

iodine in the form of polyiodides as was reported previously. The formation of such polyiodides under different conditions is also well documented for lead halide perovskites.^{87,101} Therefore, iodide to iodine (triiodide) oxidation can be reversible and does not represent the main limitation for the perovskite stability.⁸⁶ Of course, the formation of polyiodides is not the only possible degradation process. Formation of volatile iodine vapor which leaves the perovskite film and even can react with gold electrodes should also be considered under applied electric field. And in solar cells this molecular iodine can react with other components of the device, for example fullerene derivatives of even the backside of top silver electrodes.

But the actual paradigm changing discovery is in revealing a facile reduction of organic cations with the formation of volatile products such as methylamine and molecular hydrogen. There is also a possibility of other products formation which were unable to detect with ToF-SIMS. But nevertheless, while the iodine could be trapped within the device, the latter is too mobile to be captured in the reaction zone e.g. by adjacent layers. Therefore, the reduction of organic cations should be considered as the most important and virtually irreversible electrochemical process affecting severely the stability of the perovskite films. The fact that electrochemical degradation occurs at potentials below the solar cell open circuit voltages implies a great challenge for achieving a long-term operational stability of hybrid perovskite photovoltaics, which needs to be addressed in the future e.g. via rational interface engineering. The revealed here mechanistic aspects of the electric field-induced MAPbI₃ degradation provide

impetus for the rational design of new absorber materials with improved efficiency and stability for perovskite photovoltaic solar cells.

5.2 Defining the most electrochemically stable perovskite material depending on chemical structure

5.2.1 Bulk material biasing and comparison

On the next stage our goal was to determine the most electrochemically stable complex lead halide and investigate the influence of chemical structure on electrochemical stability of bulk material. For the preliminary checking we created a full set of lateral devices with the same architecture as was described in chapter 5.1.1 (Figure 8a). Gold electrodes were evaporated directly on top of the perovskite thin film through the shadow mask, leaving only the narrow channel of 200 μm of perovskite material between gold electrodes. Lateral devices were produced for a set of perovskite materials with various structure: MAPbI_3 , $\text{MA}_{0.15}\text{Cs}_{0.1}\text{FA}_{0.75}\text{PbI}_3$, $\text{Cs}_{0.15}\text{FA}_{0.85}\text{PbI}_3$, $\text{Cs}_{0.125}\text{FA}_{0.875}\text{PbBr}_{0.375}\text{I}_{2.625}$, CsPbI_2Br . All materials were prepared according to the literature sources mentioned in Experimental section of current Thesis and their correspondence to the literature was confirmed by XRD analysis. Of course, chemical formulas written here do not represent exact composition of each material, but correspond to the initial ratios of precursors in prepared solutions. There is undoubtedly a deviation of real compositions from the formulas, but according to the literature sources it won't be significant enough to disrupt our comparative analysis.

Figure 16 demonstrates the starting time for changes in current as a function of the sample biasing time at the voltage density $1 \text{ V}/\mu\text{m}$ applied to the lateral device electrodes. It can be seen from the presented data that all materials without exception display the same behavior as was previously shown for MAPbI_3 in chapter 5.1.1. Process starts with rapid increase in the current, reaches its limit at the different for every material time and current and then slowly goes through exponential decay (dot lines) due to the electrochemical degradation of the material.

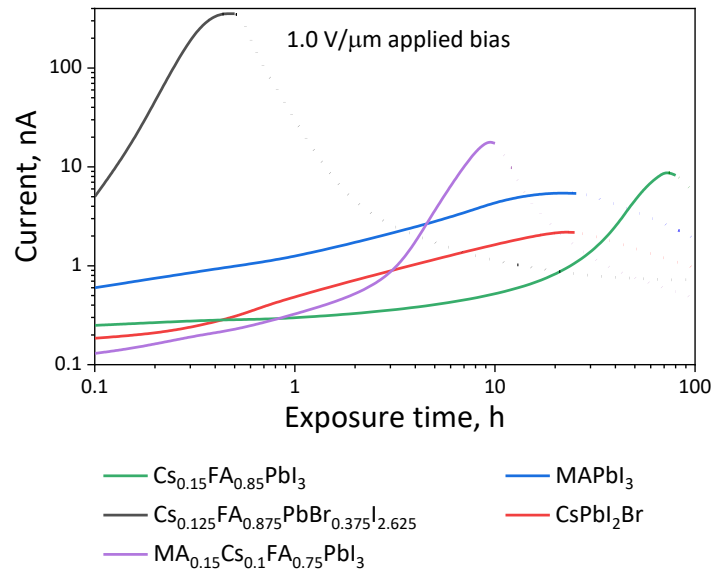


Figure 16. Evolution of the current flowing through the channel of the lateral two-terminal device under potentiostatic polarization with $1 \text{ V}/\mu\text{m}$ applied bias for various perovskite materials.

The electrochemical doping is most likely due to the accumulation of charge carriers or defects in the material, how it was already described previously.⁴⁸ This improves the conductivity in the channel at first stage. However, after reaching the limit concentration the material starts to degrade and the current decreases. And concentration of accumulated charge carriers or defects can be roughly estimated. According to the definition we can write the current-time dependence as:

$$I(t) = dq/dt,$$

Where I is the current flowing through the channel, t is time and q is a charge accumulated in a channel through biasing. From this point, area below the $I(t)$ curve would correspond to the accumulated charge in the channel. We can evaluate the stability of materials by integrating their $I(t)$ from 0 to the maximum current point for every material, which will correspond to the maximum accumulated charge Q that material could sustain. So according to the data from the Figure 16 we can preliminarily rate stability of investigated materials as $\text{Cs}_{0.15}\text{FA}_{0.85}\text{PbI}_3$ (area = 305) > MAPbI_3 (area = 105) > $\text{Cs}_{0.125}\text{FA}_{0.875}\text{PbBr}_{0.375}\text{I}_{2.625}$ (area = 90) > $\text{MA}_{0.15}\text{Cs}_{0.1}\text{FA}_{0.75}\text{PbI}_3$ (area = 74) > CsPbI_2Br (area = 40).

The same set of techniques as for MAPbI_3 was used to understand the difference in the processes in different materials. We applied PL mapping to materials $\text{Cs}_{0.15}\text{FA}_{0.85}\text{PbI}_3$, $\text{MA}_{0.15}\text{Cs}_{0.1}\text{FA}_{0.75}\text{PbI}_3$, MAPbI_3 and $\text{Cs}_{0.125}\text{FA}_{0.875}\text{PbBr}_{0.375}\text{I}_{2.625}$. Unfortunately, we were not able to perform PL mapping for CsPbI_2Br because this material could not sustain the transportation between the glovebox and measurement device. Even encapsulated lateral devices immediately degraded after getting into

ambient atmosphere, starting from edges of the film. Behavior of the materials in the device channel after applying an electric field and also optical photographs made right after the last PL mapping are demonstrated in Figure 17.

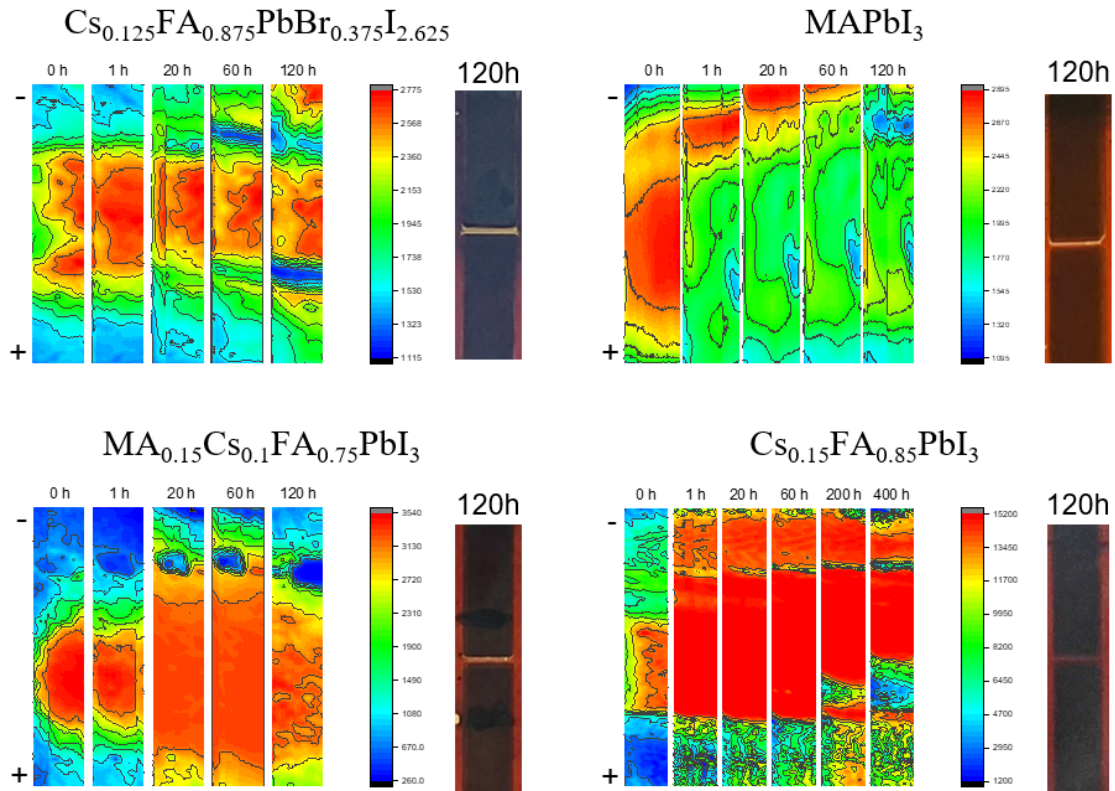


Figure 17. Evolution of PL signal in the channel of lateral two-electrode device during the electric bias exposure for various perovskite materials. Optical photos of corresponding channels for every material after the 120 h biasing are presented on the left. Channels on all figures oriented horizontally, with cathode on top position and anode in bottom position.

Optical photographs of biased channels revealed severe changes in the film structure in an area adjacent to the cathode after a relatively long exposure to the electric bias for 120 h for all materials except $\text{Cs}_{0.15}\text{FA}_{0.85}\text{PbI}_3$. The anode side was much more stable for $\text{MA}_{0.15}\text{Cs}_{0.1}\text{FA}_{0.75}\text{PbI}_3$ and MAPbI_3 , while $\text{Cs}_{0.125}\text{FA}_{0.875}\text{PbBr}_{0.375}\text{I}_{2.625}$ demonstrates degradation at both sides of the channel.

PL mapping demonstrates increasing of perovskite material PL signal in the channel for $\text{Cs}_{0.15}\text{FA}_{0.85}\text{PbI}_3$, $\text{MA}_{0.15}\text{Cs}_{0.1}\text{FA}_{0.75}\text{PbI}_3$ and $\text{Cs}_{0.125}\text{FA}_{0.875}\text{PbBr}_{0.375}\text{I}_{2.625}$, after 1 h bias applying, which correlates with chronoamperometry data and represents the increase in material conductivity. Then quenching of the PL intensity at cathode side is observed starting from 20 h of biasing. But MAPbI_3 demonstrates a more rapid degradation process with a decrease in the PL intensity along the whole channel even at the 1-st hour. So, this confirms that the degradation process we defined earlier, with the reduction of organic cation at the cathode and following release of volatile products, is applicable to all hybrid perovskites.

We used ToF-SIMS profiling to reveal the field-induced gradients for all 5 materials. Figures 18 and 19 show that applying electric bias for ~ 300 h always leads to the severe depletion of organic cations near the cathode normalized to the yield of Pb^+ cation. Pb^+ was chosen as normalization cation because among all components of perovskite it is the least mobile one. Despite the fact that obtained data is quite difficult for the separated analysis, especially in cases of multicomponent materials, we still can observe general tendencies like the common for everyone electrochemical reduction of not only highly volatile MA^+ cation (Figure 18-1a,b), but also for FA^+ (Figure 18-1b,c,

Figure 18-2a) in all presented cases. Even big and heavy Cs^+ cations migrate from anode to the cathode (Figure 18-1b,c, Figure 18-2a,b), leading to the chemical shift in all perovskite material.

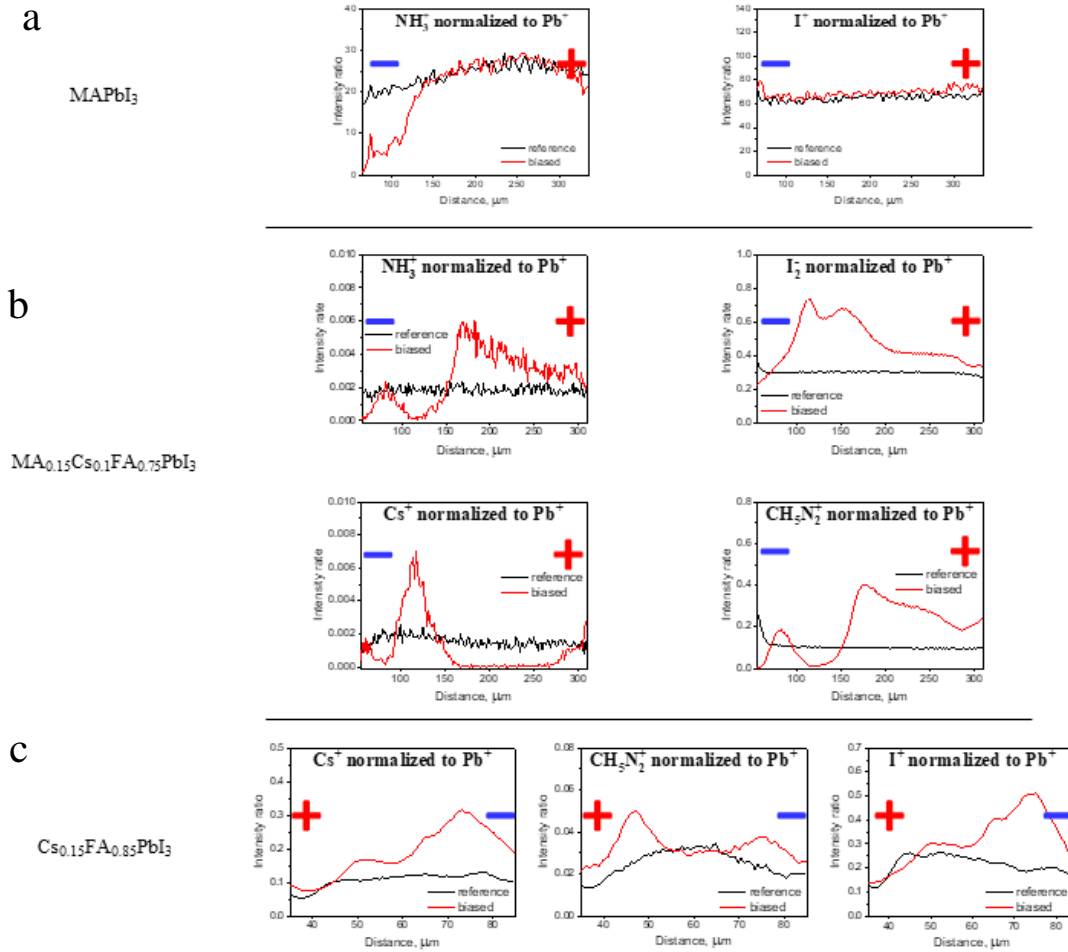


Figure 18-1. ToF-SIMS profiles of lateral two-terminal devices for across the channel formed by corresponding (noted on the left) perovskite semiconductor film MAPbI_3 (a)

$\text{MA}_{0.15}\text{Cs}_{0.1}\text{FA}_{0.75}\text{PbI}_3$ (b) $\text{Cs}_{0.15}\text{FA}_{0.85}\text{PbI}_3$ (c) before (reference) and after (biased) exposure to electric bias of $1 \text{ V}/\mu\text{m}$ for 300 h. A ratio of ion yields is given to account

for possible geometry effects.

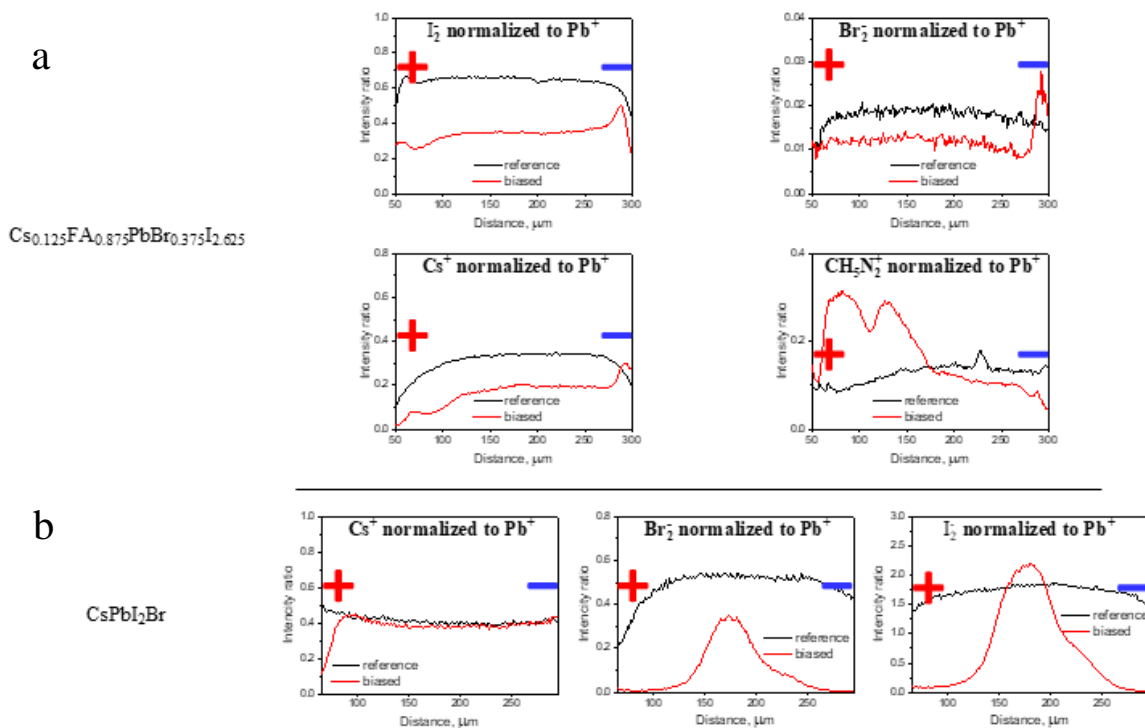


Figure 18-2. ToF-SIMS profiles of lateral two-terminal devices for across the channel formed by corresponding (noted on the left) perovskite semiconductor film $\text{Cs}_{0.125}\text{FA}_{0.875}\text{PbBr}_{0.375}\text{I}_{2.625}$ (a) CsPbI_2Br (b) before (reference) and after (biased) exposure to electric bias of $1 \text{ V}/\mu\text{m}$ for 300 h. A ratio of ion yields is given to account for possible geometry effects.

All materials were finally characterized by changes in topography according to AFM (Figure 19). Since $\text{Cs}_{0.15}\text{FA}_{0.85}\text{PbI}_3$ demonstrated the best bulk material stability so far, we also decided to additionally test its close structural modifications $\text{Cs}_{0.12}\text{FA}_{0.8}\text{PbI}_{2.92}$ and $\text{Rb}_{0.1}\text{Cs}_{0.15}\text{FA}_{0.75}\text{PbI}_3$. It was demonstrated by our colleagues recently that solar cells based on $\text{Cs}_{0.12}\text{FA}_{0.8}\text{PbI}_{2.92}$ demonstrate enhanced stability, since excess of PbI_2 shifts the equilibrium of the perovskite material and its degradation

products to the perovskite side. And partial replacement of FA^+ with Rb^+ in $\text{Rb}_{0.1}\text{Cs}_{0.15}\text{FA}_{0.75}\text{PbI}_3$ was recently demonstrated as the way to create highly stable and efficient MA^+ free perovskite solar cells.⁹⁰ It was shown that all the studied materials undergo degradation in the zones adjacent to the electrodes. Figure 19 shows the most severe changes in MAPbI_3 , including formation of deep canyon alongside the cathode. Similar effect could be observed for all hybrid materials containing organic components, but of different level. Formation of new particles is also visible for all materials but the most excessively for $\text{Cs}_{0.15}\text{FA}_{0.85}\text{PbI}_3$. During all previous experiments $\text{Cs}_{0.15}\text{FA}_{0.85}\text{PbI}_3$ was the stability leader among all perovskite materials. Only its relatives $\text{Cs}_{0.12}\text{FA}_{0.8}\text{PbI}_{2.92}$ and $\text{Rb}_{0.1}\text{Cs}_{0.15}\text{FA}_{0.75}\text{PbI}_3$ with similar chemical structure could probably overthrow it according to the AFM data. Another candidate for long-living devices could be the fully inorganic CsPbI_2Br which does not contain any organic components prone to reduction process, but during the previous experiments it demonstrated comparatively low stability.

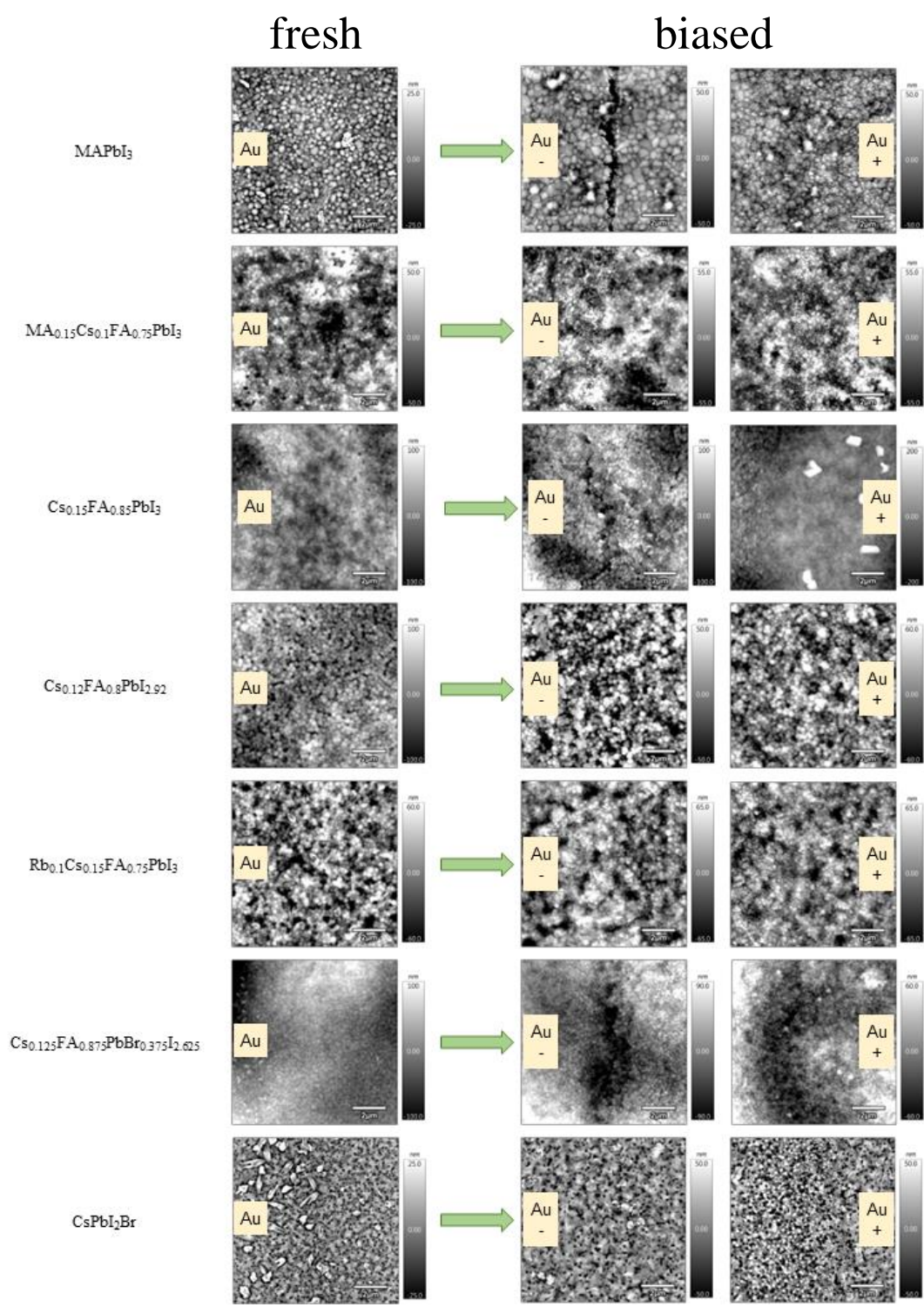


Figure 19. AFM data for corresponding (marked on the left) perovskite materials before and after biasing for 80 hours near both electrodes.

5.2.2 Solar cells testing

The n-i-p solar cells were fabricated in a configuration of ITO/SnO₂/PCBA/perovskite/PTAA/V₂O₅/Al as shown in Figure 20a. The perovskites with various compositions (MAPbI₃, MA_{0.15}Cs_{0.1}FA_{0.75}PbI₃, Cs_{0.15}FA_{0.85}PbI₃, Cs_{0.12}FA_{0.8}PbI_{2.92}, Rb_{0.1}Cs_{0.15}FA_{0.75}PbI₃, Cs_{0.125}FA_{0.875}PbBr_{0.375}I_{2.625}, CsPbI₂Br and MAPbI_xCl_{3-x}) in the n-i-p structure were investigated for their lifetimes. In this experiment the device configuration different from the previously used was chosen because of the difficulties in optimizing the manufacturing process of solar cells with various active layers. Out of all tested device architectures only mentioned here allowed us to make devices with all desired perovskite materials of sufficient quality and starting efficiency. Figure 20b represents the evolution of normalized average PCE for obtained cells, each material was represented by the batch of minimum 3 devices, devices were biased at constant voltage 1V. Absolute values for all solar cell parameters (V_{OC} , J_{SC} , FF and PCE) and their evolution during the bias exposure is presented in Supplementary materials (Figure A4 in Appendix A).

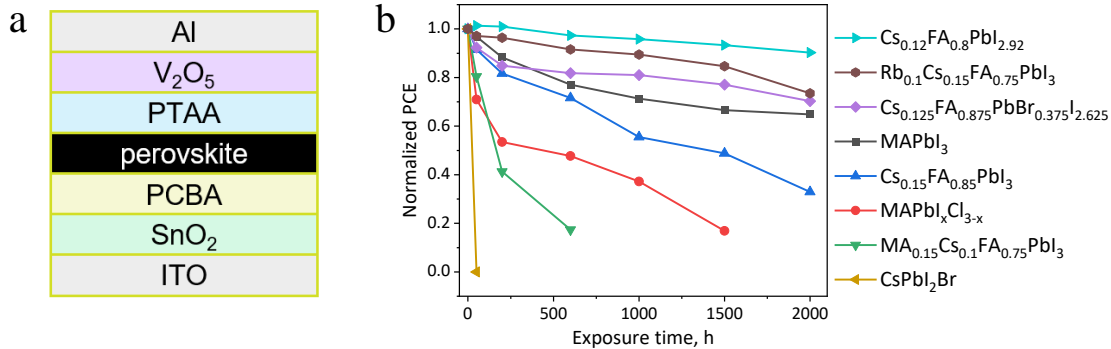


Figure 20. N-i-p solar cells device configuration (a). Normalized average PCE evolution for the batches of solar cells with different perovskite photoactive layers (b).

The obtained data correlates well with the chronoamperometry measurements from Figure 16. And inorganic perovskite CsPbI₂Br devices demonstrated the fastest degradation among all materials, despite their favorable chemical structure. The poor performance of this material during first tests in lateral devices here was supported by the low thickness of the photoactive film, which is unfortunately around 200 nm for CsPbI₂Br because of its processing method, while for other materials thickness is around 400 nm. Thickness influences the voltage density per 1 nm in the biasing process, so it is obvious that thin film devices will surely degrade faster.

Fortunately, thickness of all hybrid materials films was around 400 nm and thus we are able to compare them. And on top of the rating, we can see two materials with the best AFM profiles Cs_{0.12}FA_{0.8}PbI_{2.92} and Rb_{0.1}Cs_{0.15}FA_{0.75}PbI₃. Unfortunately, their analog Cs_{0.15}FA_{0.85}PbI₃ was not able to demonstrate significant stability. But it can be noted that absence of MA⁺, presence of inorganic cations like Cs⁺ or Rb⁺ does

significantly improves stability of the device and material itself. Also, the excess of PbI_2 in the chemical composition also appears to have positive effect on device stability, as it probably shifts the equilibrium of the reaction towards the original components.

5.2.3 Conclusion for the second stage

Based on the results for the second stage of this work, we can conclude that the chemical composition of perovskite material influences its stability in bulk, but it does not always correlate with a complete solar cell stability. Of course, replacement of a highly volatile MA^+ with the bigger cation FA^+ or inorganic Cs^+ and Rb^+ improves stability of the device, but the thickness of the photoactive material in the device should also be as high as possible. At the same time, replacement of I^- with Br^- seems to have insignificant effect on device stability.

5.3 Device configuration influence on electrochemical stability of the PSCs

5.3.1 Influence of hole-transport layers on electrochemical stability of the device

PSCs for all experiments at this stage were assembled in a conventional p-i-n configuration because this structure permits the largest variability in used HTMs. It also helps to avoid large J - V curve hysteresis, which we consider as a significant factor since large hysteresis exhibits presence of additional polarization effects able to affect the experiment.^{39,40} Structure of the device is demonstrated in Figure 21a.

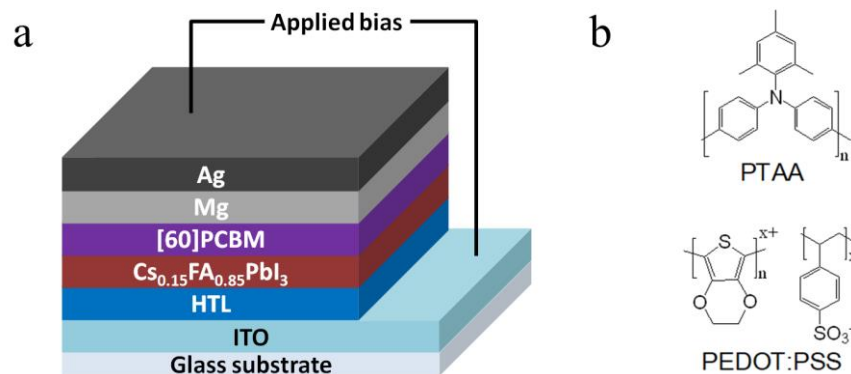


Figure 21. Schematic structure of solar cells used in experiments (a). Chemical structures of organic HTMs (b).

ITO was covered with the corresponding hole-transport material or with the specific sequence of materials. Stoichiometric $\text{Cs}_{0.15}\text{FA}_{0.85}\text{PbI}_3$ was selected as a photoactive layer because it was defined in the previous stage as a highly effective material with relatively high stability.^{102,103} PCBM in combination with the Mg was used to provide electron transport and Ag contacts were evaporated on top through the shadow mask.

For the experiment, we selected the set of well-known HTMs of different nature. PTAA was reported as an outstanding polymer for improving the perovskite films and PSCs photostability.¹⁰⁴⁻¹⁰⁸ PEDOT:PSS is a long-known hole-transport materials for p-i-n device architectures with promising PCE.¹⁰⁶ Structures of these organic HTMs are presented in Figure 21b. We also applied inorganic HTMs such as NiO_x and CuO_x , CuI and CuSCN. All of them exhibit suitable valence band positions, wide bandgap and high transparency, resulting in favorable characteristics and stability of the PSCs.¹⁰⁹⁻¹¹³

At the first stage, selected batches of the devices (at least 3 samples for every investigated HTL) were exposed to the electric bias in forward direction in a “stepwise” mode: starting voltage was set as 0.7 V and then it was increased every 50 hours by 0.1 V up to 1 V, then the voltage was increased every 50 hours by 0.2 V up to 2.2 V. This method simultaneously allows to accelerate the degradation process for obtaining results in short period of time and demonstrates the influence of voltage magnitude. The experiment was performed in the dark, at room temperature inside the glovebox with controlled atmosphere (O_2 , $H_2O < 0.1$ ppm). Characteristics of all devices were measured every 25 hours, average magnitude was counted and normalized to the starting point.

Applying bias from 0.7 to 0.9 V did not induce any changes in the device performance regardless the hole-selective material. The evolution of average normalized device PCE starting from 0.9 V is demonstrated in Figure 22a. Systems with such HTLs as CuI, CuSCN and PEDOT:PSS demonstrated significant PCE decreasing started from 0.9 V biasing voltage. The NiO_x -based system demonstrates relative stability at voltages below 1 V, but immediately goes almost to zero efficiency at 1.2-1.4 V applied bias. Devices with PTAA appeared to be the most stable during this experiment: they have demonstrated improvement of PCE for 10% at biasing voltages equal or less than 1 V.

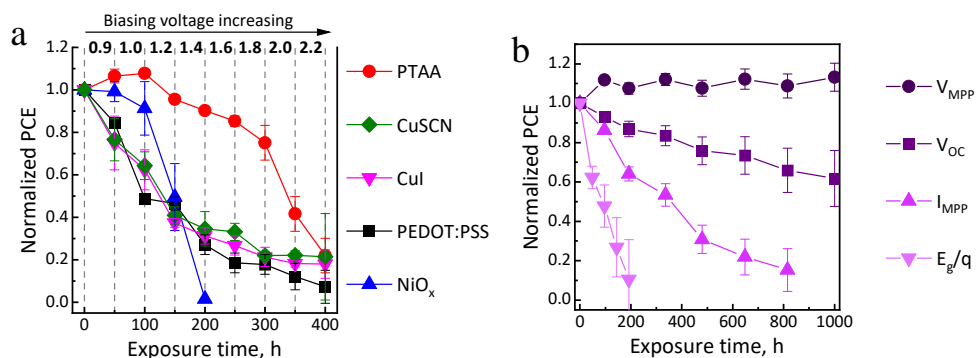


Figure 22. Evolution of normalized PCE during the “stepwise” biasing of solar cells with various HTLs (a). Evolution of the efficiency of PSCs with PTAA as HTL under applied electric bias ($V_{MPP} = 0.7$ V, $V_{OC} = 1$ V, $I_{MPP} = 18.3$ mA/cm², $E_g/q = 1.55$ V) (b).

It is notable, that dramatic change of the efficiency starts at particular biasing voltage for every system reproducibly. The appearance of the so-called “threshold voltage” for PSCs was already observed previously in the publication of the Bae et al. and confirmed in previous part of the Thesis. That means, in the current situation we can claim that the threshold voltage depends on the incorporated charge-transport materials, which makes it even more important to understand the influence of HTM nature on PSC electrochemical stability.

Speculatively, the magnitude of this “threshold voltage” should be related to the V_{OC} or V_{MPP} of the solar cell. To check this assumption, we calculated the average V_{OC} and V_{MPP} for every batch of samples before biasing. The following values were estimated: for PTAA solar cells average $V_{OC} = 1020$ mV and $V_{MPP} = 900$ mV, for NiO_x – 910 mV and 730 mV, for CuSCN – 770 mV and 620 mV, for CuI – 790 mV and 610 mV, for PEDOT:PSS – 800 mV and 750 mV respectively. Additionally, it is noticeable

that for all configurations PCE decreasing starts right after biasing voltage reaches/overcomes the V_{OC} of the device. In view of the voltage magnitude effect, we faced the necessity to choose the best value applicable for further investigation of different systems electrochemical degradation rate. Our previous experiment was accelerated and so the result cannot be applied for comparison of the PSCs long-term degradation.

On the second stage, ITO/PTAA/ $CS_{0.15}FA_{0.85}PbI_3/PC_{60}BM/Mg/Ag$ configuration was chosen as the reference system for checking the influence of biasing voltage on the PSC stability and additionally choosing the right biasing voltage for further experiments. This system is the most stable at voltages less than 2 V so it was necessary to find the right voltage when PTAA solar cells do not degrade just in few hundreds of hours. We decided to divide PTAA solar cell samples to 4 batches (at least 6 samples in each batch) and apply 4 different biases: $V_1 - 0.7$ V is less or equal to the initial V_{MPP} of the solar cells, $V_2 - 1$ V is equal to average V_{OC} of the solar cells, $V_3 - 1.2$ V is equal to V at I_{MPP} in the dark and $V_4 - 1.55$ V is equal to E_g/q . These parameters were chosen according to the recommendations of the consensus paper dedicated to the PSCs stability protocols.¹¹⁴

In Figure 22b, the evolution of normalized PCE for all four applied biases is demonstrated. The reproducible 10 % increasing of device performance at V_{MPP} biasing is observed. V_{OC} biasing induces constant uniform decrease and loss of 40 % of efficiency after 1000 h of aging. I_{MPP} and E_g/q biasing leads to total degradation of all devices in 800 h and 200 h accordingly. As expected, higher biasing voltage induces faster degradation of device performance. This data also positively correlates with recent

works implying the faster photo- and bias-induced degradation under OC conditions versus the MPP.¹¹⁵⁻¹¹⁷ We assume that underlying mechanism can be related to the charge-carriers accumulation,¹¹⁸⁻¹²⁰ which at small times and/or voltages leads to the electrochemical doping of the semiconductor film(s) inside the solar cell and following PCE improvement. Similar effect was observed for MAPbI₃ thin films conductivity in the work of Frolova et al. and in previous chapter of the Thesis. In this case V_{OC} becomes an ideal “threshold voltage” since it corresponds the state with the highest charge-carriers accumulation in the device and thus becomes the highest voltage device can sustain. Further biasing will most likely lead to the inter-layer ion migration and reduction-oxidation processes in the device.^{121,122}

Following the obtained results, we decided to take 1 V as a biasing voltage for the third stage of our work including long-term biasing. Since the most plausible way of device long-term degradation is supposed to be an interaction at the interfaces of different layers as well as possible mutual penetration of ions, we also decided to make devices with double combinations of hole-transport materials in the structure. Inorganic HTM|PTAA layers with direct PTAA-perovskite contact were included to reveal the influence of the inorganic HTM/perovskite interface. Solar cells where ITO was consequently covered with PTAA|CuI, PTAA|CuO_x, PTAA|CuSCN, were provided to identify the influence of the ITO-inorganic HTL contact and reveal possible interactions between them. Evolution of normalized average PCE depending on exposure time of constant 1 V biasing is presented in the heatmap (Figure 23). Evolutions for absolute device characteristics are given in Supplementary materials (Figure A5 in Appendix A).

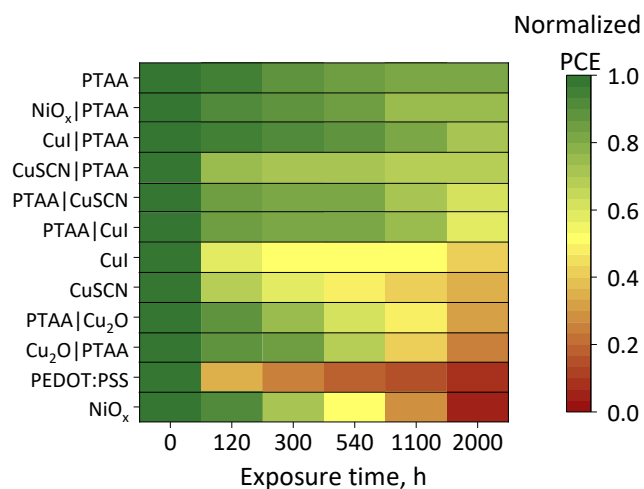


Figure 23. Evolution of normalized average efficiency for solar cells with various HTLs under constant 1V electric bias. HTLs are ranged from the best (top) to worst (bottom).

For majority of HTLs degradation goes rapidly in first 300 hours of exposure; then the rate of parameters decreasing slows down until the end of the experiment. According to the results, V_{OC} of solar cells does not contribute significantly into efficiency diminishment: in majority of the cases it remains constant; strongest contribution comes from J_{SC} and FF decreasing. J - V evolution examples for all systems are given in the Supplementary materials (Figure A6 in Appendix A).

According to the Figure 23 all HTMs and combinations of HTMs can be divided into 5 groups depending on their influence on device stability. The 1-st group contains PEDOT:PSS and NiO_x and represents the least stable HTMs which go to zero efficiency in less than 2000 h. For MAPbI₃ solar cells it was suggested that acidic PSS component chemically interacts with the methylamine – product of electrochemical degradation of perovskite.¹²³ In the present experiment, we have formamidinium cations as a component

of the perovskite layer and it is highly expectable for PSS to react with the product of FA^+ reduction, so PEDOT:PSS solar cells demonstrate the worst stability.

NiO_x being one of the HTM outsiders is also an expected result. Although surprisingly, combining NiO_x with PTAA dramatically improves device stability making this layer one of the most promising close to that of PTAA. This effect of PTAA layer introduction between NiO_x and perovskite evidences that the NiO_x -perovskite interface is responsible for the electrochemical degradation process in the ITO/ NiO_x / $\text{Cs}_{0.15}\text{FA}_{0.85}\text{PbI}_3$ / PC_{60}BM /Mg/Ag system. It is widely known that the interface between the oxide charge-transport layer and perovskite is chemically active.^{95,124} For NiO_x the possibility of interaction with iodide under electric bias,¹²⁵ formation of nickel iodide,^{126,127} and presence of the hydroxide layer on the NiO_x surface,^{128,129} which could chemically interact with perovskite components, was also demonstrated. The possible reaction of perovskite with water molecules that could remain in NiO_x layer due to fabrication process also cannot be excluded. Degradation can occur because of one or superposition of all pathways, but it is always a field-induced process, because reference samples stored in the dark inert atmosphere remained stable and retained almost 100% of the starting efficiency. Therefore, PTAA layer serves as a protection barrier between NiO_x aggressive factors and perovskite layer.

The second group of HTMs includes PTAA/ CuO_x and CuO_x /PTAA. Only these PTAA-containing HTLs demonstrate low stability, which can be due to oxygen, traces of water and KOH remaining in the CuO_x layer after immersing a CuI film in aqueous KOH solution. The third group contains CuSCN and CuI, and the fourth group is represented

by PTAA|CuI and PTAA|CuSCN. An interesting observation is that introduction of PTAA between ITO-CuSCN and ITO-CuI leads to the significant stability improvement. This result could specify that degradation in this case occurs at the ITO-Cu(I)X interface, but even better stability for the Cu(I)X|PTAA system than for the PTAA|Cu(I)X is observed. To sum up, it is most likely not the ITO-Cu(I)X interface responsible for the degradation, but the poor quality of Cu(I)X films on ITO leads to the pinholes in the layer. Most likely the Cu(I)X films were damaged during the following perovskite processing because they both can be slightly dissolved by polar solvents including DMF and DMSO.¹³⁰ As a result, we observe interaction of perovskite with ITO and accelerated degradation. Preliminary deposition of the PTAA layer on ITO removes the influence of ITO-perovskite interaction on device stability and improves it almost to the PTAA-only containing devices.

The fifth group contains the most stable CuI|PTAA, CuSCN|PTAA, NiO_x|PTAA and PTAA systems. A PTAA polymer seems to be chemically inert to the adjacent layers components which makes this material the best candidate for perovskite protection from electric field-induced degradation. Almost all systems containing PTAA in the hole transport layer (except CuO_x) kept more than 60% of starting PCE to the end of the experiment.

Thus, electrochemical degradation of perovskite is undoubtedly related to the adjacent HTM. Most likely defects and aggressive components (oxygen, water and hydroxide molecules, acidic PSS) in hole-transport layer induce interfacial field-driven chemical reactions becoming the initiators of perovskite layer decomposition. We

collected all important characteristics and proceeding factors of used HTMs in Table 1 for better visualizing and placed all HTLs according to their influence on device stability from best to worst divided into aforementioned five groups.

As we can observe, the bottom of the rating belongs to water-processed HTMs, which contain an oxygen/hydroxide or acidic component. Copper salts with the direct perovskite contact perform a bit better, but degradation is still significant most likely because of their partial removal by solvents used for perovskites processing (DMF and DMSO). Finally, the devices with a direct PTAA-perovskite contact demonstrate the best stability. PTAA is a toluene-processed polymer, which does not demonstrate any chemical reactivity to perovskite. This makes PTAA the best candidate for stability improvement and even protection of perovskite from other aggressive materials like NiO_x . Of course, it should be noted that PTAA could not protect perovskite from every danger like in CuO_x |PTAA case. Another noticeable thing is that except for water-processed HTLs there is a correlation between system stability and V_{OC} , V_{MPP} . This indicates the most suitable criteria for stability-improving HTLs including: chemical inertness towards perovskite component, using of perovskite-friendly solvents like toluene and chlorobenzene, complete insolubility in perovskite solvents, formation of tight flawless film and with highest possible V_{OC} and FF.

Table 3. Stability rating of all used HTLs

depending on their ability to boost the device stability and their characteristics.

HTLs from best to worst	V _{OC} start average, mV	V _{MPP} start average, mV	Solvents	Aggressive factors
PTAA	1020	900	Toluene	-
NiO _x PTAA	980	850	H ₂ O Toluene	O ²⁻ , OH ⁻ -
CuSCN PTAA	980	815	DPS Toluene	-
CuI PTAA	970	810	MeCN Toluene	-
PTAA CuSCN	980	810	Toluene DPS	- Partial flush
PTAA CuI	1000	800	Toluene MeCN	- Partial flush
CuSCN	770	620	DPS	Partial flush
CuI	790	610	MeCN	Partial flush
CuO _x PTAA	900	800	MeCN, H ₂ O-KOH Toluene	O ²⁻ -
PTAA CuO _x	960	810	Toluene MeCN, H ₂ O-KOH	- O ²⁻
NiO _x	910	730	H ₂ O	O ²⁻ , OH ⁻
PEDOT:PSS	800	750	H ₂ O	Acidic PSS

To confirm the positive influence of the PTAA layer we performed the ToF-SIMS analysis of NiO_x and NiO_x|PTAA cells degraded at 1 V for 2000 h (biased) and stored in the dark for the same time (fresh). The distribution of the marker ions corresponding to all solar cell components is reflected in the Figure 24 representing the full sequence of solar cell layers from the top Ag electrode to the bottom ITO substrate. Ion selection was concluded according to the publication of S. P. Harvey et al. about ToF-SIMS implementation for PSCs.¹³¹ Using the set of the chosen marker ions it is possible to observe their displacements after degradation. It should be noted that we performed a

ToF-SIMS analysis at the edge area of the biased electrode, because during the biasing we observed visual changes in almost all devices and all these changes emerged at the electrode edge and spread along the whole electrode subsequently.

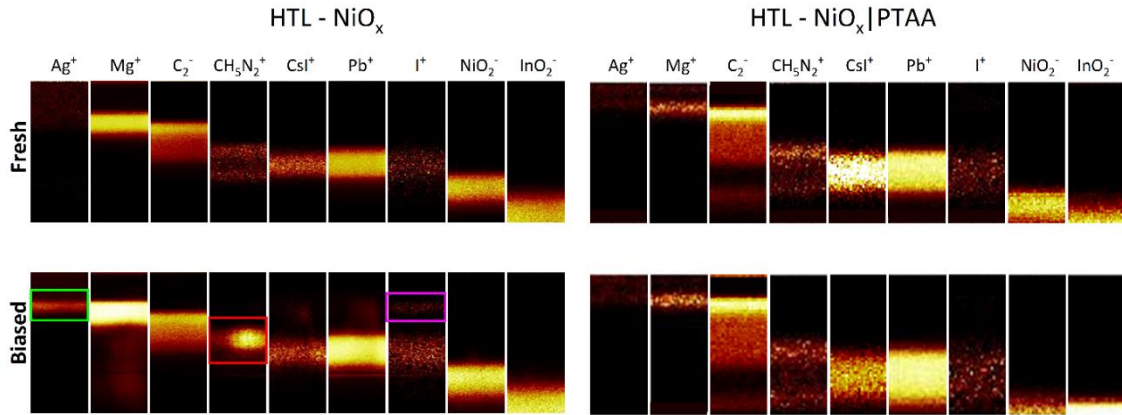


Figure 24. ToF-SIMS ions profiles for fresh and biased (2000 h) samples of solar cells with NiO_x and $\text{NiO}_x|\text{PTAA}$ as HTLs.

According to Figure 24 the degradation of the NiO_x -based solar cell after biasing can be observed. Significant changes are noticeable in the silver electrode: accumulation of Ag^+ ions on the edge with magnesium (green frame in Figure 24) indicates the chemical reaction of silver and formation of silver iodide, which is confirmed by I^+ appearance at the same position (purple frame in Figure 24). This corrosion of electrode edge is also visible on the optical photo of the electrode presented in Figure 25.

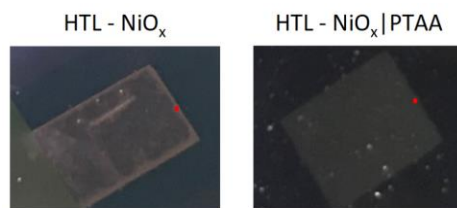


Figure 25. Optical photos of the solar cell backsides after 2000 h under constant biasing.

Magnesium also reacts with iodine according to the Mg^+ intensity increasing and traces remaining along the whole device depth. At the same time, PCBM and NiO_x layers represented by C_2^- and NiO_2^- ions do not demonstrate any significant changes.

The most severe degradation is visible in the perovskite layer: formamidinium ions were completely removed from their initial position and after biasing accumulated within the PCBM layer (red frame in Figure 24), while cesium and lead ions remain almost the same. A similar effect was observed for MAPbI_3 solar cells, where methylammonium cations diffused into ETL after biasing (Figure 13), which means the reduction of formamidinium ions and penetration of gaseous products into ETL is observed. According to Figure 26 these gaseous products find their way through the corroded silver and form a lot of pinholes in the electrode surface. Thus, almost complete destruction of the perovskite layer is observed with the following volatilization of organic species and iodine penetration through ETL and chemical reaction with the silver electrode.

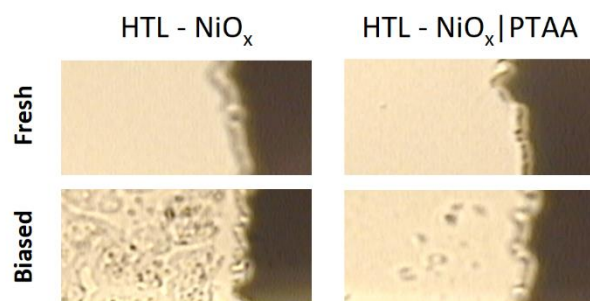


Figure 26. Optical microscope images of the top silver electrode edges before and after biasing for 2000 h.

At the same time, ToF-SIMS data for the NiO_x|PTAA solar cell does not demonstrate strong changes in perovskite ions distribution (Figure 24). Slight intermixing of all layers into each other can be explained by simple ion migration under the applied electric field. Optical photo of the NiO_x|PTAA device (Figure 25) confirm the absence of corrosion and microscopic photo of the electrode edge (Figure 26) confirms much lower concentration of pinholes.

5.3.2 Influence of electron-transport layers and top electrodes

To investigate the influence of electron-transport materials and top metal electrodes we decided to shift from the p-i-n to the n-i-p configuration for the best variability in both type of desired materials. The structure of the device is demonstrated in Figure 27a. ITO was covered with the applicable electron-transport material. Non-stoichiometric Cs_{0.12}FA_{0.8}PbI_{2.92} was selected as a photoactive layer because it was defined in the previous stage as the most stable perovskite material under the applied

electric field. PTAA was chosen as the best HTL in terms of stability, according to the previous results. V_2O_5 was added to improve charge extraction. We selected the set of electron-transport materials (ETMs): In_2O_3 , TiO_2 , ZnO and SnO_2 – well-known inorganic oxides,¹³² and covered them with C_{60} or fullerene derivative phenyl- C_{61} -butyric acid PCBA, which works as the analog to PCBM.¹³³ We decided to concentrate on these set of materials to have the best possible variability and did not consider small-molecule ETMs because according to our previous results they most likely will be chemically aggressive towards perovskite. And that was another reason for choosing the n-i-p configuration despite the risk of parasitic effects related to increased hysteresis.

For this stage, the experiment with “stepwise” biasing was passed down because we have already chosen 1 V as the optimal biasing voltage. So, we selected at least three samples for every device configuration with starting PCEs of approximately the same range. PCE depending on exposure time of constant 1 V biasing is presented in the Figure 27b, while evolution of absolute device parameters is presented in Supplementary materials (Figure A7, Appendix A). It should be noted that there are no data for pure oxides as ETLs, because such devices demonstrated zero stability, they either were not working since the moment of production or degraded right after preparation even before the biasing. So pure oxides should be placed at the bottom of the stability rating, which is of no surprise. We already have demonstrated the influence of the direct contact between perovskite and copper/nickel oxides on electrochemical stability of the device. Implementation of C_{60} between the oxide and perovskite improves the stability of the device slightly. All systems were able to work not more than 500 hours, the best of them

with titanium oxide is presented in Figure 27. And, finally, placing fullerene derivative PCBA between perovskite and metal oxide improves stability of the device significantly, especially in case of tin oxide. We can conclude that fullerene derivatives demonstrate the highest chemical inertness towards perovskite and are able to perform the higher level of isolation from aggressive layers compared to pure fullerene C₆₀.

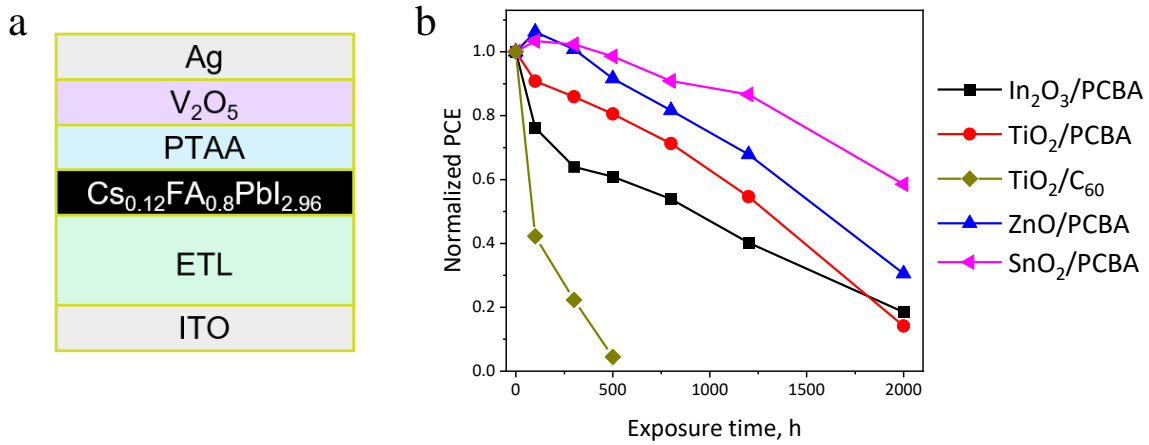


Figure 27. Schematic structure of solar cells used in the experiment of ETL variation (a).

Evolution of normalized average PCE of solar cells with various ETLs (b).

Finally, we decided to assemble the best possible configuration to test and compare various metals for the top electrode, since the only metals we used in all experiments with solar cells mentioned above were silver, as it is one of the most widespread and commonly used electrode material in solar energy generation industry.

Devices were assembled in configuration ITO/SnO₂/PCBA/Cs_{0.12}FA_{0.8}PbI_{2.96}/PTAA/V₂O₅/Metal electrode (Figure 28a). Metals for top electrode were varied as: Ag, Al, Au – the most demanded metals for photovoltaics.

Other available and tested metals were Bi, Mn, Cu, Co, Ni, Cr. Table 4 demonstrates average initial absolute PCE for all used systems in the electrode variation experiment. Figure 28b represents the evolution of normalized PCE depending on exposure time of constant 1 V biasing. Evolution of absolute device parameters is presented in Supplementary materials (Figure A8, Appendix A). As it is demonstrated, the best metals for top electrodes are gold and aluminum regarding both efficiency and stability.

Table 4. Average initial PCEs for investigated systems with various top electrodes.

Top electrode material	Au	Ag	Ni	Al	Co	Cr	Mn	Bi	Cu
Average PCE, %	18.0	17.8	17.2	16.6	12.3	9.4	8.2	6.3	5.1

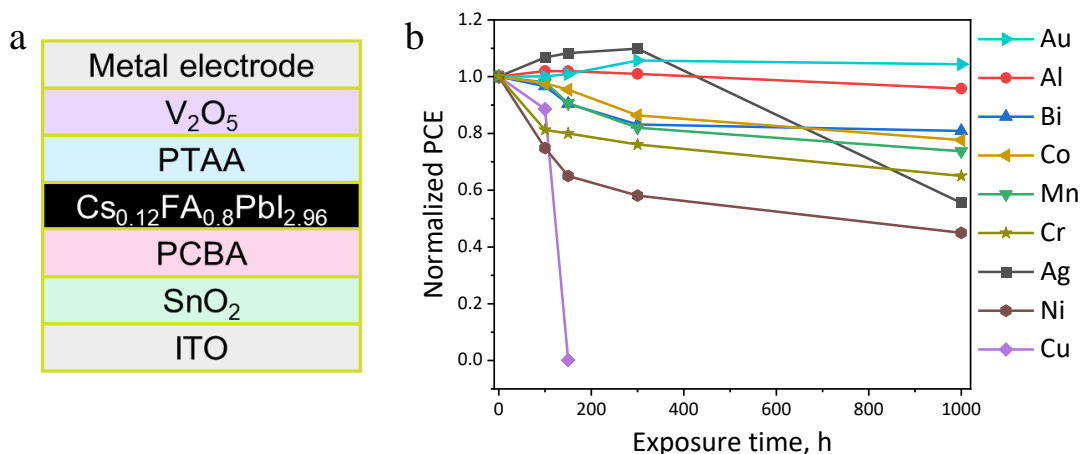


Figure 28. Schematic structure of solar cells used in the experiment of top electrode variation (a). Evolution of normalized average PCE of solar cells with various electrode materials (b).

In the Figure 24, the appearance of iodide anions was detected on the edge with the silver electrode. We also observed the corrosion of the top electrode in Figures 25 and 26. Thus, we can conclude that stability of the device depends on how strongly the electrode metal can react with iodine. The formation of iodides for some electrode metals was already mentioned in the literature.^{91-95,135} We hoped that we will be able to correlate the obtained result with some of the characteristics of all metals, but unfortunately, we were not able to define any dependances and assume that this matter requires additional long-term investigations, broadening the list of top electrode materials with other materials like carbon, carbon nano-tubes, ITO and etc. The only obvious conclusion could be made for now is that the gold electrodes demonstrate the best stability due to the low reactivity towards iodine.

5.3.4 Conclusion for the third stage

Based on the presented scientific findings, important guidelines for charge-transport material design for stable PSCs are established. It was demonstrated, that during the choice of the CTL for stable perovskite solar cells a special attention should be paid to the chemical inertness of CTL towards perovskite, using of perovskite-friendly solvents simultaneously with complete insolubility in perovskite solvents, formation of the tight flawless film and with the highest possible V_{OC} and FF of the complete device. Furthermore, special attention should be paid to the interface between the charge-transport layer and perovskite. In this regard, double CTLs consisting of the organic layer in direct contact with perovskite and supporting metal oxide are of great interest because

of organic-perovskite interface stability and inorganic material encapsulation properties combination.^{90,136}

Chapter 6. Conclusions

Herein, we revealed for the first time a comprehensive mechanism of previously poorly investigated electrochemical decomposition of $\text{CH}_3\text{NH}_3\text{PbI}_3$ using a set of microscopy techniques (optical, AFM, PL) and ToF-SIMS. We demonstrated that applied electric bias induces the oxidation of I^- to I_2 , which most likely remains trapped in the film in the form of polyiodides and, hence, the process can be conceivably reversed by reduction. On the contrary, reduction of organic methylammonium cation produces volatile products, which leave the film making the degradation irreversible and thus reduction becomes the crucial point of the whole process.

We also demonstrated the influence of chemical composition on electrochemical stability of bulk material and complete device and concluded that replacement of highly volatile MA^+ to the bigger cation FA^+ or inorganic Cs^+ improves stability, while variation of anion in the structure seems to have insignificant effect on device stability.

We proposed a general pathway for electrochemical degradation of solar cells. Small biasing voltage and duration lead to the electrochemical doping and efficiency increasing due to charge-carriers accumulation, but further biasing induces interlayer ion migration and even redox process in the perovskite layer, both processes confirmed by the ToF-SIMS technique. The latter occurs if an aggressive factor like oxygen, water, acidic or basic reagent comes from the adjacent charge-transport layer and initiates degradation.

We also presented the first systematic study on the influence of charge-transport materials and top electrodes on the field-induced degradation of perovskite solar cells.

And it was revealed that the most important factors for improving the solar cell stability are enhanced V_{OC} and FF of complete device, chemical inertness of adjacent charge-transport material (for example polymers or carbon-based materials) and its solvent towards perovskite (toluene, chlorobenzene), insolubility of CTLs in solvents for perovskite processing, formation of tight flawless films and, finally, the high thickness of perovskite layer. These conclusions can serve as material selection criteria for enhancement of perovskite solar cell stability.

We also think that method of measuring PCE(t) of solar cells introduced in this Thesis can be widely applied for the analysis of PSC stability because of its flexibility and possibility of parameter variation.

We strongly believe that our insightful results will lead new pathways for further development of stable perovskite photovoltaics.

Bibliography

- (1) Kojima, A.; Teshima, K.; Shirai, Y.; Miyasaka, T., Organometal halide perovskites as visible-light sensitizers for photovoltaic cells. *J. Am. Chem. Soc.* **2009**, *131*, 6050-6051.
- (2) NREL efficiency chart - <https://www.nrel.gov/pv/cell-efficiency.html>
- (3) Huang, F.; Li, M.; Siffalovic, P.; Cao, G.; Tian, J., From scalable solution fabrication of perovskite films towards commercialization of solar cells. *Energy Environ. Sci.* **2019**, *12*, 518-549.
- (4) Wojciechowski, K.; Forgács, D.; Rivera, T., From scalable solution fabrication of perovskite films towards commercialization of solar cells. *Sol. RRL* **2019**, 1900144.
- (5) Qui, L.; He, S.; Ono, L. K.; Liu, S.; Qi, A., Scalable fabrication of metal halide perovskite solar cells and modules. *ASC Energy Lett.* **2019**, *4*, 2147-2167.
- (6) Park, N. G.; Zhu, K., Scalable fabrication and coating methods for perovskite solar cells and solar modules. *Nat. Rev. Mater.* **2020**, *5*, 333-350.
- (7) Meng, X.; Xing, Z.; Hu, X.; Huang, Z.; Hu, T.; Tan, L.; Li, F.; Chen, Y., Stretchable Perovskite Solar Cells with Recoverable Performance. *Angew. Chem. Int. Ed.* **2020**, *59*, 16602-16608.
- (8) Kaltenbrunner, M.; Adam, G.; Glowacki, E. D.; Drack, M.; Schwödiauer, R.; Leonat, L.; Apaydin, D. H.; Groiss, H.; Scharber, M. C.; White, M. S.; Sariciftci, N. S.; Bauer, S., Flexible high power-per-weight perovskite solar cells with chromium oxide-metal contacts for improved stability in air. *Nature Mater.* **2015**, *14*, 1032-1039.

- (9) Boldyreva, A. G.; Akbulatov, A. F.; Tsarev, S. A.; Luchkin, S. Y.; Zhidkov, I. S.; Kurmaev, E. Z.; Stevenson, K. J.; Petrov, V. G.; Troshin, P. A., γ -Ray-Induced Degradation in the Triple-Cation Perovskite Solar Cells. *J. Phys. Chem. Lett.* **2019**, *10*, 813-818.
- (10) Wang, Z.; Song, Z.; Yan, Y.; Liu, S.; Yang, D., Perovskite – a Perfect Top Cell for Tandem Devices to Break the S-Q Limit. *Adv. Sci.* **2019**, *6*, 1801704
- (11) Zhua, Z.; Maa, K.; Xu, J., Perovskite tandem solar cells with improved efficiency and stability. *Journal of Energy Chem.* **2021**, *58*, 219-232
- (12) Dagar, J.; Castro-Hermosa, S.; Lucarelli, G.; Cacialli, F.; Brown, T. M., Highly efficient perovskite solar cells for light harvesting under indoor illumination via solution processed SnO₂/MgO composite electron transport layers. *Nano Energy* **2018**, *49*, 290-299.
- (13) Wang, K.-L.; Zhou, Y.-H.; Lou, Y.-H.; Wang, Z.-K., Perovskite indoor photovoltaics: opportunity and challenges. *Chem. Sci.* **2021**, *12*, 11936-11954.
- (14) Song, Z.; Abate, A.; Wathage, S. C.; Liyanage, G. K.; Phillips, A. B.; Steiner, U.; Graetzel, M.; Heben, M. J., Perovskite solar cell stability in humid air: partially reversible phase transitions in the PbI₂-CH₃NH₃I-H₂O system. *Adv. Energy Mater.* **2016**, *6*, 1600846.
- (15) Han, Y.; Dkhissi, Y.; Weber, K.; Pringle, J. M.; Bach, U.; Spiccia, L.; Cheng, Y., Degradation observations of encapsulated planar CH₃NH₃PbI₃ perovskite solar cells at high temperatures and humidity. *J. Mater. Chem. A* **2015**, *3*, 8139-8148.

- (16) Yang, J.; Siempelkamp, B. D.; Liu, D.; Kelly, T. L., Investigation of $\text{CH}_3\text{NH}_3\text{PbI}_3$ degradation rates and mechanisms in controlled humidity environments using in situ techniques. *ACS Nano* **2015**, *2*, 1955-1963.
- (17) Li, F.; Liu, M., Recent efficient strategies for improving the moisture stability of perovskite solar cells. *J. Mater. Chem. A* **2017**, *5*, 15447-15459.
- (18) Bryant, D.; Aristidou, N.; Pont, S.; Sanchez-molina, I.; Chotchunangatchaval, T.; Wheeler, S.; Durrant, R.; Haque, S. A. Light and oxygen induced degradation limits the operational stability of methylammonium lead triiodide perovskite solar cells. *Energy Environ. Sci.* **2016**, *9*, 1655-1660.
- (19) Ouyang, Y.; Li, Y.; Zhu, P.; Li, Q.; Gao, Y.; Tong, J.; Shi, L.; Zhou, Q.; Ling, C.; Chen, Q. et al. Photo-oxidative degradation of methylammonium lead iodide perovskite: mechanism and protection. *J. Mater. Chem. A* **2019**, *7*, 2275-2282.
- (20) Aranda, C. A.; Calìò, L.; Salado, M. Toward commercialization of stable devices: an overview on encapsulation of hybrid organic-inorganic perovskite solar cells. *Crystals* **2021**, *11*(5), 519.
- (21) Leijtens, T.; Bush, K.; Cheacharoen, R.; Beal, R.; Bowring, A.; McGehee, M. D. Towards enabling stable lead halide perovskite solar cells; interplay between structural, environmental, and thermal stability. *J. Mater. Chem. A* **2017**, *5*, 11483-11500.
- (22) Tasnim, A. T.; Al Mamun, A.; Marsillac, S.; Namkoong, G. A review: thermal stability of methylammonium lead halide based perovskite solar cells. *Appl. Sci.* **2019**, *9*, 188.

- (23) Hong, Q.; Xu, R.; Jin, T.; Tang, J.; Li, Y. Unraveling the light-induced degradation mechanism of CH₃NH₃PbI₃ perovskite films. *Organic Electronics* **2019**, *67*, 19-25.
- (24) Khenkin, M. V.; Anoop, K. M.; Katz, E. A.; Visoly-Fisher, I. Bias-dependent degradation of various solar cells: lessons for stability of perovskite photovoltaics. *Energy Environ. Sci.* **2019**, *12*, 550-558.
- (25) Green, M. A.; Ho-Baillie, A.; Snaith, H. J. The emergence of perovskite solar cells. *Nature Photonics* **2014**, *8*, 506-514.
- (26) Green F.; Shafie, S.; Lim, H. N.; Musa, A. O. Advancement on Lead-Free Organic-Inorganic Halide Perovskite Solar Cells: A Review. *Materials* **2018**, *11*(6), 1008.
- (27) Dong, Q.; Fang, Y.; Shao, Y.; Mulligan, P.; Qiu, J.; Cao, L.; Huang, J. Electron-Hole Diffusion Lengths > 175 μm in Solution-Grown CH₃NH₃PbI₃ Single Crystals. *Science* **2015**, *347*, 967-970.
- (28) Lee, M. M.; Teuscher, J.; Miyasaka, T.; Murakami, T. N.; Snaith, H. J. Efficient hybrid solar cells based on meso-superstructured organometal halide perovskites. *Science* **2012**, *338*, 643-647.
- (29) Leijtens, T.; Eperon, G. E.; Pathak, S.; Abate, A.; Lee M. M.; Snaith, H. J. Overcoming ultraviolet light instability of sensitized TiO₂ with meso-superstructured organometal tri-halide perovskite solar cells. *Nat. Commun.* **2013**, *4*, 2885.
- (30) Ono, L. K.; Leyden, M. R.; Wang, S.; Qi, Y. Organometal halide perovskite thin films and solar cells by vapor deposition. *J. Mater. Chem. A.* **2016**, *4*, 6693-6713.

- (31) He, M.; Zheng, D. J.; Wang, M. Y.; Lin, C. J.; Lin, Z. Q. High efficiency perovskite solar cells: from complex nanostructure to planar heterojunction. *J. Mater. Chem. A* **2014**, *2*, 5994-6003.
- (32) Meng, L.; You, J. B.; Guo, T. F.; Yang, Y. Recent Advances in the Inverted Planar Structure of Perovskite Solar Cells. *Acc. Chem. Res.* **2016**, *49*, 155-165.
- (33) Salim, T.; Sun, S. Y.; Abe, Y.; Krishna, A.; Grimsdale, A. C.; Lam, Y. M. Perovskite-based solar cells: impact of morphology and device architecture on device performance. *J. Mater. Chem. A* **2015**, *3*, 8943-8969.
- (34) Shao, Y.; Xiao, Z.; Bi, C.; Yuan, Y.; Huang, J. Origin and elimination of photocurrent hysteresis by fullerene passivation in CH₃NH₃PbI₃ planar heterojunction solar cells. *Nat. Commun.* **2014**, *5*, 5784.
- (35) Wang, C.; Xiao, C.; Yu, Y.; Zhao, D.; Awni, R. A.; Grice, C. R.; Ghimire, K.; Constantinou, I.; Liao, W.; Cimaroli, A. J.; Liu, P.; Chen, J.; Podraza, N. J.; Jiang, C.-S.; Al-Jassim, M. M.; Zhao, X.; Yan, Y. Understanding and eliminating hysteresis for highly efficient planar perovskite solar cells. *Adv. Energy Mater.* **2017**, *7*, 1700414.
- (36) Snaith, H. J.; Abate, A.; Ball, J. M.; Eperon, G. E.; Leijtens, T.; Noel, N. K.; Stranks, S. D.; Wang, J. T. W.; Wojciechowski, K.; Zhang, W. Anomalous hysteresis in perovskite solar cells. *J. Phys. Chem. Lett.* **2014**, *5*, 1511-1515.
- (37) Azpiroz, J. M.; Mosconi, E.; Bisquert, J.; De Angelis, F. Defect migration in methylammonium lead iodide and its role in perovskite solar cell operation. *Energy Environ. Sci.* **2015**, *8*, 2118-2127.

- (38) Li, C.; Tscheuschner, S.; Paulus, F.; Hopkinson, P. E.; Kießling, J.; Kohler, A.; Vaynzof, Y.; Huettner, S. Iodine migration and its effect on hysteresis in perovskite solar cells. *Adv. Mater.* **2016**, *28*, 2446-2454.
- (39) Kim, S.; Bae, S.; Lee, S.-W.; Cho, K.; Lee, K. D.; Kim, H.; Park, S.; Kwon, G.; Ahn, S.-W.; Lee, H.-M.; Kang, Y.; Lee, H.-S.; Kim, D. Relationship between ion migration and interfacial degradation of CH₃NH₃PbI₃ perovskite solar cells under thermal conditions. *Sci. Rep.* **2017**, *7*, 1200.
- (40) Liu, T.; Chen, K.; Hu, Q.; Zhu, R.; Gong, Q. Inverted perovskite solar cells: progresses and perspectives, *Adv. Energy Mater.* **2016**, *6*, 1600457.
- (41) Djurisic, A. B.; Liu, F. Z.; Tam, H. W.; Wong, M. K.; Ng, A.; Surya, C.; Chen, W.; He, Z. B. Perovskite solar cells - An overview of critical issues. *Prog. Quantum Electron.* **2017**, *53*, 1-37.
- (42) Zhang, T.; Wang, M.; Yang, H. A Review of the Energy Performance and Life-Cycle Assessment of Building-Integrated Photovoltaic (BIPV). *Energies* **2018**, *11*(11), 3157
- (43) Xiao, Z.; Yuan, Y.; Shao, Y.; Wang, Q.; Dong, Q.; Bi, C.; Sharma, P.; Gruverman, A.; Huang, J. Giant switchable photovoltaic effect in organometal trihalide perovskite devices. *Nat. Mater.* **2015**, *14*, 193.
- (44) Van Reenen, S.; Kemerink, M.; Snaith, H. J. Modeling Anomalous Hysteresis in Perovskite Solar Cells. *J. Phys. Chem. Lett.* **2015**, *6*, 3808-3814.
- (45) Zhang, Y.; Liu, M.; Eperon, G. E.; Liejtens, T. C.; McMeekin, D.; Saliba, M.; Zhang, W.; de Bastiani, M.; Petrozza, A.; Herz, L. M.; Johnston, M. B.; Lin, H.; Snaith,

- H. J. Charge selective contacts, mobile ions and anomalous hysteresis in organic–inorganic perovskite solar cells. *Mater. Horiz.* **2015**, *2*, 315-322.
- (46) Roiati, V.; Mosconi, E.; Listorti, A.; Colella, S.; Gigli, G.; de Angelis, F. Stark effect in perovskite/TiO₂ solar cells: evidence of local interfacial order. *Nano Lett.* **2014**, *14*, 2168.
- (47) Carrillo, J.; Guerrero, A.; Rahimnejad, S.; Almora, O.; Zarazua, I.; MasMarza, E.; Bisquert, J.; Garcia-Belmonte, G. Ionic Reactivity at Contacts and Aging of Methylammonium Lead Triiodide Perovskite Solar Cells. *Adv. Energy Mater.* **2016**, *6*, 1502246.
- (48) Frolova, L. A.; Dremova, N. N.; Troshin, P. A. The chemical origin of the p-type and n-type doping effects in the hybrid methylammonium–lead iodide (MAPbI₃) perovskite solar cells. *Chem. Commun.* **2015**, *51*, 14917-14920.
- (49) Bae, S.; Kim, S.; Lee, S.-W.; Cho, K. J.; Park, S.; Lee, S.; Kang, Y.; Lee, H.-S.; Kim, D. Electric-field-induced degradation of methylammonium lead iodide perovskite solar cells. *J. Phys. Chem. Lett.* **2016**, *7*, 3091-3096.
- (50) Yuan, Y.; Li, T.; Wang, Q.; Xing, J.; Gruverman, A.; Huang, J. Anomalous photovoltaic effect in organic-inorganic hybrid perovskite solar cells. *Sci. Adv.* **2017**, *3*, e1602164.
- (51) Saraf, R.; Maheshwari, V. Self-powered photodetector based on electric field induced effects in MAPbI₃ perovskite with improved stability. *ACS Appl. Mater. Interfaces* **2018**, *10*, 21066-21072.

- (52) Li, C.; Guerrero, A.; Huettner, S.; Bisquert, J. Unravelling the role of vacancies in lead halide perovskite through electrical switching of photoluminescence. *Nature Communications* **2018**, *9*, 5113.
- (53) Rizzo, A.; Lamberti, F.; Buonomo, M.; Wrachien, N.; Torto, L.; Lago, N.; Sansoni, S.; Pilot, R.; Prato, M.; Michieli, N. et al. Understanding lead iodide perovskite hysteresis and degradation causes by extensive electrical characterization. *Sol. Energy Mater. Sol. Cells* **2019**, *189*, 43-52.
- (54) Leijtens, T.; Hoke, E. T.; Grancini, G.; Slotcavage, D. J.; Eperon, G. E.; Ball, J. M.; De Bastiani, M.; Bowring, A. R.; Martino, N.; Wojciechowski, K. et al. Mapping electric field-induced switchable poling and structural degradation in hybrid lead halide perovskite thin films. *Adv. Energy Mater.* **2015**, *5*, 1500962.
- (55) Yuan, Y.; Chae, J.; Shao, Y.; Wang, Q.; Xiao, Z.; Centrone, A.; Huang, J. Photovoltaic switching mechanism in lateral structure hybrid perovskite solar cells. *Adv. Energy Mater.* **2015**, *5*, 1500615.
- (56) Yuan, Y.; Wang, Q.; Shao, Y.; Lu, H.; Li, T.; Gruverman, A.; Huang, J. Electric-field-driven reversible conversion between methylammonium lead triiodide perovskites and lead iodide at elevated temperatures. *Adv. Energy Mater.* **2016**, *6*, 1501803.
- (57) Deng, X.; Wen, X.; Lau, C. F. J.; Young, T.; Yun, J.; Sani, M. A.; Huang, S.; Ho-Baillie, A. W. Y. Electric field induced reversible and irreversible photoluminescence responses in methylammonium lead iodide perovskite. *J. Mater. Chem. C* **2016**, *4*, 9060-9068.

- (58) Li, C.; Guerrero, A.; Zhong, Y.; Gräser, A.; Luna, C. A. M.; Köhler, J.; Bisquert, J.; Hildner, R.; Huettnner, S. Real-time observation of iodide ion migration in methylammonium lead halide perovskites. *Small* **2017**, *13*, 1701711.
- (59) Birkhold, S. T.; Precht, J. T.; Liu, H.; Giridharagopal, R.; Eperon, G. E.; Schmidt-Mende, L.; Li X.; Ginger, D. S. Interplay of mobile ions and injected carriers creates recombination centers in metal halide perovskites under bias. *ACS Energy Lett.* **2018**, *3*, 1279-1286.
- (60) Luchkin, S. Yu.; Akbulatov, A. F.; Frolova, L. A.; Griffin, M. P.; Dolocan, A.; Gearba, R.; Bout, D. A. V.; Troshin, P. A.; Stevenson, K. J. Reversible and irreversible electric field induced morphological and interfacial transformations of hybrid lead iodide perovskites. *ACS Appl. Mater. Interfaces* **2017**, *9*, 3347-3352.
- (61) Yun, J. S.; Seidel, J.; Kim, J.; Soufiani, A. M.; Huang, S.; Lau, J.; Jeon, N. J.; Seok, S. I.; Green, M. A.; Ho-Baillie, A. Critical role of grain boundaries for ion migration in formamidinium and methylammonium lead halide perovskite solar cells. *Adv. Energy Mater.* **2016**, *6*, 1600330.
- (62) Bowring, A. R.; Bertoluzzi, L.; O'Regan, B. C., McGehee, M. D. Reverse bias behavior of halide perovskite solar cells. *Adv. Energy Mater.* **2017**, *8*, 1702365.
- (63) Handa, T.; Tex, D. M.; Shimazaki, A.; Aharen, T.; Wakamiya, A.; Kanemitsu, Y. Optical characterization of voltage-accelerated degradation in $\text{CH}_3\text{NH}_3\text{PbI}_3$ perovskite solar cells. *Optics Express* **2016**, *24*, A917-A924.
- (64) Barbé, J.; Kumar, V.; Newman, M. J.; Lee, H. K. H.; Jain, S. M.; Chen, H.; Charbonneau, C.; Rodenburg, C. Dark electrical bias effects on moisture-induced

degradation in inverted lead halide perovskite solar cells measured by using advanced chemical probes. *Sust. En. Fuels* **2018**, *2*, 905-914.

(65) Li, X.; Wang, X.; Zhang, W.; Wu, Y.; Gao, F.; Fang, J. The effect of external electric field on the performance of perovskite solar cells. *Organic Electronics* **2015**, *18*, 107-112.

(66) Bruno, A.; Cortecchia, D.; Chin, X. Y.; Fu, K.; Boix, P. P.; Mhaisalkar, S.; Soci, C. Temperature and electrical poling effects on ionic motion in MAPbI₃ photovoltaic cells. *Adv. Energy Mater.* **2017**, *7*, 1700265.

(67) Swartz, C. H.; Khakurel, N.; Najar, S. R.; Hossain, M. I.; Zakhidov, A. Temperature- and bias-dependent degradation and regeneration of perovskite solar cells with organic and inorganic hole transport layers. *Phys. Status Solidi A* **2021**, *218*(7), 2000721.

(68) Jeangros, Q.; Duchamp, M.; Werner, J.; Kruth, M.; Dunin-Borkowski, R. E.; Niesen, B.; Ballif, C.; Hessler-Wyser, A. In situ TEM analysis of organic-inorganic metal-halide perovskite solar cells under electrical bias. *Nano Lett.* **2016**, *16*, 7013-7018.

(69) Yadav, P.; Prochowicz, D.; Alharbi, E. A.; Zakeeruddin, S. M.; Grätzel, M. Intrinsic and interfacial kinetics of perovskite solar cells under photo and bias-induced degradation and recovery. *J. Mater. Chem. C* **2017**, *5*, 7799-7805.

(70) Duong, T.; Mulmudi, H. K.; Wu, Y.; Fu, X.; Shen, H.; Peng, J.; Wu, N.; Nguyen, H. T.; Macdonald, D.; Lockrey, M. et al. Light and electrically induced phase segregation and its impact on the stability of quadruple cation high bandgap perovskite solar cells. *ACS Appl. Mater. Interfaces* **2017**, *9*(32), 26859-26866.

- (71) Smith, E. C.; Ellis, C. L. C.; Javaid, H.; Renna, L. A.; Liu, Y.; Russell, T. P.; Bag, M.; Venkataraman, D. Interplay between ion transport, applied bias, and degradation under illumination in hybrid perovskite p-i-n devices. *J. Phys. Chem. C* **2018**, *122*(25), 13986-13994.
- (72) Jung, H. J.; Kim, D.; Kim, S.; Park, J.; Dravid, V. P.; Shin, B. Stability of halide perovskite solar cell devices: in situ observation of oxygen diffusion under biasing. *Adv. Mater.* **2018**, *30*(39), 1802769.
- (73) Anoop, K. M.; Khenkin, M. V.; Di Giacomo, F.; Galagan, Y.; Rahmany, S.; Etgar, L.; Katz, E. A.; Visoly-Fisher, I. Bias-dependent stability of perovskite solar cells studied using natural and concentrated sunlight. *Sol. RRL* **2019**, 1900335.
- (74) Ni, Z.; Jiao, H.; Fei, C.; Gu, H.; Xu, S.; Yu, Z.; Yang, G.; Deng, Y.; Jiang, Q.; Liu, Y. et al. Evolution of defects during the degradation of metal halide perovskite solar cells under reverse bias and illumination. *Nat. Energy* **2022**, *7*, 65-73.
- (75) Domanski, K.; Roose, B.; Matsui, T.; Saliba, M.; Turren-Cruz, S.-H.; Correa-Baena, J.-P.; Carmona, C. R.; Richardson, G.; Foster, J. M.; De Angelis, F. et al. Migration of cations induces reversible performance losses over day/night cycling in perovskite solar cells. *Energy Environ. Sci.* **2017**, *10*, 604-613.
- (76) Khudiyakov, D. V.; Ganin, D. V.; Lyashedko, A. D.; Frolova, L. A.; Troshin, P. A.; Lobach A. S. Nonlinear optical absorption in thin halide perovskite films under femtosecond excitation at wavelengths of 1064 and 532 nm. *Quantum Electronics* **2021**, *51*, 211–216.

- (77) Tsarev, S.; Olthof, S.; Boldyreva, A. G.; Aldoshin, S. M.; Stevenson, K. J.; Troshin, P. A. Reactive modification of zinc oxide with methylammonium iodide boosts the operational stability of perovskite solar cells. *Nano Energy* **2021**, *83*, 105774.
- (78) Turren-Cruz, S.-H.; Hagfeldt, A.; Saliba, M. Methylammonium-free, high-performance and stable perovskite solar cells on a planar architecture. *Science* **2018**, *362*, 449-453.
- (79) López-González, M.C.; del Pozo, G.; Martín-Martín, D.; Muñoz-Díaz, L.; Pérez-Martínez, J.C.; Hernández-Balaguera, E.; Arredondo, B.; Galagan, Y.; Najafi, M.; Romero, B. Evaluation of Active Layer Thickness Influence in Long-Term Stability and Degradation Mechanisms in CsFAPbI₃ Perovskite Solar Cells. *Appl. Sci.* **2021**, *11*, 11668.
- (80) Gao, Y.; Dong, Y.; Huang, K.; Zhang, C.; Liu, B.; Wang, S.; Shi, J.; Xie, H.; Huang, H.; Xiao, S.; He, J.; Gao, Y.; Hatton, R. A.; Yang, J. Highly Efficient, Solution-Processed CsPbI₂Br Planar Heterojunction Perovskite Solar Cells via Flash Annealing. *ACS Photonics* **2018**, *5*, 4104-4110.
- (81) Zhu, J.; Niu, K.; Li, M.; Lin, M.; Li, J.; Wang, Z. PEDOT:PSS-CrO₃ composite hole-transporting layer for high-performance pi-n structure perovskite solar cells. *Organic Electronics* **2018**, *54*, 9–13.
- (82) Fakharuddin, A.; De Rossi, F.; Watson, T. M.; Schmidt-Mende, L.; Jose, R. Research Update: Behind the high efficiency of hybrid perovskite solar cells. *APL Mater.* **2016**, *4*, 091505

- (83) Eames, C.; Frost, J. M.; Barnes, P. R. F.; O'Regan, B. C.; Walsh A.; Islam, M. S. Ionic transport in hybrid lead iodide perovskite solar cells. *Nat. Commun.* **2015**, *6*, 7497.
- (84) Svensson, P. H.; Kloo, L. Synthesis, structure, and bonding in polyiodide and metal iodide-iodine systems. *Chem. Rev.* **2003**, *103*, 1649-1684.
- (85) Topol, L. E. Thermodynamic studies in the tetramethylammonium iodide-polyiodide and tetraethylammonium iodide-polyiodide systems. *Inorganic Chemistry* **1971**, *10*, 736-740.
- (86) Meggiolaro, D.; Motti, S. G.; Mosconi, E.; Barker, A. J.; Ball, J.; Perini, C. A. R.; Deschler, F.; Petrozza, A.; De Angelis, F. Iodine chemistry determines the defect tolerance of lead-halide perovskites. *Energy Environ. Sci.* **2018**, *11*, 702-713.
- (87) Turkevych, I.; Kazaoui, S.; Belich, N. A.; Grishko, A. Y.; Fateev, S. A.; Petrov, A. A.; Urano, T.; Aramaki, S.; Kosar, S.; Kondo, M. et al. Strategic advantages of reactive polyiodide melts for scalable perovskite photovoltaics. *Nature Nanotechnology* **2019**, *14*, 57-64.
- (88) Akbulatov, A. F.; Frolova, L. A.; Griffin, M. P.; Gearba, I. R.; Dolocan, A.; Vanden Bout, D. A.; Tsarev, S.; Katz, E. A.; Shestakov, A. F.; Stevenson, K. J. et al. Effect of electron-transport material on light-induced degradation of inverted planar junction perovskite solar cells. *Adv. Energy Mater.* **2017**, *7*, 1700476.
- (89) Zhu, Q.; Cox, D. E.; Fischer, J. E.; Kniaz, K.; McGhie, A. R.; Zhou, O. Intercalation of solid C₆₀ with iodine. *Nature* **1992**, *355*, 712-714.
- (90) Huong, P. V. Raman spectra and structure of iodine and bromine intercalated fullerenes C₆₀ and C₇₀. *Solid State Communications* **1993**, *88*, 23-26.

- (91) Kato, Y.; Ono, L. K.; Lee, M. V.; Wang, S.; Raga, S. R.; Qi, Y. Silver iodide formation in methyl ammonium lead iodide perovskite solar cells with silver top electrodes. *Adv. Mater. Interfaces* **2015**, *2*, 1500195.
- (92) Li, J.; Dong, Q.; Li, N.; Wang, L. Direct evidence of ion diffusion for the silver-electrode-induced thermal degradation of inverted perovskite solar cells. *Adv. Energy Mater.* **2017**, 1602922.
- (93) Drozdov, M. N.; Yunin, P. A.; Travkin, V. V.; Koptyaev, A. I.; Pakhomov, G. L. Direct imaging of current-induced transformation of a perovskite/electrode interface. *Adv. Mater. Interfaces* **2019**, *6*, 1900364.
- (94) Li, X.; Ding, H.; Li, G.; Wang, Y.; Fang, Z.; Yang, S.; Ju, H.; Zhu, J. In situ investigations of interfacial degradation and ion migration at CH₃NH₃PbI₃ perovskite/Ag interface. *Chinese Journal of Chemical Physics* **2019**, *32*, 299-305.
- (95) Lee, H.; Lee, C. Analysis of ion-diffusion-induced interface degradation in inverted perovskite solar cells via restoration of the Ag electrode. *Adv. Energy Mater.* **2017**, 1702197.
- (96) Kulbak, M.; Gupta, S.; Kedem, N.; Levine, I.; Bendikov, T.; Hodes, G.; Cahen, D. Cesium enhances long-term stability of lead bromide perovskite-based solar cells. *J. Phys. Chem. Lett.* **2016**, *7*, 167-172.
- (97) Duan, J.; Zhao, Y.; He, B.; Tang, Q. Simplified perovskite solar cell with 4.1% efficiency employing inorganic CsPbBr₃ as light absorber. *Small* **2018**, *14*, 1704443.

- (98) Ding, J.; Zhao, Y.; Duan, J.; He, B.; Tang, Q. Alloy-controlled work function for enhanced charge extraction in all-inorganic CsPbBr₃ perovskite solar cells. *Chem. Sus. Chem.* **2018**, *11*, 1432-1437.
- (99) Chen, M.; Ju, M.-G.; Garces, H. F.; Carl, A. D.; Ono, L. K.; Hawash, Z.; Zhang, Y.; Shen, T.; Qi, Y.; Grimm, R. L. et al. Highly stable and efficient all-inorganic lead-free perovskite solar cells with native-oxide passivation. *Nat. Commun.* **2019**, *10*, 16.
- (100) Ito, N.; Kamarudin, M. A.; Hirotsu, D.; Zhang, Y.; Shen, Q.; Ogomi, Y.; Iikubo, S.; Minemoto, T.; Yoshino, K.; Hayase, S. Mixed Sn–Ge perovskite for enhanced perovskite solar cell performance in air. *J. Phys. Chem. Lett.* **2018**, *9*, 1682-1688.
- (101) Minns, J. L.; Zajdel, P.; Chernyshov, D.; van Beek, W.; Green, M. A. Structure and interstitial iodide migration in hybrid perovskite methylammonium lead iodide. *Nat. Commun.* **2017**, *8*, 15152.
- (102) Troughton, J.; Gasparini, N.; Baran, D. Cs_{0.15}FA_{0.85}PbI₃ perovskite solar cells for concentrator photovoltaic applications. *J. Mater. Chem. A* **2018**, *6*, 21913-21917.
- (103) Zheng, E.; Niu, Z.; Tosado, G. A.; Dong, H.; Albrikan, Y.; Yu, Q. Revealing stability of inverted planar MA-free perovskite solar cells and electric field-induced phase instability. *J. Phys. Chem. C* **2020**, *124*(34), 18805-18815.
- (104) Heo, J. H.; Im, S. H.; Noh, J. H.; Mandal, T. N.; Lim, C.-S.; Chang, J. A.; Lee, Y. H.; Kim, H.-J.; Sarkar, A.; Nazeeruddin, M. K. et al. Efficient inorganic-organic hybrid heterojunction solar cells containing perovskite compound and polymeric hole conductors. *Nat. Photonics* **2013**, *7*, 486-491.

- (105) Elnaggar, M.; Boldyreva, A. G.; Elshobaki, M.; Tsarev, S. A.; Fedotov, Y. S.; Yamilova, O. R.; Bredikhin, S. I.; Stevenson, K. J.; Aldoshin, S. M.; Troshin, P. A. Decoupling contributions of charge-transport interlayers to light-induced degradation of p-i-n perovskite solar cells. *RRL Solar* **2020**, *4*(9), 2000191.
- (106) Krebs, F. C.; Gevorgyan, S. A.; Alstrup, J. A roll-to-roll process to flexible polymer solar cells: model studies, manufacture and operational stability studies. *J. Mater. Chem.* **2009**, *19*, 5442-5451.
- (107) Shin, S. S.; Yeom, E. J.; Yang, W. S.; Hur, S.; Kim, M. G.; Im, J.; Seo, J.; Noh, J. H.; Seok, S. I. Colloidally prepared La-doped BaSnO₃ electrodes for efficient, photostable perovskite solar cells. *Science* **2017**, *356*, 167-171.
- (108) Liu, Z.; Krückemeier, L.; Krogmeier, B.; Klingebiel, B.; Márquez, J. A.; Levchenko, S.; Öz, S.; Mathur, S.; Rau, U.; Unold, T.; Kirchartz, T. Open-circuit voltages exceeding 1.26 V in planar methylammonium lead iodide perovskite solar cells. *ACS Energy Lett.* **2019**, *4*, 110-117.
- (109) Zuo, C.; Ding, L. Solution-processed Cu₂O and CuO as hole transport materials for efficient perovskite solar cells. *Small* **2015**, *11*, 5528-5532.
- (110) Chaudhary, N.; Chaudhary, R.; Kesari, J. P.; Patra, A.; Chand, S. Copper thiocyanate (CuSCN): an efficient solution-processable hole transporting layer in organic solar cells. *J. Mater. Chem. C* **2015**, *3*, 11886-11892.
- (111) Chen, J. Z.; Park, N. G. Inorganic hole transporting materials for stable and high efficiency perovskite solar cells. *J. Phys. Chem. C* **2018**, *122*(25), 14039-14063.

- (112) Chen, W.; Zhou, Y.; Wang, L.; Wu, Y.; Tu, B.; Yu, B.; Liu, F.; Tam, H. W.; Wang, G.; Djurišić, A. B. et al. Molecule-doped nickel oxide: verified charge transfer and planar inverted mixed cation perovskite solar cell. *Adv. Mater.* **2018**, *30*(20), 1800515.
- (113) Liu, C.; Zhang, L.; Li, Y.; Zhou, X.; She, S.; Wang, X.; Tian, Y.; Jen, A. K. Y.; Xu, B. Highly stable and efficient perovskite solar cells with 22.0% efficiency based on inorganic-organic dopant-free double hole transporting layers. *Adv. Funct. Mater.* **2020**, *30*(28), 1908462.
- (114) Pashaei, B.; Bellani, S.; Shahroosvand, H.; Bonaccorso, F. Molecularly engineered hole-transport material for low-cost perovskite solar cells. *Chem. Sci.* **2020**, *11*, 2429-2439.
- (115) Khenkin, M. V.; Katz, E. A.; Abate, A.; Bardizza, G.; Berry, J. J.; Brabec, C.; Brunetti, F.; Bulović, V.; Burlingame, Q.; Di Carlo A. et al. Consensus statement for stability assessment and reporting for perovskite photovoltaics based on ISOS procedures. *Nat. Energy* **2020**, *5*, 35-49.
- (116) Domanski, K.; Alharbi, E. A.; Hagfeldt, A.; Grätzel M.; Tress, W. Systematic investigation of the impact of operation conditions on the degradation behaviour of perovskite solar cells. *Nat. Energy* **2018**, *3*, 61-67.
- (117) Nie, W.; Blancon, J.-C.; Neukirch, A. J.; Appavoo, K.; Tsai, H.; Chhowalla, M.; Alam, M. A.; Sfeir, M. Y.; Katan, C.; Even, J. et al. Light-activated photocurrent degradation and self-healing in perovskite solar cells. *Nat. Commun.* **2016**, *7*, 11574.
- (118) Bastos, J. P.; Paetzold, U. W.; Gehlhaar, R.; Qiu, W.; Cheyns, D.; Surana, S.; Spampinato, V.; Aernouts T.; Poortmans, J. Light-induced degradation of perovskite

solar cells: the influence of 4-tert-butyl pyridine and gold. *Adv. Energy Mater.* **2018**, 8(23), 1800554.

(119) Carlson D. E.; Rajan, K. The reversal of light-induced degradation in amorphous silicon solar cells by an electric field. *Appl. Phys. Lett.* **1997**, 70, 2168-2170.

(120) Faria, G. C.; Coutinho, D. J.; von Seggern, H.; Fari, R. M. Doping mechanism in organic devices: Effects of oxygen molecules in poly(3-hexylthiophene) thin films. *Org. Electron.* **2018**, 57, 298-304.

(121) Schwenzler, J. A.; Rakocevic, L.; Gehlhaar, R.; Abzieher, T.; Gharibzadeh, S.; Moghadamzadeh, S.; Quintilla, A.; Richards, B. S.; Lemmer, U.; Paetzold, U. W. Temperature variation-induced performance decline of perovskite solar cells. *ACS Appl. Mater. Interfaces* **2018**, 10(19), 16390-16399.

(122) Besleaga, C.; Abramiuc, L. E.; Stancu, V.; Tomulescu, A. G.; Sima, M.; Trinca, L.; Plugaru, N.; Pintilie, L.; Nemnes, G. A.; Iliescu, M. et al. Iodine migration and degradation of perovskite solar cells enhanced by metallic electrodes. *J. Phys. Chem. Lett.* **2016**, 7(24), 5168-5175.

(123) Zhao, Y.; Zhou, W.; Tan, H.; Fu, R.; Li, Q.; Lin, F.; Yu, D.; Walters, G.; Sargent E. H.; Zhao, Q. Mobile-ion-induced degradation of organic hole-selective layers in perovskite solar cells. *J. Phys. Chem. C* **2017**, 121(27), 14517-14523.

(124) Cho, A. N.; Park, N. G. Impact of interfacial layers in perovskite solar cells, *ChemSusChem* **2017**, 10(19), 3687-3704.

- (125) Głowienka, D.; Zhang, D.; Di Giacomo, F.; Najafi, M.; Veenstra, S.; Szmytkowski, J.; Galagan, Y. Role of surface recombination in perovskite solar cells at the interface of HTL/CH₃NH₃PbI₃. *Nanomater. Energy* **2020**, *67*, 104186.
- (126) Di Girolamo, D.; Matteocci, F.; Kosasih, F. U.; Chistiakova, G.; Zuo, W.; Divitini, G.; Korte, L.; Ducati, C.; Di Carlo, A.; Dini D. et al. Stability and dark hysteresis correlate in NiO-based perovskite solar cells. *Adv. Energy Mater.* **2019**, *9*(31), 1901642.
- (127) Boldyreva, A. G.; Zhidkov, I. S.; Tsarev, S.; Akbulatov, A. F.; Tepliakova, M. M.; Fedotov, Y. S.; Bredikhin, S. I.; Postnova, E. Yu.; Luchkin, S. Yu.; Kurmaev, E. Z. et al. Unraveling the impact of hole transport materials on photostability of perovskite films and p-i-n solar cells. *ACS Appl. Mater. Interfaces* **2020**, *12*(16), 19161-19173.
- (128) W. A. Dunlap-Shohl, T. Li and D. B. Mitzi, Interfacial effects during rapid lamination within MAPbI₃ thin films and solar cells. *ACS Appl. Energy Mater.* **2019**, *2*(7), 5083-5093.
- (129) Di Girolamo, D.; Di Giacomo, F.; Matteocci, F.; Marrani, A. G.; Dini, D.; Abate, A.; Di Girolamo D. Progress, highlights and perspectives on NiO in perovskite photovoltaics, *Chem. Sci.* **2020**, *11*, 7746-7759.
- (130) Islam, M. B.; Pant, N.; Yanagida, M.; Shirai, Y.; Miyano, K. Effect of hydroxyl groups in NiO_x on the open circuit voltage of lead iodide perovskite solar cells. *Jpn. J. Appl. Phys.* **2018**, *57*, 08RE06.

- (131) Chaudhary, N.; Chaudhary, R.; Kesari, J. P.; Patra, A. An eco-friendly and inexpensive solvent for solution processable CuSCN as a hole transporting layer in organic solar cells. *Opt. Mater.* **2017**, *69*, 367-371.
- (132) Dkhili, M.; Lucarelli, G.; De Rossi, F.; Taheri, B.; Hammedi, K.; Ezzaouia, H.; Brunetti, F.; Brown, T. M. Attributes of High-Performance Electron Transport Layers for Perovskite Solar Cells on Flexible PET versus on Glass. *ACS Appl. Energy Mater.* **2022**, *5*(4), 4096-4107.
- (133) Wang, J.; Datta, K.; Weijtens, C. H. L.; Wienk, M. M.; Janssen, R. A. J. Insights into Fullerene Passivation of SnO₂ Electron Transport Layers in Perovskite Solar Cells. *Adv. Funct. Mater.* **2019**, *29*, 1905883.
- (134) Harvey, S. P.; Messinger, J.; Zhu, K.; Luther, J. M.; Berry, J. J. Investigating the effects of chemical gradients on performance and reliability within perovskite solar cells with ToF-SIMS. *Adv. Energy Mater.* **2020**, *10*, 1903674.
- (135) Shlenskaya, N. N.; Belich, N. A.; Gratzel, M.; Goodilin, E. A.; Tarasov, A. B. Light-induced reactivity of gold and hybrid perovskite as a new possible degradation mechanism in perovskite solar cells. *J. Mater. Chem. A* **2018**, *6*, 1780.
- (136) Tepliakova, M. M.; Mikheeva, A. N.; Somov, P. A.; Statnik, E. S.; Korsunsky, A. M.; Stevenson, K. J. Combination of metal oxide and polytriarylamine: a design principle to improve the stability of perovskite solar cells. *Energies* **2021**, *14*(16), 5115.

Appendix A. Supplementary materials

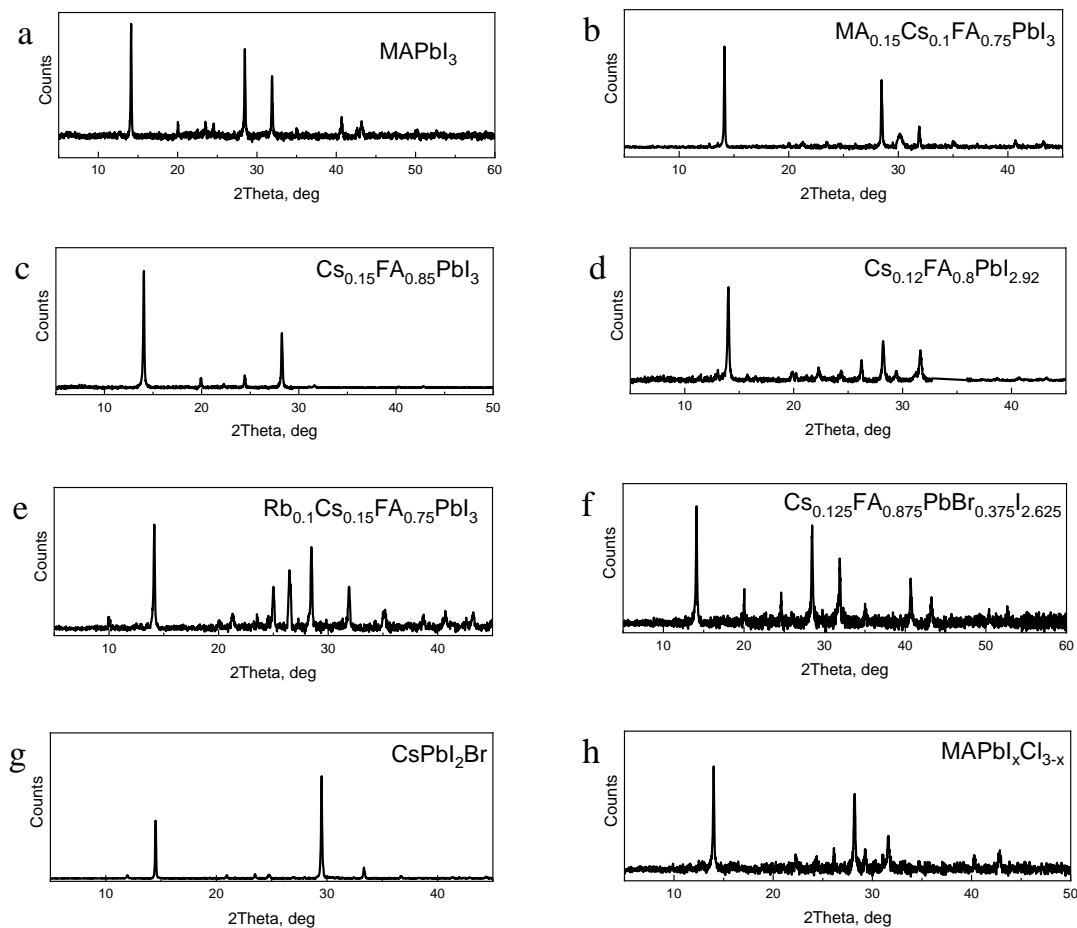


Figure A1. XRD data for freshly prepared optimized thin films of perovskite materials:

MAPbI_3 (a), $\text{MA}_{0.15}\text{Cs}_{0.1}\text{FA}_{0.75}\text{PbI}_3$ (b), $\text{Cs}_{0.15}\text{FA}_{0.85}\text{PbI}_3$ (c) $\text{Cs}_{0.12}\text{FA}_{0.8}\text{PbI}_{2.92}$ (d),

$\text{Rb}_{0.1}\text{Cs}_{0.15}\text{FA}_{0.75}\text{PbI}_3$ (e), $\text{Cs}_{0.125}\text{FA}_{0.875}\text{PbBr}_{0.375}\text{I}_{2.625}$ (f),

CsPbI_2Br (g) and $\text{MAPbI}_x\text{Cl}_{3-x}$ (h).

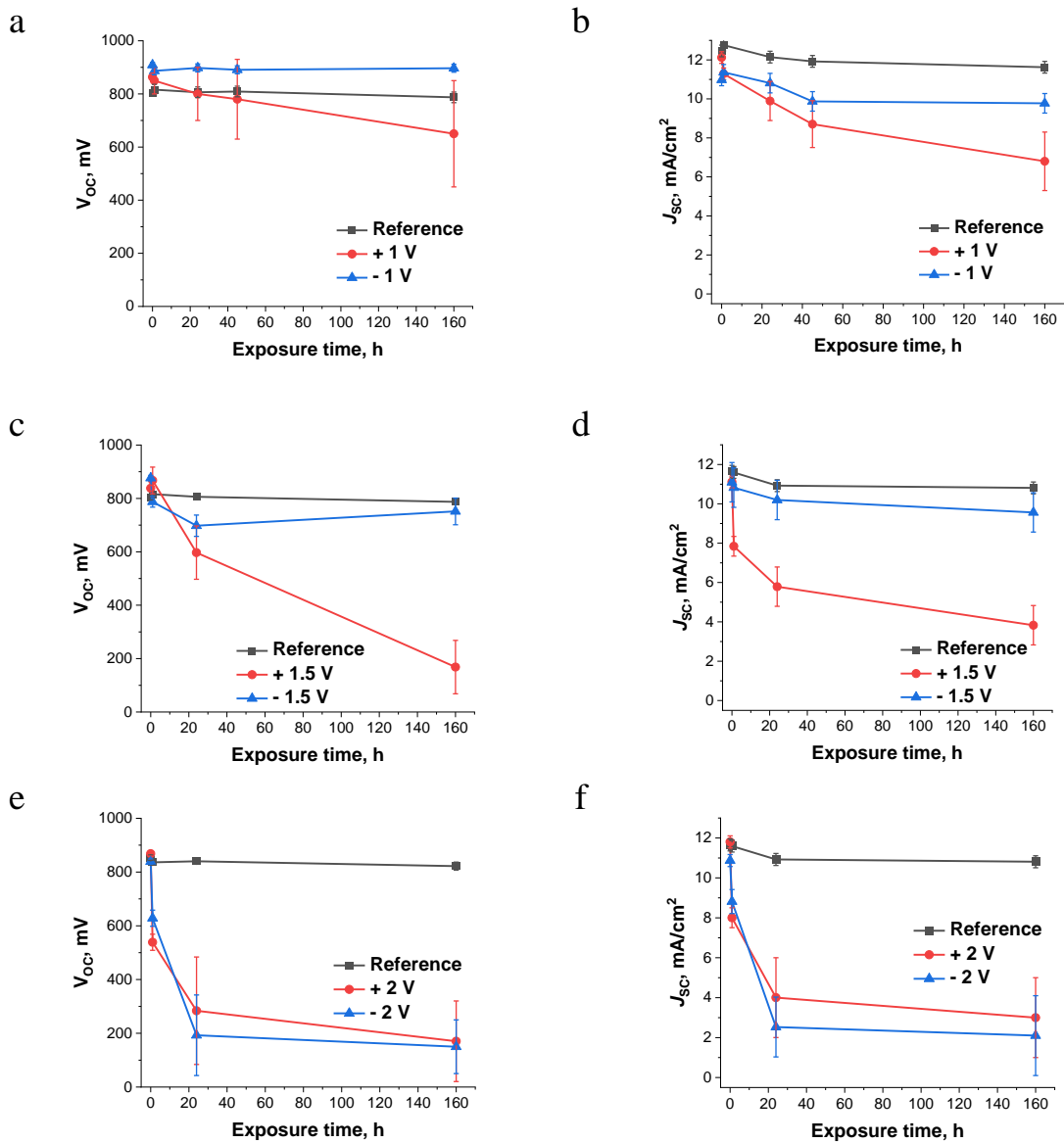


Figure A2. Evolution of the solar cell open circuit voltage (V_{OC} ; a, c, e) and short circuit current density (J_{SC} ; b, d, f) as functions of the electric bias exposure time at the applied potentials of 1 V (a-b), 1.5 V (c-d) and 2 V (e-f) in forward and reverse directions.

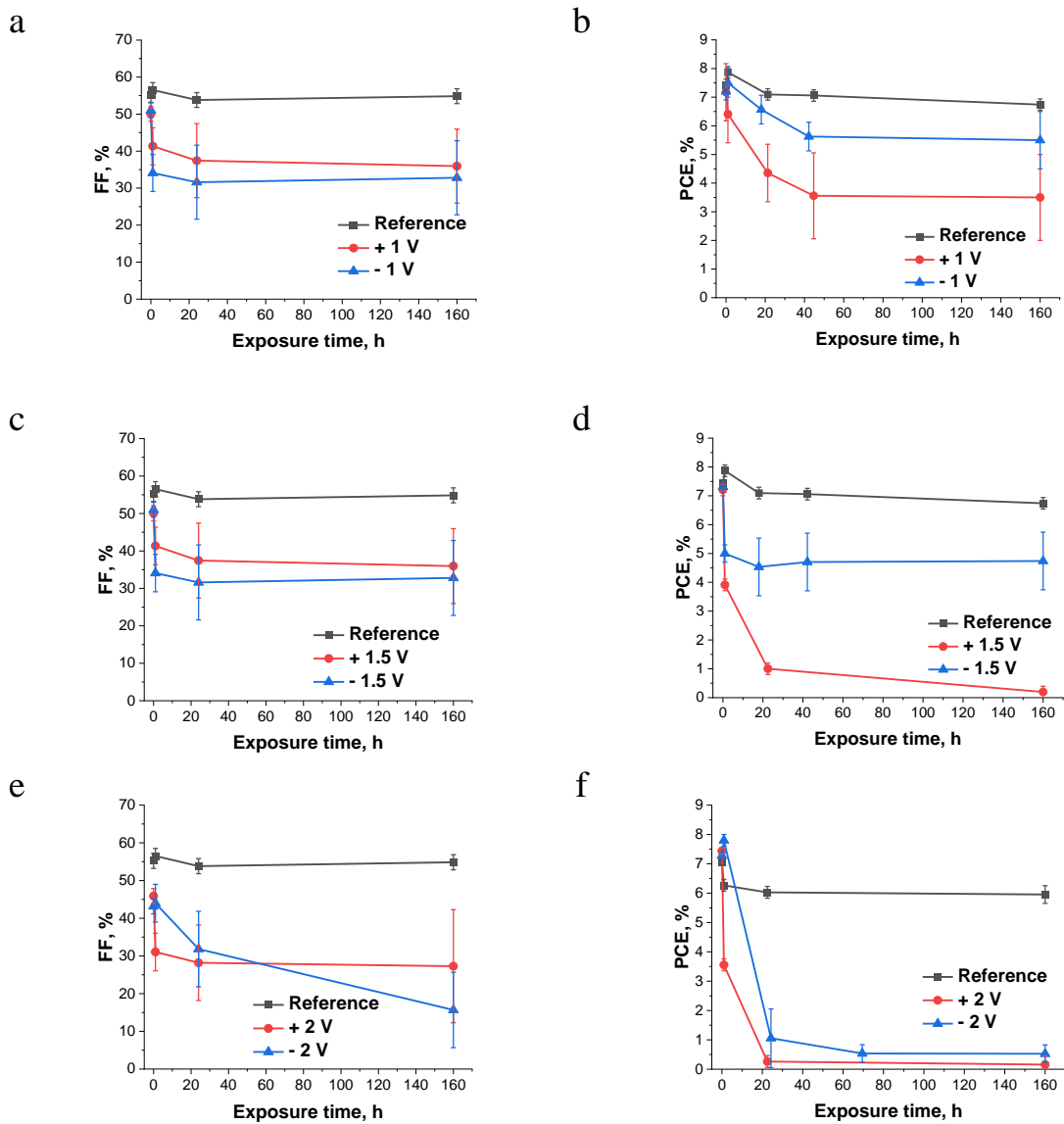


Figure A3. Evolution of the solar cell fill factor (FF; a, c, e) and power conversion efficiency (PCE; b, d, f) as functions of the electric bias exposure time at the applied potentials of 1 V (a-b), 1.5 V (c-d) and 2 V (e-f) in forward and reverse directions.

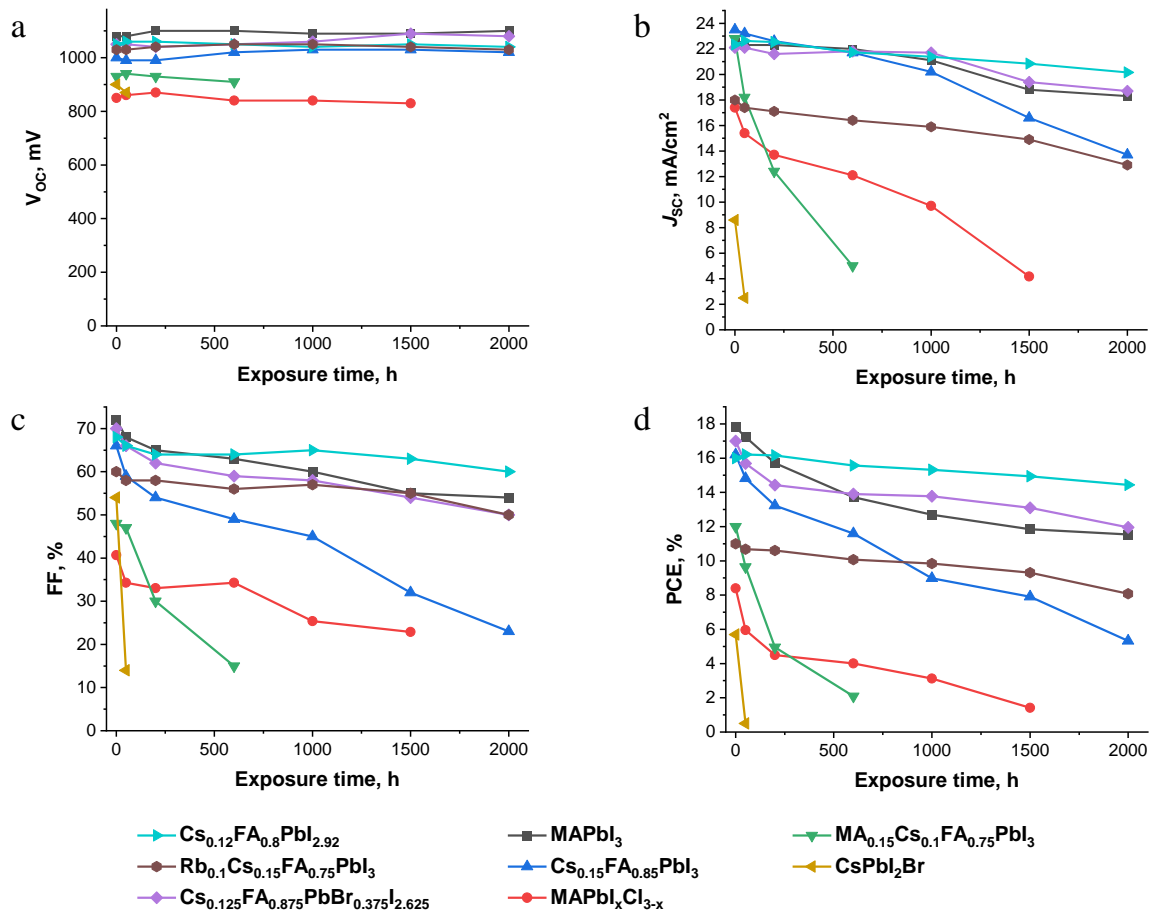


Figure A4. Evolution of the absolute values for solar cell average open circuit voltage V_{oc} (a), short circuit current density J_{sc} (b), fill factor FF (c) and power conversion efficiency PCE (d) as functions of the electric bias exposure time at the applied potential of 1 V in forward direction, depending on the used perovskite material.

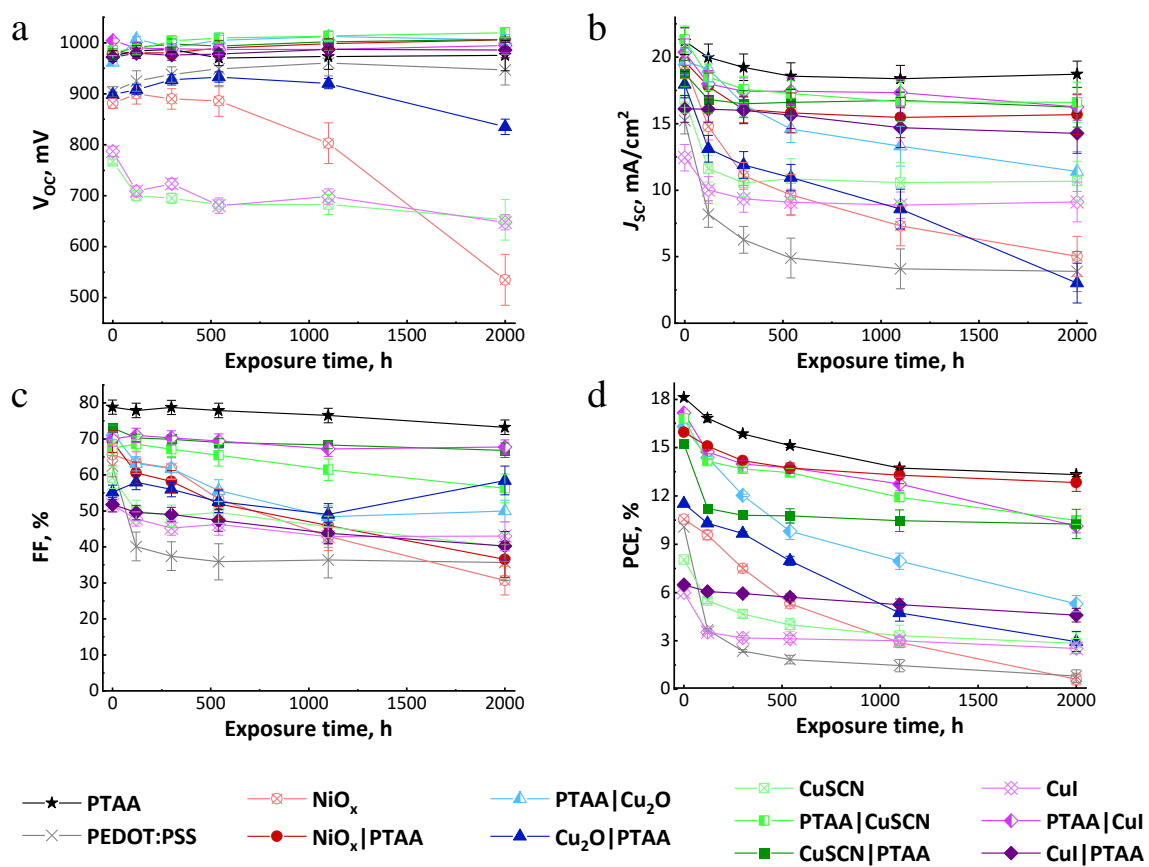


Figure A5. Evolution of the absolute values for solar cell average open circuit voltage V_{oc} (a), short circuit current density J_{sc} (b), fill factor FF (c) and power conversion efficiency PCE (d) as functions of the electric bias exposure time at the applied potential of 1 V in forward direction, depending on the used HTL.

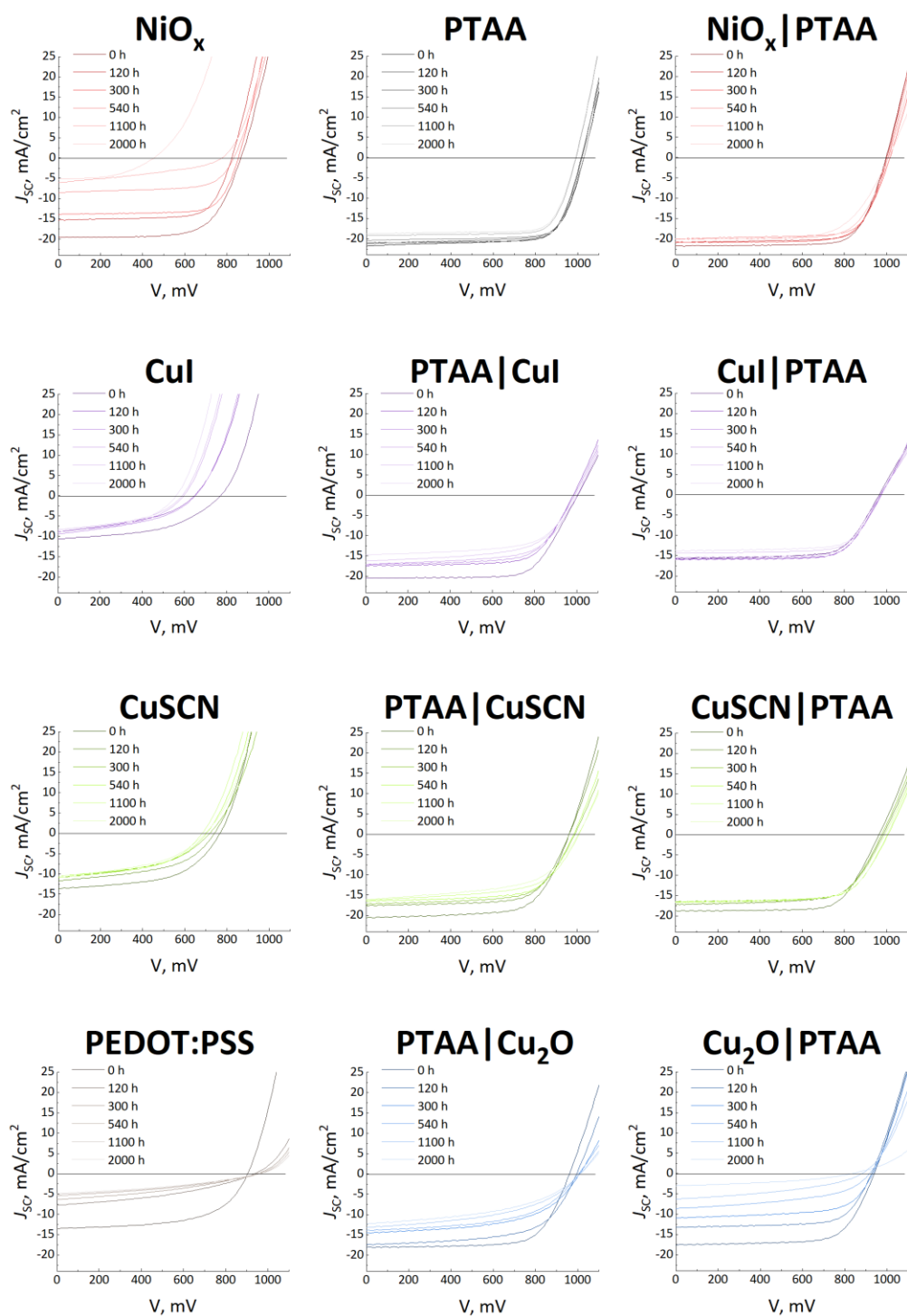


Figure A6. The typical examples of the device J - V curves evolution under 1 V external bias voltage applied in forward direction.

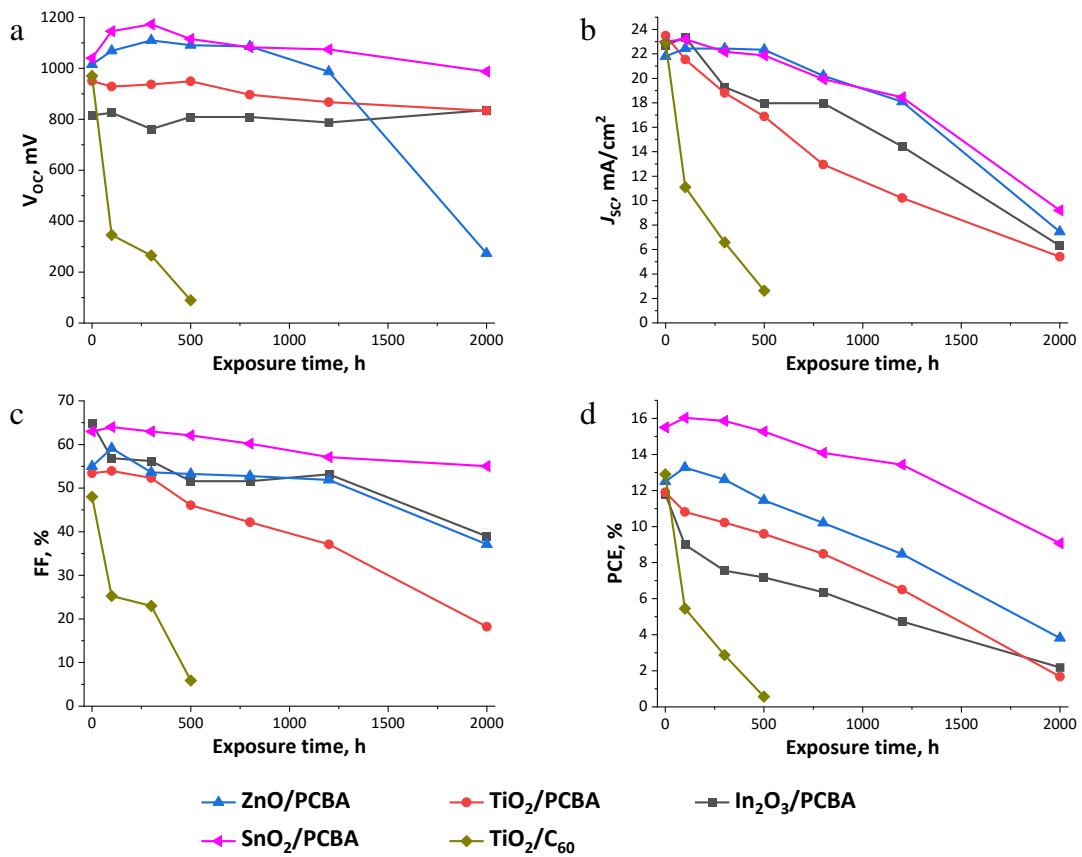


Figure A7. Evolution of the absolute values for solar cell average open circuit voltage V_{oc} (a), short circuit current density J_{sc} (b), fill factor FF (c) and power conversion efficiency PCE (d) as functions of the electric bias exposure time at the applied potential of 1 V in forward direction, depending on the used ETL.

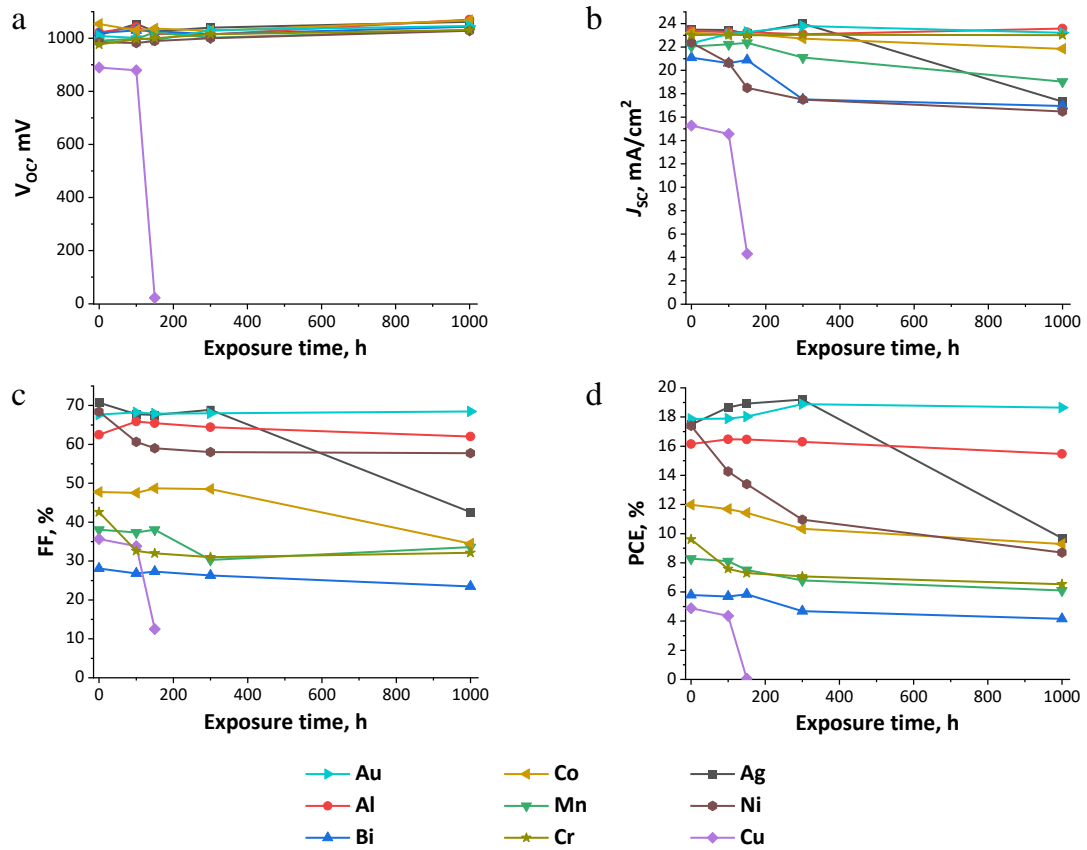


Figure A8. Evolution of the absolute values for solar cell average open circuit voltage V_{OC} (a), short circuit current density J_{SC} (b), fill factor FF (c) and power conversion efficiency PCE (d) as functions of the electric bias exposure time at the applied potential of 1 V in forward direction, depending on the used top electrode metal.